I   PARAMETRIC STUDY OF OPTICALLY PUMPED
    FAR-INFRARED WAVEGUIDE LASERS

II THEORY AND EXPERIMENT OF FOLDED FABRY-PEROT
    QUASI-OPTICAL RING RESONATOR DIPLEXER

Thesis by

Arthur Er-Terg Chiou

In Partial Fulfillment of the Requirements
for the Degree of
Doctor of Philosophy

California Institute of Technology

Pasadena, California

1983

(Submitted January 6, 1983)

TO

MY FATHER

WITH

LOVE, GRATITUDE AND RESPECT.

ACKNOWLEDGEMENTS

ABSTRACT

This thesis consists of two parts, each representing a different aspect of far-infrared (FIR) physics and technology.

Part I deals with the problems related to the physics and the design of one of the extremely useful coherent sources in the FIR region of the electromagnetic spectrum : the optically-pumped FIR waveguide laser. The effects of small waveguide diameter were studied here particularly because of their importance to the practical realization of a compact coherent FIR laser. Two known theoretical models were used to analyze the performance of CH_3OH 118 μm laser and CH_3F 496 μm laser; the results from these models were compared with the results of our experimental parametric study on CH_3OH 118 μm laser. A simplified model of Lourtioz and Adde agrees reasonably well, in a semi-quantitative sense, with our experimental results. The λ^2/a^3 dependence of distributed waveguide loss for FIR radiation turns out to be the major factor that limits the waveguide size.

Part II deals with a problem related to the physics and design of a diplexer for application in the FIR heterodyne radiometry, where signals from the local oscillator and the received signal have to be directed into a detector for frequency mixing and for further signal processing. Since the signal of interest is typically very weak, the diplexer should serve the dual purpose of directing the two beams and filtering out the unwanted frequency components (noise) to enhance the signal to noise ratio, and do so with minimum loss.

The optimum design parameters for a folded Fabry-Perot quasi-optical ring resonator diplexer were derived, and its performance was investigated both theoretically and experimentally. The results were compared with those of the similar diplexers of non-optimum geometry. The advantages and limitations of

the optimum diplexer design are analyzed.

TABLE OF CONTENTS

1

PART I

PARAMETRIC STUDY OF OPTICALLY PUMPED FAR-INFRERED WAVEGUIDE LASERS

Chapter 1. INTRODUCTION

1.1 Historical Sketch.

The first optically pumped far infrared (FIR) laser was reported by Chang and Bridges [1.1] in 1970. Laser action on six rotational transitions near 500 μm was observed in methyl fluoride (CH_3F) gas, optically pumped by a Q-switched CO_2 laser. Within a few months, Chang, Bridges and Burkhardt [1.2] reported the first cw FIR laser action observed in methyl fluoride (CH_3F), methyl alcohol (CH_3OH) and vinyl chloride (C_2H_3Cl), pumped by various lines of CO_2 laser.

In 1973, Hodges and Hartwick [1.3] reported the use of hollow waveguide resonator, constructed from both metallic and dielectric tubes for the FIR cavity. Since then, optically pumped FIR waveguide lasers have attracted the attention of experimentalists, virtually from all fields, looking for a simple, compact, rugged, stable, efficient, practical, coherent source in the FIR region of the electromagnetic spectrum.

Some of the important milestones in the development of optically pumped FIR lasers are summarized in Table 1.1.

A bit more than a decade has passed, and hundreds of papers on various aspects of FIR lasers, both theoretical and experimental, have been published. More than twelve hundred FIR laser transitions associated with some fifty molecular isotopic species, have been identified and demonstrated. The latest summary of FIR laser wavelengths is given by Coleman [1.4]. Yet, the long awaited goal of of a simple, compact, rugged, stable, coherent FIR source is still far from being satisfied, and some of the fundamental questions remain unanswered.

This thesis is the result of an exploration of some of the fundamental problems, undertaken in order to reach a better understanding of the physics invloved and better engineering design parameters.

Table 1.1

Some of the Milestones in the Development of Optically Pumped
FIR Lasers.

DATE	DESCRIPTION	REFERENCE
March 1970	The first report of an optically pumped FIR laser (pulsed operation)	Chang and Bridges [1.1]
July 1970	The first report of cw optically pumped FIR laser	Chang, Bridges and Burkhardt [1.2]
May 1973	The first report of optically pumped FIR waveguide laser	Hodges and Hartwick [1.3]
June 1974	The first theoretical treatment (rate equation model) of optically pumped FIR lasers	Tucker [1.9]
August 1976	Application of opto-acoustic absorption cell to the operation of optically pumped FIR lasers	Busse, Basel and Pfaller [1.10]

1.2 The Far-Infrared Region of the Electromagnetic Spectrum.

The exact extent of the "FIR" region of the electromagnetic spectrum is not sharply defined. The region adopted in this thesis is given in various different units in table 1.2. As the wavelength involved is of the order of fraction of a millimeter, it is also known as "submillimeter region" (SMM), especially by people with technical backgrounds in the longer wavelength end (microwave and millimeter wave) of the electromagnetic spectrum. It is also interesting to note that the classical expression for energy per degree of freedom (kT/2) of a system in equilibrium at room temperature is in the FIR region.

The physics and the related applications of FIR radiation, and the experimental difficulties associated with this particular region of electromagnetic spectrum, have been discussed by Chantry [1.5], Robinson [1.6], and Oepts [1.7]. Kimmitt [1.8] also gives brief descriptions of some of the experiments involving FIR radiation. Some of the areas actively involved in the FIR technique are :

* Rotational spectroscopy of molecules

* Lattice vibration in crystals

* Plasma diagnostics (both gaseous and solid state)

* Cyclotron resonance

* Superconductivity

1.3 Optically Pumped FIR Laser Basics.

The basic energy level scheme of a typical optically pumped FIR laser is illustrated in Fig. 1.1. Coincidence of the frequency associated with the energy difference between a rotational level of a higher vibrational state and that of a lower vibrational state of a molecule and the frequency of some infrared laser transition is required. These coincidences occur much more frequently than might be imagined a *priori*, as proven by the large number of FIR laser lines

Table 1.2

The Far-Infrared (FIR) Region of the Electromagnetic Spectrum.

Wavelength	50μm -------- 1000μm
	.05mm ------- 1mm
Wavenumber	$200cm^{-1}$ ----- $10cm^{-1}$
Frequency	$6X10^{12}$ Hz --- $3X10^{11}$ Hz
Energy	.025eV ------ .0012eV
Temperature	$300°K$ -------- $15°K$
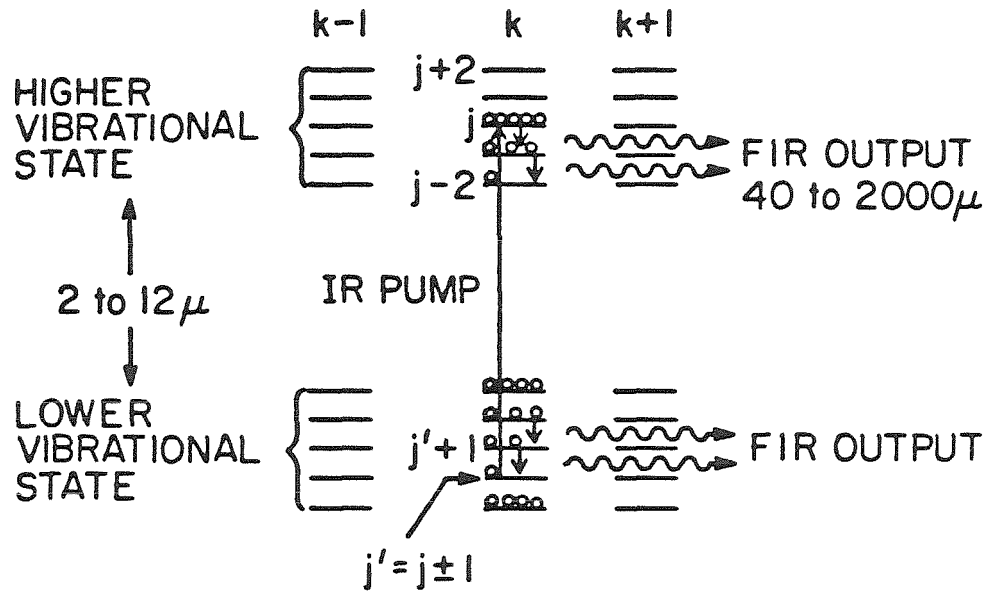
Fig. 1.1   Energy levels of a typical optically pumped
          far-infrared (FIR) laser.

listed in [1.4]. The infrared laser (for instance, a CO_2 laser or a N_2O laser) can then be used as a pump to selectively excite the molecular gas. Population inversion is usually achieved in the rotational manifolds of both the higher and lower vibrational states. Pure rotational transitions among the inverted rotational levels provide the gain where laser action takes place in a cavity with appropriate feedback as illustrated schematically in Fig. 1.2.

A typical experimental set-up is shown in Fig. 1.3. The upper part of the figure shows a conventional grating-tuned CO_2 laser capable of 10 W to 30 W on a variety of vibrational transtions in the 9.6 μm and 10.6 μm bands. Fine frequency tuning of the laser cavity is provided by one of the mirrors mounted on a PZT element shown at the upper right. Rocksalt beam splitters are used to direct some small fraction (about 5%) of the output power for wavelength and power monitoring, as shown at the middle right. The main beam is then focused by a lens (typically a BaF_2 or ZnSe lens) through a small coupling hole in the input mirror, into the FIR cavity, which consists of the input coupling mirror, a waveguide tube and a output coupling mirror. The FIR output power may be monitored either with a thermal detector or a phase-sensitive detection scheme as illustrated in Fig. 1.3. Typical performance data for some of the stronger FIR laser transitions are given in Table 1.3.

1.4 Summary of the Thesis.

Chapter 2 begins with a qualitative picture of the fundamental FIR laser processes followed by a brief survey of various analyses based on the rate equation model. A set of rate equations associated with a simplified model is used to obtain the positive gain criterion originally derived by Tucker [1.9]. Two different models are used to analyse the relationships among the performance and the physical parameters of the laser (gas pressure, waveguide diameter,
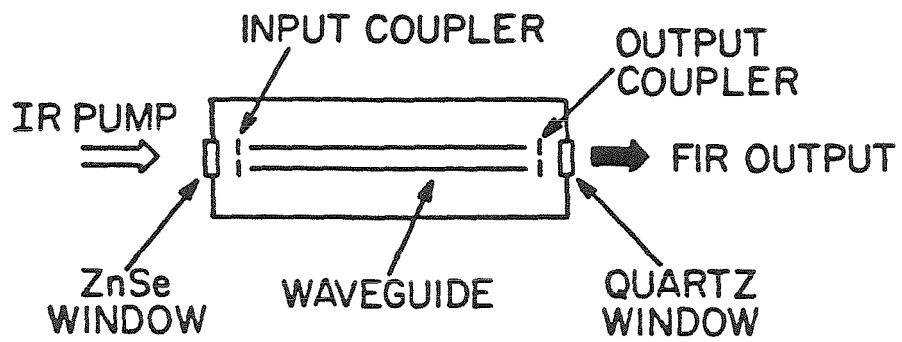
Fig. 1.2 Schematic diagram of a FIR waveguide laser cavity.
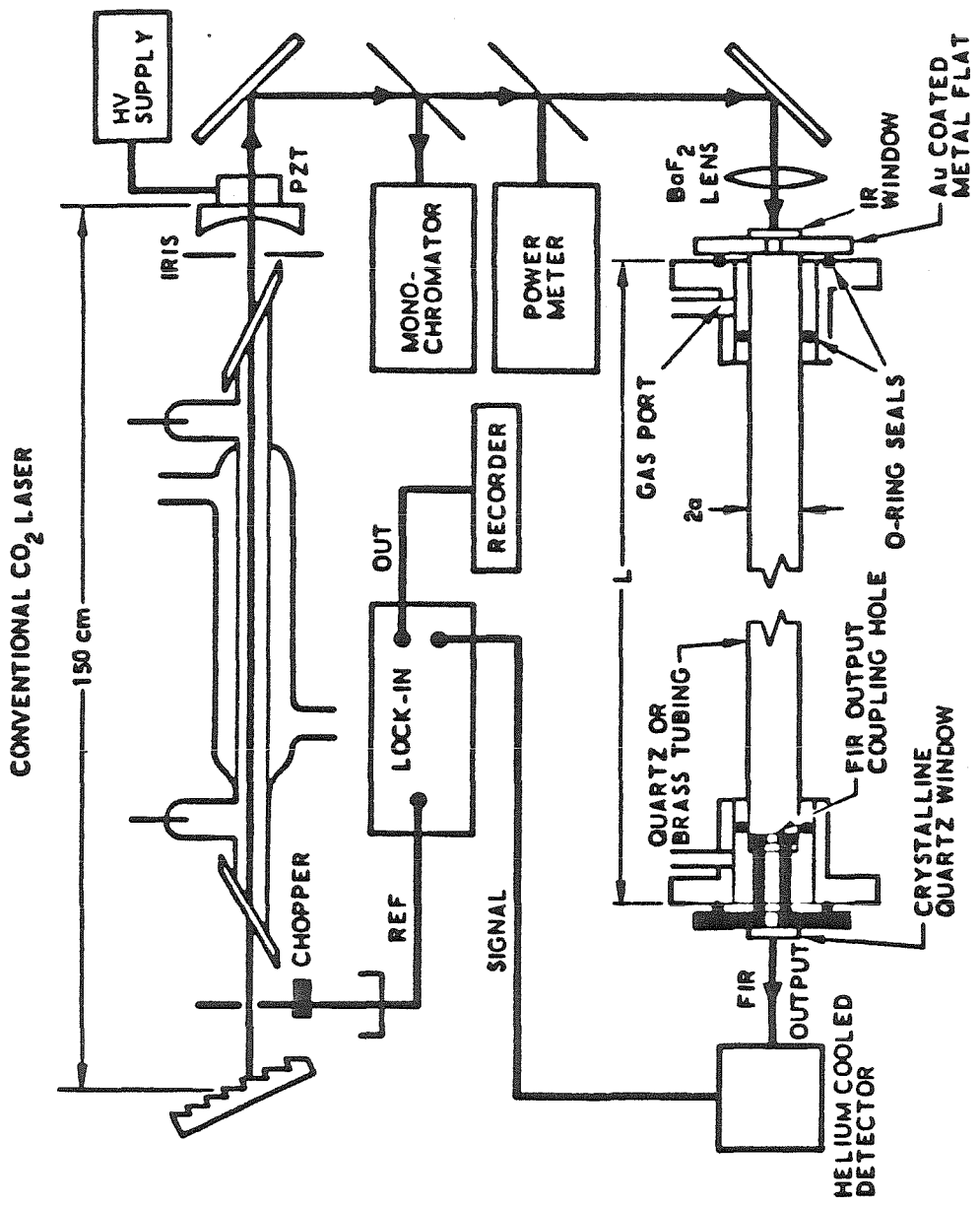
Fig. 1.3 A typical experimental set-up.

(after D.T.Hodges, "The FIR waveguide laser – a practical source," Proc. SPIE vol. 67, 1975, page 43.)

Table 1.3

Typical Performance Data for Some of the Stronger FIR Laser Transitions.
(after M. Yamanaka, "Submillimeter-wave lasers and their applications,"
Jap. J. of Appl. Phys., vol. 49, No. 8, 1980, page 816.)

Molecule	Pump Laser	Wavelength (μm)	Output Power
$^{13}CH_3F$	9 μm P (32) CO_2	1221.8	10 mW (CW, η=4.2%) 8 mW (CW, η= 10%) 5 kW (multi-pulses) 1 MW ($\sim$)
HCOOH	9 μm R (28) CO_2	513.0	40 mW (CW, η=8.2%)
$^{12}CH_3F$	9 μm P (20) CO_2	496.1	40 mW (CW, η=2.9%) 1 MW (multi-pulses) 0.6 MW (single-pulse)
CH_3I	10 μm P (18) CO_2	447.1	40 mW (CW) 100 kW (pulsed)
HCOOH	9 μm R (20) CO_2 9 μm R (18) CO_2	432.7 393.6	50 mW (CW, τ=8.3%) 50 mW (CW, η=7.5%)
D_2O	9 μm R (22) CO_2	384.6	10 MW (multi-pulses) 1.3 MW (single-pulse)
		359	0.7 MW (single-pulse)
CH_2F_2	9 μm R (34) CO_2 9 μm R (32) CO_2 9 μm R (20) CO_2	214.7 184.6 165.9	24.5 mW (CW, η=16%) 33 mW (CW, τ=16%) 44 mW (CW, η=20%)
CH_3OH	9 μm P (36) CO_2	118.8	400 mW (CW, η=7.9%)
D_2O	9 μm P (32) CO_2 9 μm R (12) CO_2	119 114	4.5 MW (multi-pulses) 25 MW ($\sim$)
NH_3	10 μm P (13) N_2O	81.5	40 mW (CW, η=10%)
CH_3OH	9 μm P (34) CO_2	70.5	100 mW (CW, η=2.4%)
D_2O	9 μm P (32) CO_2	66 50.3	45 MW (multi-pulses) 0.45 MW ($\sim$)
CH_3OH	9 μm P (32) CO_2	41.7	55 mW (CW)
CF_4	9 μm R (12) CO_2	16.26	0.5 MW (pulsed, 0.1 J, η=5%)
NH_3	9 μm R (16) CO_2	12.81	1.5 MW (pulsed, 0.75 J, τ=20%)
		12.08	2.8 MW (pulsed, 1.25 J, η=25%)

pump power, etc). Of particular interest here are waveguide diameters sufficiently small that the distributed waveguide loss is comparable to or larger than other loss mechanisms; this condition is of particular interest because waveguide loss turns out to be one of the most crucial factors that limits the size (compactness) of FIR laser.

The problem of power stability of an FIR laser is treated in Chapter 3, where various factors relating to power stability such as CO_2 laser output characteristics, laser gas absorption characteristics and cavity coupling effects are investigated experimentally. The effects of cavity isolation and opto-acoustic active frequency locking are described.

Various techniques and designs of spatially uniform output couplers for the FIR laser cavity are given in Chapter 4. A uniform output coupler is an essential element for experimental investigation of the effect of waveguide radius on the laser performance in order to decouple the effects of changing modes from those caused by the variation of waveguide diameter. No uniform output couplers are yet commercially available, and the design of output couplers (either uniform or non-uniform) have been an interesting field of its own.

The experimental parametric study, investigating the relationships among FIR power output, pressure of FIR laser gas, waveguide diameter and pump power are described in Chapter 5.

A summary of the theoretical and experimental findings, together with their implications, is given in chapter 6.

References for Chapter 1

1.1   T. Y. Chang and T. J. Bridges, "Laser action at 452, 496, and 541 m in optically pumped CH_3F," *Opt. Commun.*, Vol. 1, Apr. 1970, pp. 423-426.

1.2   T. Y. Chang, T. J. Bridges and E. G. Burkhardt, "Cw submillimeter wave laser action in optically pumped methyl fluoride, methyl alcohol, and vinyl chloride gases," *Appl. Phys. Lett.*, Vol. 17, Sept. 15, 1970, pp. 249-251.

1.3   D. T. Hodges and T. S. Hartwick, "Waveguide laser for the far infrared (FIR) pumped by a CO_2 laser," *Appl. Phys. Lett.*, Vol. 23, Sept. 1, 1973, pp. 252-253.

1.4   P. D. Coleman, "Far Infrared Lasers," sec. 3.3 in **CRC Handbook of Laser Science and Technology**, Vol II, Gas Lasers. M. J. Weber, Editor, CRC Press, Miami, 1982.

1.5   G. W. Chantry, **Submillimeter Spectroscopy**, Academic Press, New York, 1971. Chapter 5.

1.6   L. C. Robinson, "Physical Principles of Far-Infrared Radiation," **Methods of Experimental Physics**, Vol. 10, Academic Press, New York, 1973.

1.7   D. Oepts, "Far-Infrared and Submillimeter-Wave Regions," Sec. 4.2 in **Methods of Experimental Physics**, Vol 13-Part B, D. Williams, Editor, Academic Press, New York, 1976.

1.8   M. F. Kimmitt, **Far-Infrared Technique**, Pion Limited, London, England, 1970. Chapter 6.

1.9   J. R. Tucker, "Theory of FIR gas laser," Conference Digest, *International Conf. on Submillimeter Waves and Their Application*, Atlanta, Ga., June 1974., pp. 17. Catalog #74CHO856-5MTT.

1.10   G. Busse, E. Basel and A. Pfaller, "Application of the opto-acoustic effect to the operation of optically pumped far-infrared gas laser," *Appl. Phys.* 12, 1977, pp. 387-389.

Chapter 2. Fundamental Processes and Rate Equation Models

2.1 Introduction.

Some of the fundamental processes which play dominant roles in FIR laser performance have been summarized by Hodges [2.1] as shown in Fig. 2.1. On one hand, the vibrational relaxation process (shown with rate Γ in Fig. 2.1) and the thermal equilibrization process (shown with rate λ) are responsible for "refilling" the population of the initial state (J',K). On the other hand, the same thermal equilibration processes work to eliminate the desired population inversion established in the excited vibrational state by the selective pumping. The optimum operating condition results from the balance of these competing processes, which, in turn depends on macroscopic parameters such as pump power, gas pressure, waveguide diameter and output mirror transmittance. Various loss mechanisms, unavoidable in real laser operation, further complicate the problem.

A more intricate model, taking into account the rotational energy levels and further details of molecular dynamics is illustrated in Fig. 2.2, where

$\Gamma =$ rate of vibrational relaxation to the ground state

$\Gamma_{\Delta J} =$ rate of rotational relaxation to thermal equilibrium within each vibrational manifolds

$\Gamma_{V_z} =$ rate of velocity cross relaxation to equilibrium Maxwellian distribution

$\Gamma_{\Delta K} =$ rate of K-changing collision process.

The rate of K-changing collisional processes as well as other molecular energy transfer mechanisms, such as V-V, V-T , V-R and etc. , (not shown in Fig. 2.2), are known [2.2-2.5] to be much slower than the rotational thermalization rate ($\Gamma_{\Delta J}$) and can be ignored in general.
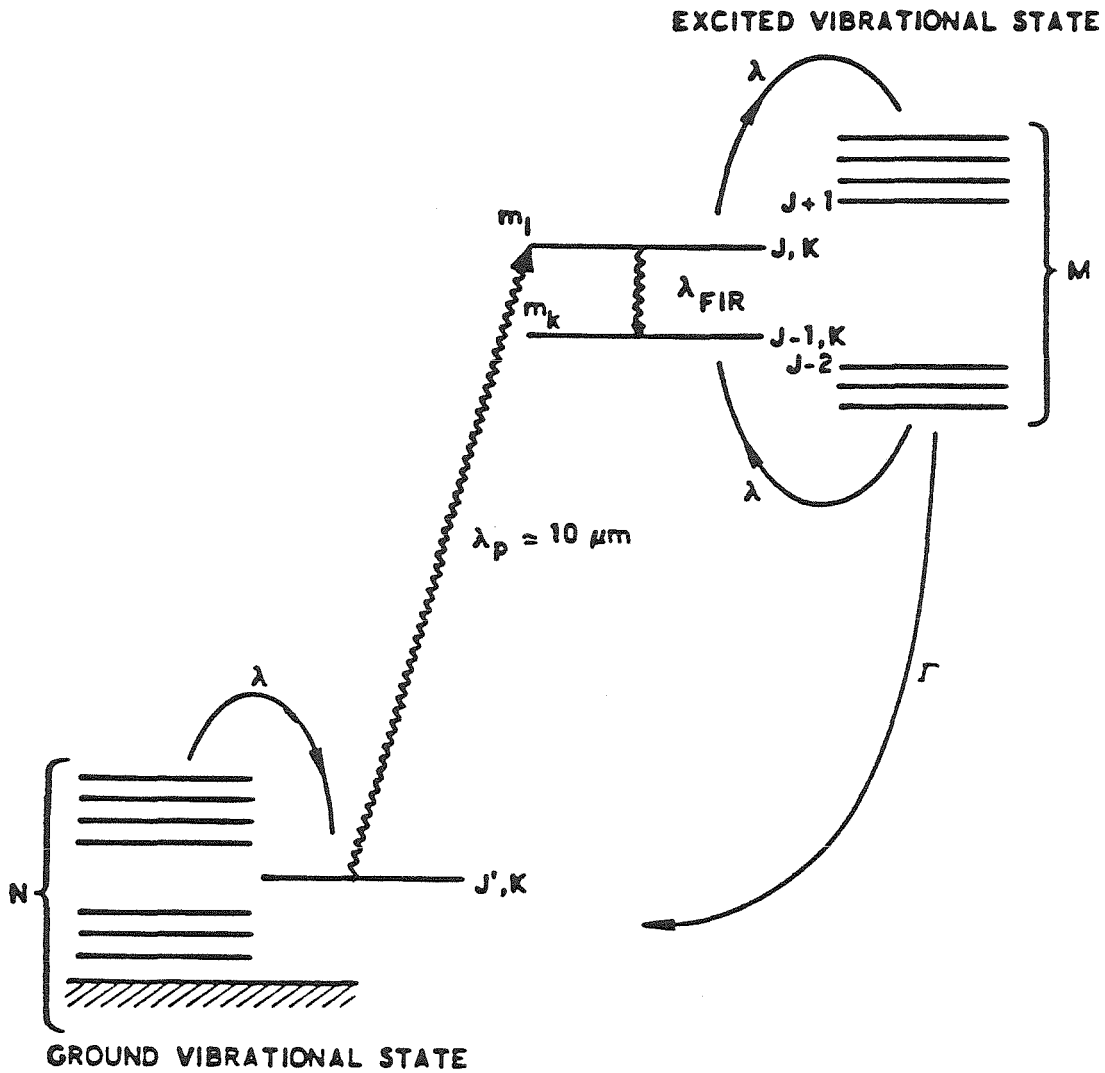
Fig. 2.1. Fundamental processes in optically pumped FIR lasers
(after D.T.Hodges, "The FIR waveguide laser-a practical source,"
Proc. SPIE vol. 67, 1975, page 42.)

15
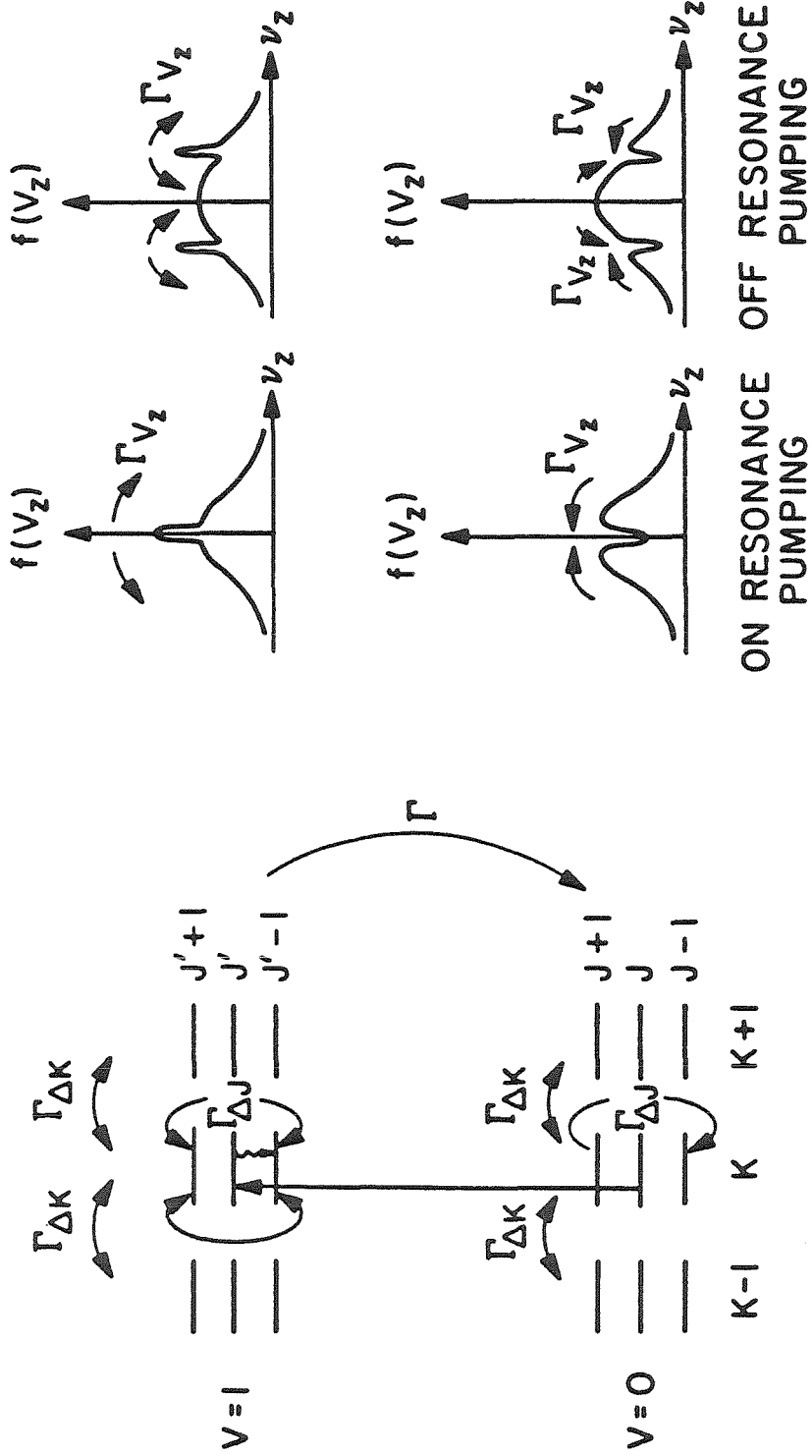
Fig. 2.2 Energy levels diagram showing various collisional processes.

Rate equation models, taking into account the various processes described above, have been used to analyze FIR laser performance [2.6-2.12]. Although certain quantum features [2.13-2.17] which can only be understood by a more exotic quantum mechanical treatment have been reported, rate equations are still useful to analyze performance of cw FIR lasers over a fairly wide range of parameters (pressure, pump power, waveguide radius, etc.) of practical interest.

In pursuing the optimum design of a rugged, compact waveguide FIR laser, it is essential that the dependence of laser performance on size be fully understood. With a cylindrical waveguide structure in mind, waveguide radius is obviously one of the most important parameters. Qualitatively, smaller waveguide diameter should increase the FIR gain because of the better pump confinement and the enhancement of vibrational relaxation via wall collisions. On the other hand, a smaller waveguide diameter results in larger waveguide loss for both the pump and the FIR laser beams. In order to understand the overall performance of an FIR laser, a tradeoff between these conflicting requirements should be analyzed.

A rate equation analysis, taking into account all the fundamental processes illustrated in Fig. 2.2, was first reported by DeTemple and Danielewicz [2.9] for the cw CH_3F waveguide laser at 496 μm. Their theoretical results, for the relationships between FIR output power, pump power , optimum pressure and FIR output mirror transmittance agree fairly well with their experimental data. Unfortunately, the dependence of these parameters on waveguide diameter is not given explicitly, except for one graph of FIR saturation intensity versus pressure with waveguide radius as parameter.

Following a similar approach, Kokubo et al [2.11] obtained the relationship

between FIR output power, gas pressure, waveguide diameter, and FIR output mirror transmittance for a CH_3F metallic waveguide laser at 496 μm, assuming 8 W pump power and 80 cm waveguide length.

The same approach was also followed by Lourtioz and Adde [2.12] to analyze the performance of 118.8 μm CH_3OH laser at various pressures, and pump powers for an 1.8 m long, 25 mm ID pyrex waveguide.

In Section 2.2 a set of simplified rate equations, taking into account only those fundamental processes illustrated in Fig. 2.1, is used to obtain the positive gain criterion originally derived by Tucker [2.6]. In Section 2.3 a simple phenomenological model incorporating the positive gain criterion is used to estimate the FIR laser performance as a function of pressure, pump power and waveguide diameter. An implicit expression for FIR output power given by Lourtioz and Adde [2.12] is simplified and the effect of waveguide loss is investigated in Section 2.4. In Section 2.5 we conclude this chapter by summarizing the major similarities and differences of the results predicted by the two models. A more elaborate discussion and a comparison with experimental results are given in Chapter 6.

2.2 The Rate Equations and Positive Gain Criterion.

The model illustrated in Fig. 2.1 is reproduced in Fig. 2.3 with minor rearrangement and a few changes in notation for convenience. The rate equations associated with this picture are :

$$\dot{N}_1 = N_{21}W_p + (f_1 N_{V0} - N_1)\Gamma_j \qquad (2.1)$$

$$\dot{N}_2 = -N_{21}W_p - N_{23}W_F + (f_2 N_{V1} - N_2)\Gamma_j \qquad (2.2)$$

$$\dot{N}_3 = N_{23}W_F + (f_3 N_{V1} - N_3)\Gamma_j \qquad (2.3)$$
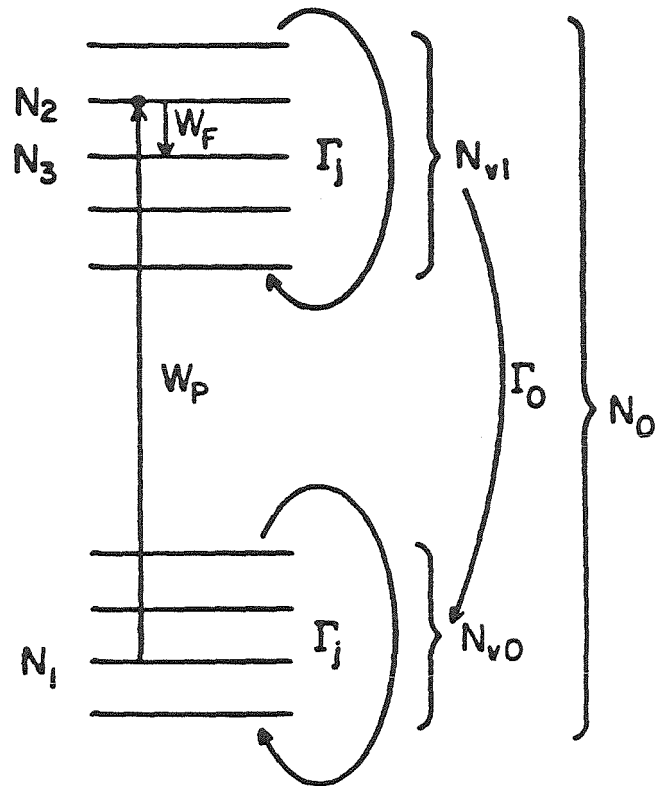
Fig. 2.3 A simplified energy level diagram and fundamental processes of an optically pumped FIR laser.

$$\dot{N}_{V0} = N_{21}W_p + N_{V1}\,\Gamma_0 \qquad\qquad (2.4)$$

$$\dot{N}_{V1} = -N_{21}W_p - N_{V1}\,\Gamma_0 \qquad\qquad (2.5)$$

$$\dot{n}_p = n_p\,(\alpha_p - \gamma_p - \gamma'_p/L)\,C + Z_p \qquad\qquad (2.6)$$

$$\dot{n}_F = n_F\,(\alpha_F - \gamma_F - t/2L)\,C \qquad\qquad (2.7)$$

$$N_{V0} + N_{V1} = N_0 \qquad\qquad (2.8)$$

where

$N_{ij} = N_i - \dfrac{g_i}{g_j}N_j$ is the population inversion;

f_i is the Boltzmann occupation factor of level i;

Γ_j is the rate of thermal equlibration within each vibrational level and is given by $\pi\Delta\nu$, where $\Delta\nu$ is the linewidth (FWHM) due to pressure broadening;

Γ_0 is the rate of transition from vibrational excited state to vibrational ground state;

Z_p is the rate of input photon density due to the pump and is related to pump power P by $Z_p = P_p/\pi a^2 Lh\nu_p$; where a is the guide radius and L is the length of the FIR cavity;

α_p is the absorption coefficient for the pump beam and is given by [2.18] $\alpha_p = N_{21}\lambda^2_p g_p(\nu)/\pi a^2 L8\pi t_{21}$, where t_{21} is the spontaneous lifetime for the $2\rightarrow1$ transition and $g_p(\nu)$ is the appropriate lineshape function; α_p is also related to pumping rate W_p and circulating pump photon density n_p by

$$N_{21}W_p = \alpha_p n_p c\pi a^2 L; \quad W_p = n_p\frac{\lambda^2_p c}{8\pi t_{21}}g_p(\nu)\,).$$

$\gamma_p(\gamma_F)$ is the distributed waveguide loss for the pump (FIR) beam;

γ_p' is the mirror absorption loss and the diffraction loss of the pump beam at the end reflectors;

α_F is the FIR gain coefficient, given by $\alpha_F = N_{23}\lambda^2_F g_F(\nu)/\pi a^2 L 8\pi t_{23}$ [2.18]; α_F is related to the FIR transition rate W_F and the circulating FIR photon density n_F by $N_{23}W_F = \alpha_F n_F c \pi a^2 L$; $W_F = n_F \dfrac{\lambda^2_F c}{8\pi t_{23}} g_F(\nu)$

t is the transmittance of FIR output coupler.

Quantum numbers J and K for those states directly involved in the pump excitation and FIR laser transition are given in Table 2.1 for both CH$_3$OH 118.8 μm line and CH$_3$F 496 μm line. The corresponding Boltzman factors are also listed in the same table for later convenience.

The steady state solution is obtained by setting all the time rates of change [L.H.S. of eqns.(2.1) through (2.7)] equal to zero. Solving for N_{21} and N_{23}, we obtain

$$N_{21} = - f_1 \Gamma_j N_0 [W_F (1 + \frac{g_2}{g_3}) + \Gamma_j]/D \qquad (2.9)$$

$$N_{23} = f_1 \Gamma_j N_0 W_P [1 - R(\frac{g_2}{g_3}f_3 - f_2)]/D \qquad (2.10)$$

where

$$D = W_p W_F [1 + \frac{g_1}{g_3} + \frac{g_2}{g_3} + f_1 R(1 + \frac{g_2}{g_3}) + \frac{g_1}{g_3}R (f_2 + f_3)$$

$$+ W_P \Gamma_j [1 + \frac{g_1}{g_2} + f_1 R + \frac{g_1}{g_2}f_2 R] + W_F \Gamma_j (\frac{g_1}{g_2} + \frac{g_1}{g_3}) + \frac{g_1}{g_3}\Gamma_j^2$$

and

$$R \equiv \Gamma_j/\Gamma_0$$

Table 2.1

Some Spectroscopic Data Associated With the CH_3OH 118.8μm Laser Line and CH_3F 496μm Laser Line.

	CH_3OH 118μm	CH_3F 496μm
J_1	8	12
J_2	16	12
J_3	15	11
K_1	8	2
K_2	8	2
K_3	7	2
f_1	1.83×10^{-3}	6.6×10^{-3}
f_2	1.83×10^{-3}	6.6×10^{-3}
f_3	2.64×10^{-3}	6.71×10^{-3}
g_1	33	25
g_2	33	25
g_3	31	23

From (2.9) and (2.10), we see that N_{21} is always negative as expected while N_{23} may be positive or negative. The positive gain criterion ($N_{23}>0$) leads to the condition

$$[\ 1 - \frac{\Gamma_j}{\Gamma_0}\ (\frac{g_2}{g_3}f_3 - f_2\ )\ ] > 0 \tag{2.11}$$

For $\frac{h\nu_P}{kT}\ll 1$, the factor $\frac{f_3/g_3}{f_2/g_2} - 1$ is approximately equal to $\frac{h\nu_P}{kT}$ [2.22] to a very good approximation, and (2.11) can be rewritten as

$$[\ 1 - \frac{\Gamma_j}{\Gamma_0}f_2\frac{h\nu_P}{kT}\ ] > 0 \quad \text{or} \quad \Gamma_0 > \Gamma_j f_2\frac{h\nu_P}{kT} \tag{2.12}$$

Equation (2.12) is the positive gain criterion originally derived by Tucker [2.6]. The condition as required by (2.11) or (2.12) is by no means sufficient. In practice waveguide loss is always present, and equation (2.7) indicates that the practical laser operating condition should read $\alpha_P - \gamma_P - \frac{t}{2L} = 0$.

Although the approximation $\frac{h\nu_P}{kT}\ll 1$ is fairly good for the 496 μm line at room temperature ($\frac{h\nu_P}{kT}\approx 0.1$), for much shorter wavelengths such as the CH_3OH 118.8 μm line where $\frac{h\nu_P}{kT}\approx 0.4$ at room temperature the approximation is not as good, and the more general expression (2.11) should be used instead of (2.12). The positive gain criterion in Tucker's approximation and in the more general form are compared in Table 2.2 for both CH_3OH 118 μm and CH_3F 496 μm lines at $\approx$ 300 K.

The rotational thermalization rate Γ_j is given by $\pi\Delta\nu_H$, where $\Delta\nu_H$ is the line width due to collisional (homogeneous) broadening and is known [2.19] to be $\approx$40 MHz per torr for most of the FIR laser molecules. (The value for CH_3OH reported by Lourtioz and Adde [2.12] is $\approx$ 28 MHz per torr. Γ_j can therefore be

Table 2.2

The Positive Gain Criterion

Comparison of the General Expression and the Tucker's Approximation
For CH_3OH 118.8 µm line and CH_3F 496 µm Line.

	CH_3OH 118.8 um	CH_3F 496 um
General expression		
$\left[1 - \dfrac{\Gamma_j}{\Gamma_0} f_2 \left(\dfrac{f_3 / g_3}{f_2 / g_2} - 1 \right) \right] > 0$	$\dfrac{\Gamma_0}{\Gamma_j} > 9.8 \times 10^{-4}$	$\dfrac{\Gamma_0}{\Gamma_j} > 6.93 \times 10^{-4}$
Tucker's approximation		
$\left[1 - \dfrac{\Gamma_j}{\Gamma_0} f_2 \left(\dfrac{h\nu}{KT} \right) \right] > 0$	$\dfrac{\Gamma_0}{\Gamma_j} > 7.32 \times 10^{-4}$	$\dfrac{\Gamma_0}{\Gamma_j} > 6.65 \times 10^{-4}$
percentage error	25 %	4 %

expressed as $\Gamma_j = C_2 p$ where p is the gas pressure in Torr and C_2 is constant for a given gas, lying in the range of 20×10^6 to 40×10^6 Sec^{-1}Torr^{-1}.

In general, both molecular collisions and diffusion (collisions with the waveguide wall) may contribute to the vibrational relaxation process, and the vibrational relaxation rate Γ_0 can be expressed as

$$\Gamma_0 \quad = \quad C_3 p \quad + \quad C_4/pa^2 \qquad\qquad (2.13)$$

collision term   diffusion term

Two important special cases should be noted:

(1) If $C_3 p \gg C_4/pa^2$ (collision-dominant relaxation), we have $\dfrac{\Gamma_j}{\Gamma_0} \approx \dfrac{C_2}{C_3}$, and the positive gain criterion is independent of pressure and waveguide diameter.

(2) If $C_3 p \ll C_4/pa^2$ (diffusion-dominant relaxation), then $\dfrac{\Gamma_j}{\Gamma_0} \approx (pa)^2 C_2/C_4$ and the positive gain criterion not only establishes a maximum operating pressure but also requires that the cutoff pressure be inversely proportional to the waveguide diameter.

For CH_3F where $C_4 \approx 4.5 \times 10^2$(Sec^{-1} Torr cm^2), $C_3 \approx 5.9 \times 10$(Sec^{-1}Torr^{-1}) [2.20] , simple calculation reveals that under typical operating conditions for the CH_3F 496 μm waveguide laser (p~30 to 100 μ, a~0.5 cm to 1.5 cm), $C_4/pa^2 \gg C_3 p$, and the vibrational relaxation is dominated by diffusion processes. The a^{-1} dependence of cutoff pressure has been verified, and the vibrational relaxation bottleneck limited by diffusion is now believed to be one of the major causes for the relatively poor output power of the cw CH_3F 496 μm laser.

The processes that limit CH_3OH laser performance are not so well understood and will be discussed in the following sections.

2.3 A Simple Phenomenological Model.

In a review paper [2.19] based on rate equation model of Tucker [2.6] and some phenomenological factors, Hodges estimated the maximum efficiency for conversion of infrared pump power P_p into far-infrared laser output power P_{FIR} as

$$\frac{P_{FIR}}{h\nu_{FIR}} = [\frac{1}{1 + g_2/g_3}](\frac{P_p}{h\nu_p})(\frac{\gamma L}{\gamma L + A_p})(\frac{T}{A + T}) [1 - f_2 \frac{h\nu_{FIR}}{kT} \frac{\Gamma_j}{\Gamma_0}] \qquad (2.14)$$

where g_2 and g_3 are the degeneracies of the upper and lower FIR laser levels, ν_p is the frequency of pump radiation, T is the FIR mirror transmission, A is the cavity loss at the FIR wavelength, γ is the absorption coefficient for the pump, L is the cavity length, and A_p is the cavity loss at the pump wavelength. The physical meaning associated with eqn.(2.14) can be interpreted as follow :

$(P_p/h\nu_p)$ = rate of pump photon input.

$[\gamma L/(\gamma L + A_p)]$ = pumping efficiency.

$(P_p/h\nu_p)[\gamma L/(\gamma L + A_p)]$ = effective rate of pumping = rate of populating the upper laser level by the IR pump.

$[1/(1+g_2/g_3)](P_p/h\nu_p)[\gamma L/(\gamma L+A_p)]$ = FIR photon emission rate. (assuming that stimulated emission is the only process that depopulates the upper laser level)

$T/(A+T)$ = fraction of FIR photons coupled out.

$$[\frac{1}{1 + g_2/g_3}](\frac{P_p}{h\nu_p})(\frac{\gamma L}{\gamma L + A_p})(\frac{T}{A + T}) [1 - f_2 \frac{h\nu_{FIR}}{kT} \frac{\Gamma_j}{\Gamma_0}]$$

= rate of FIR photon output

= $P_{FIR}/h\nu_{FIR}$

The factor $(1-f_2\dfrac{h\nu_{FIR}}{kT}\dfrac{\Gamma_j}{\Gamma_0})$ is the positive gain criterion in Tucker's approximation explained in the previous section.

In this simplified picture, the pump power enters only as a scaling factor. Saturation effects of both the pump excitation and FIR laser transition are completely ignored, and the cutoff pressure is determined solely by Tucker's positive gain criterion, independent of pump power.

Using Hodge's estimation [equation (2.14)], with the expression $(1-f_2\dfrac{h\nu_{FIR}}{kT}\dfrac{\Gamma_j}{\Gamma_0})$ replaced by the more general expression $1-\dfrac{\Gamma_j}{\Gamma_0}f_2(\dfrac{f_3/g_3}{f_2/g_2}-1)$ we rewrite equation (2.14) as

$$P_{FIR} = [\frac{1}{1+g_2/g_3}]P_p\frac{\nu_F}{\nu_p}(\frac{\gamma L}{\gamma L+A_p})(\frac{T}{A_F+T})[1-f_2(\frac{f_3/g_3}{f_2/g_2})\frac{\Gamma_j}{\Gamma_0}] \qquad (2.15)$$

and use it to estimate the dependence of FIR output power on the active gas pressure and waveguide diameter.

The parameters and the associated numerical values used in our computation are listed in Table 2.3, and the results for CH_3OH and CH_3F are discussed below. The results of our simple model calculation for the CH_3F 496 μm line are shown in Fig. 2.4 for various waveguide radii and two different values of the loss parameter ($C_1 = 0.025$ and 0.25). $C_1 = 0.025$ corresponds approximately to a loss fifty times larger than that calculated for a pyrex waveguide EH_{11} mode at 496 μm, as evaluated by Marcatili's theory [21]. Since combinations of higher order modes are generally expected in such an "overmoded" waveguide, C_1 is here incorporated as an adjustable parameter to investigate the effects of overall distributed waveguide loss on FIR laser performance.

In this simple model, both the optimum pressure and the cutoff pressure are

Table 2.3

Parameters for CH_3OH 118 m Laser and CH_3F 496 m Laser Used in the Phenomenological Model Calculation.

	CH_3OH 118 um	CH_3F 496 um
g_j/g_k	1.065	1.087
ν_{FIR} / ν_P	9.69/118.8	9.55/496
P_P	8 W	8 W
T	12 %	12 %

$A_F = 0.08 + C_1 / a^3$
C_1 = waveguide loss parameter $C_1 = 0.025, 0.25$ $C_1 = 0.0125, 0.25$
a = waveguide radius in cm   a = .3 cm to 1.5 cm for both lasers

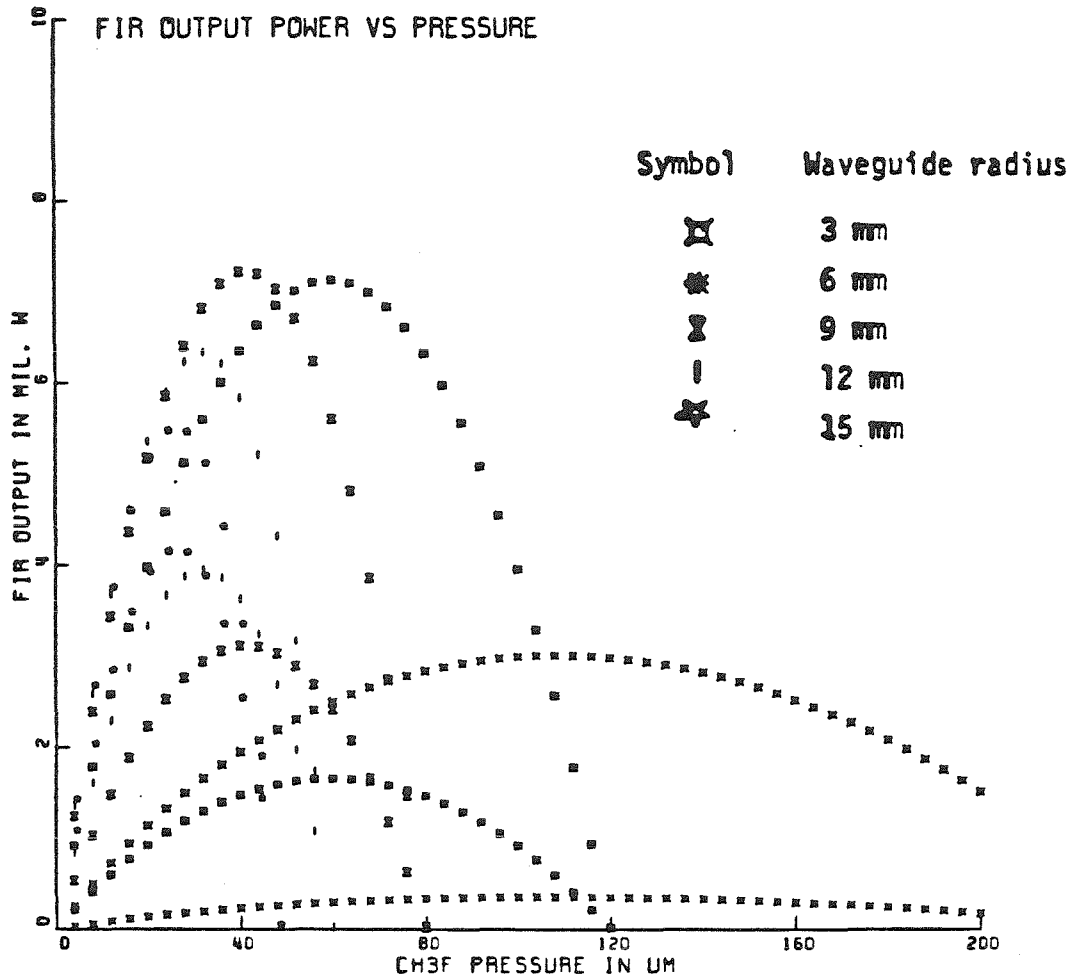|		
γ	$1.1 \times 10^{-2} \, cm^{-1}/torr$	$1.75 \times 10^{-2} \, cm^{-1}/torr$
L	122 cm	122 cm
A_P	25 %	25 %
f_2	1.83×10^{-3}	6.6×10^{-3}
f_3	2.64×10^{-3}	6.71×10^{-3}
$\Gamma_j = C_2 p$ (p in Torr)	$C_2 = 28 \times 10^6$	40×10^6
$\Gamma_0 = C_3 p + C_4/p a^2$	$(C_3, C_4) =$ $(5.9 \times 10^2, 4.5 \times 10^2)$	$(5.9 \times 10^2, 4.5 \times 10^2)$
		$(5.9 \times 10^2, 4.5 \times 10^3)$
		$(5.9 \times 10^4, 4.5 \times 10^2)$

Fig. 2.4. Performance of CH_3F 496 μm laser as estimated by simple phenomenological model. Pump power = 8 W. FIR waveguide loss factor C_1 = 0.025 for the upper curve and 0.25 for the lower curve. (see text)

essentially determined by the ratio of the vibrational relaxation rate to the collisional thermalization rate via the positive gain criterion, and are almost independent of all other parameters. (There is a slight dependence of optimum pressure on pump loss A_p; the optimum pressure increases slightly as A_p increases). The optimum waveguide diameter is, however, essentially determined by the FIR waveguide loss factor C_1 as expected. For $C_1 = .025$, the optimal waveguide radius is around 0.8 cm, whereas for $C_1 = 0.25$ (i.e. a ten times lossier waveguide), it shifts toward the value beyond 1.5 cm.

For the CH_3OH 118.8 μm line, the value of C_1 is expected to be much smaller $[(118/496)^2 \sim 1/17 \,]$ because of the λ^2 dependence [2.21]. In order to analyze various effects of different factors, we use $C_1 = 0.0125$ and $C_1 = 0.25$, with appropriate spectroscopic data for CH_3OH 118 μm line, while keeping the vibrational relaxation rate unchanged. The results as shown in Fig.2.5 reveal that all the features remain essentially unchanged except for a gain in output power due to the quantum efficiency factor (ν_F/ν_p). The effects of the collisional contribution and the diffusional contribution to vibrational relaxation $[\Gamma_0 = C_3 p + C_4/pa^2]$ are then obtained by using $C_3=5.9\times10^4$, $C_4=4.5\times10^2$ (i.e., increasing the collisional contribution by 100-fold) and $C_3=5.9\times10^2$, $C_4=4.5\times10^3$ (i.e. increasing the diffusional contribution by 10-fold) and repeating the calculation for the CH_3OH 118 μm line. The results are shown in Fig. 2.6 and Fig. 2.7. Increasing the collisional rate even by 100-fold has very little effect on FIR laser performance except for a slight increase in the cutoff pressure and optimal pressure, particularly for large diameter waveguide. Increasing the diffusional contribution by 10-fold, however, not only results in much larger optimum pressures and cutoff pressures, but also increases the output power by a factor of two or more.

FIR OUTPUT POWER VS PRESSURE
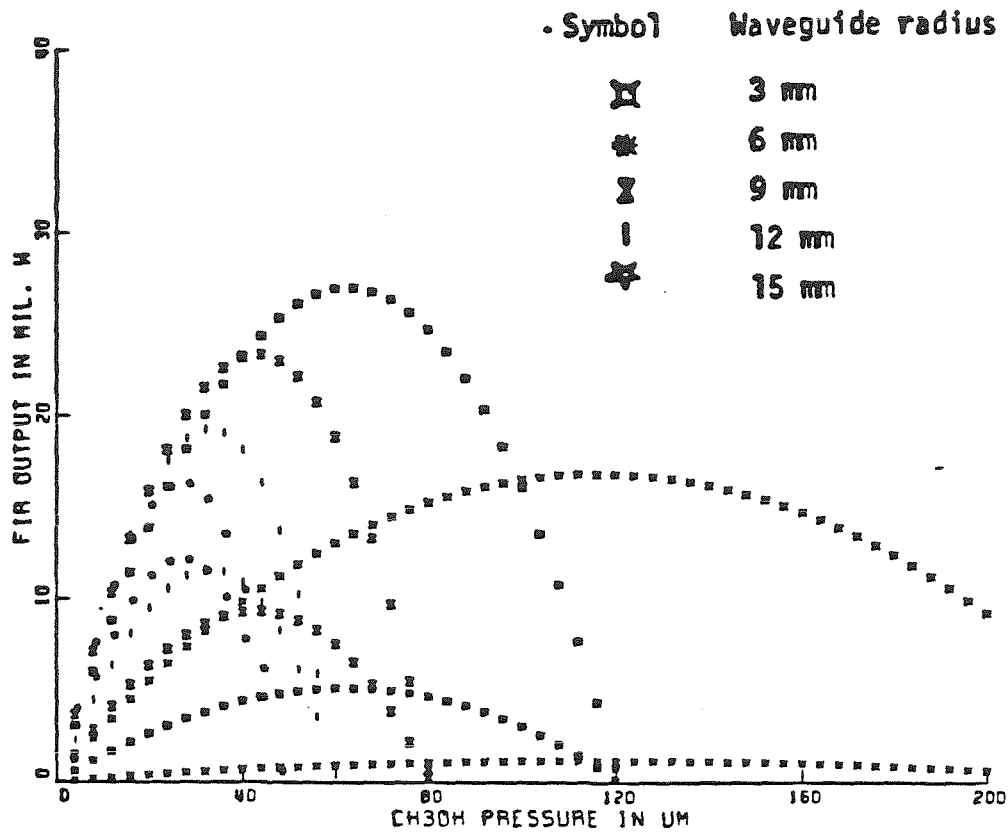
Fig. 2.5. Performance of CH_3OH 118.8 μm laser as estimated by simple phenomenological model. FIR waveguide loss parameter C_1 = 0.0125 for upper curves and 0.25 for the lower curves. The collision parameter C_3 = 5.9×10^2 and the diffusion parameter C_4 = 4.5×10^2.

(See Table 2.3 for explanation of C_1, C_3, and C_4)

FIR OUTPUT POWER VS PRESSURE
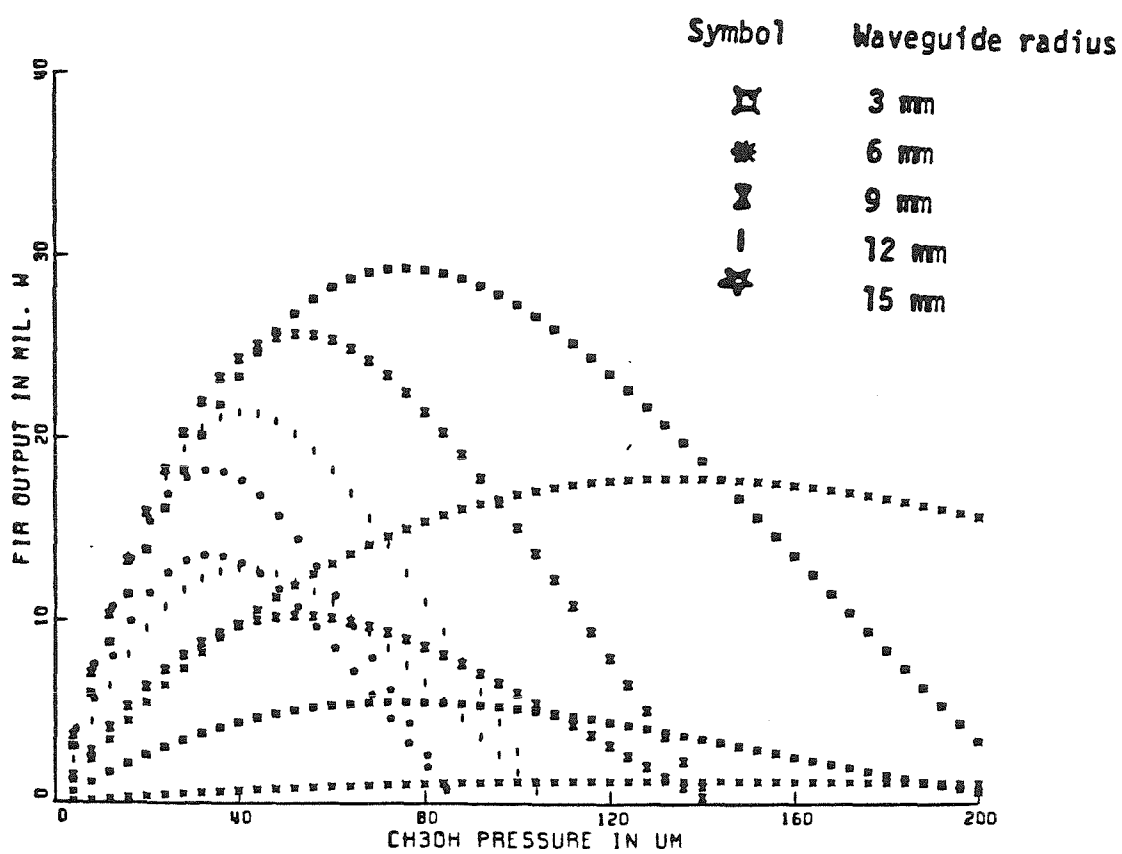
Fig. 2.6. Performance of CH_3OH 118.8 μm laser as estimated by simple phenomenological model. Collisional contribution enhanced (C_3 = 5.9x10^4) by 100-fold as compared to Fig. 2.5.

FIR OUTPUT POWER VS PRESSURE
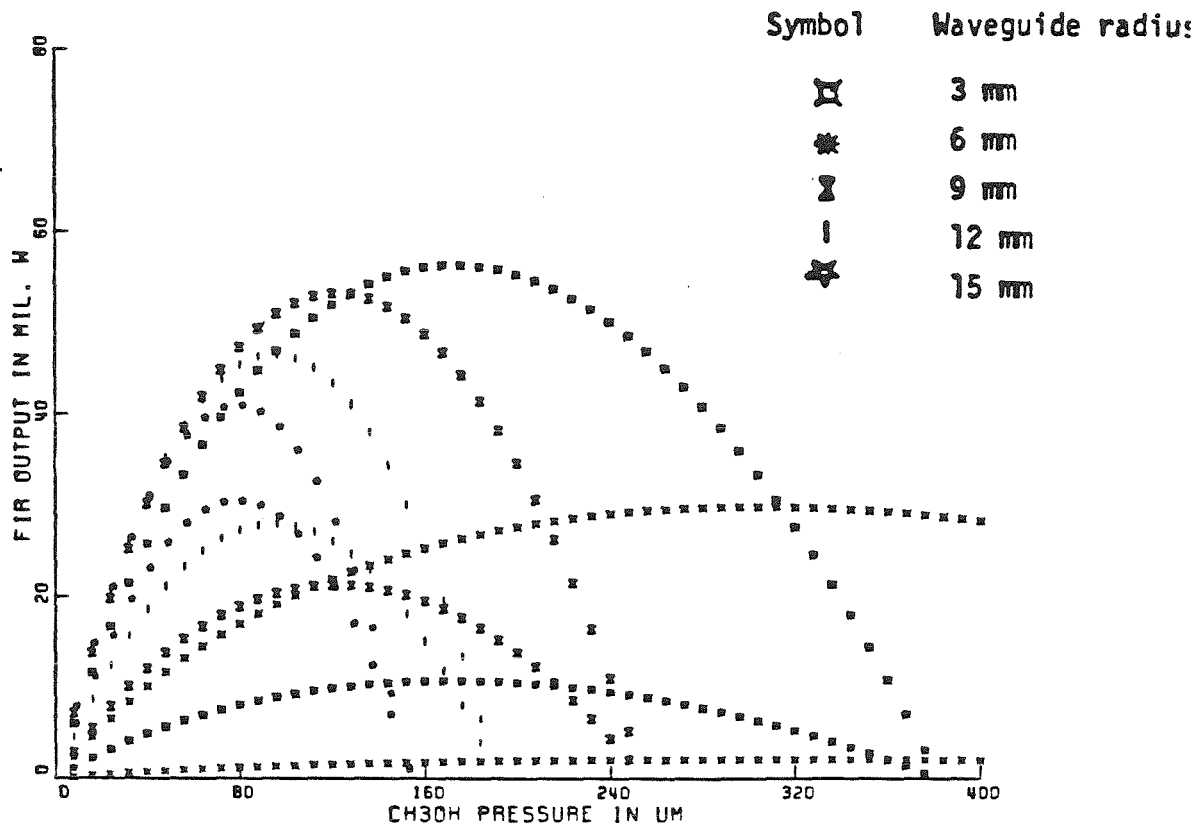

Fig. 2.7. Performance of CH_3OH 118.8 μm laser as estimated by simple phenomenological model. Diffusional contribution to vibrational relaxation enhanced (C_4 = 4.5x10^3) by 10-fold as compared to Fig. 2.5.

2.4 A Simplified Result of Lourtioz and Adde Model.

Following the approach of DeTemple and Danielewicz [9], based on a set of rate equations that take into account all the processes illustrated in Fig.2.2, and using the results of Rigrod's theory [23], the following expression for FIR laser output power was obtained by Lourtioz and Adde [12]

$$
P_{FIR} = T\,S\,I_{FIR} \left[\frac{1}{1+g_2/g_3}\ \frac{\nu_{FIR}}{\nu_{IR}}\ \frac{P_{IR}}{S}\ \frac{\gamma L}{\gamma L + A_p}\ \frac{(1-A_e)}{T+A_F} \right.
$$

$$
\left. \times \frac{1}{1 + \dfrac{\lambda_{IR}}{\lambda_{FIR}}\dfrac{(1+2I_{IR}/I_0)^{\frac{1}{2}}}{(1+2I_{FIR}/I_{SAT})^{\frac{1}{2}}}}\ \frac{1}{I_{SAT}} - 1 \right]
\tag{2.16}
$$

where I_{SAT} is the FIR saturation intensity defined by

$$
I_{SAT} = \frac{4\pi^3 h c\,\Delta\nu_H^2\,\tau_{spont}}{(1+g_2/g_3)\,\lambda_{FIR}^3},
\tag{2.17}
$$

and the circulating FIR intensity I_{FIR} is related to the FIR output power by

$$
P_{FIR} = 2TSI_{FIR}.
\tag{2.18}
$$

where $S=\pi a^2$ is the cross-sectional area of the waveguide (assuming uniform output coupling through out the whole aperture). I_0 and I_{IR} are the corresponding parameters at pump wavelength: I_{IR} is related to the pump power and pump loss by $I_{IR}=\frac{1}{2}P_{IR}/S/(\gamma L+A)$, and I_0 is defined by $\gamma=\gamma_0/(1+I_{IR}/I_0)$, where γ_0 is the small-signal absorption coefficient, and γ is its saturated version. A_e is related to the excited state FIR re-absorption and is given by

$$
A_e = \Gamma_j \left(\frac{g_2}{g_3}f_3 - f_2 \right) \left(\frac{1}{\Gamma} + N_0 f_u^o \frac{h\nu_{IR}}{2I_{IR}\gamma} \right) \rho(\delta v/\Delta v)
\tag{2.19}
$$

where f_u^o is the equilibrium fraction of the upper vibrational state referred to the total number of molecules per unit volume N_0.

$$\rho(\frac{\delta v}{\Delta v}) = \int_{-\infty}^{\infty} f(v)\alpha(v,\nu_{FIR})dv \qquad (2.20)$$

with

$$\alpha(v,\nu_{FIR}) = \alpha_o(v,\nu_{FIR}) / (1 + 2 \frac{I_{FIR}}{I_{SAT}}\alpha_o(v,\nu_{FIR})) \qquad (2.21)$$

$$\alpha_o(v,\nu_{FIR}) = \frac{\lambda^2_{FIR}(\Delta\nu_H/2)^2}{v^2 + \lambda^2_{FIR}(\Delta\nu_H/2)^2} \qquad (2.22)$$

The Maxwellian velocity distribution is given by $f(v)$ with a width $2\Delta v = 2\sqrt{KT/m}$, which is related to the Doppler widths of the pump and FIR transitions through $2\Delta v = \lambda_{IR}\Delta\nu_{D,IR} = \lambda_{FIR}\Delta\nu_{D,FIR}$

Note that since I_{FIR} is related to P_{FIR} by equation (2.18), equation (2.16) is in fact a very complicated implicit equation for P_{FIR}. Ideally, if one can carefully incorporate the dependence on pressure and waveguide diameter of each factor on the right hand side of equation (2.16) and use numerical integration and an iteration approach to solve the implicit equation for P_{FIR}, one can obtain the dependence of FIR output power on pump power, active gas pressure, waveguide diameter and output mirror transmittance, provided that all the molecular and spectroscopic constants as well as the loss parameters are known. Unfortunately, such a "brute force" approach, if not practically impossible, turns out to be extremely difficult. An alternative is of course to seek for reasonable approximations to simplify the equation to make it practically manageable.

A giant step that enormously simplifies the mathematics is to ignore the FIR excited state absorption term by setting $A_e = 0$. The effect of this simplification will be discussed at the end of this section. With $A_e = 0$, eqn. (2.16) takes the simple form

$$y = \left[\frac{b_1}{1 + \dfrac{b_2}{[1+y]^{\frac{1}{2}}}} - 1 \right] \tag{2.23}$$

where

$$b_1 \equiv \left[\frac{1}{1 + g_2/g_3} \right] \left(\frac{\nu_{FIR}}{\nu_{IR}} \right) \left(\frac{P_{IR}}{s} \right) \left(\frac{\gamma L}{\gamma L + A_p} \right) \left(\frac{1}{A_F + T} \right) \frac{1}{I_{SAT}} \tag{2.24(a)}$$

$$b_2 \equiv \frac{\lambda_{IR}}{\lambda_{FIR}} \left(1 + \frac{I_{IR}}{I_o} \right)^{\frac{1}{2}} \tag{2.24(b)}$$

$$y \equiv \frac{2I_{FIR}}{I_{SAT}} \equiv \frac{P_{FIR}}{T \, S \, I_{SAT}} \tag{2.25}$$

By straightforward algebra, we obtain

$$(1+y) + b_2[1+y]^{\frac{1}{2}} - b_1 = 0$$

$$[1+y]^{\frac{1}{2}} = (-b_2 + [b^2_2 + 4b_1]^{\frac{1}{2}})/2 \tag{2.26}$$

Note that the negative root $(-b_2 - [b^2_2 + 4b_1]^{\frac{1}{2}})/2$ is ignored, because

$$[1+y]^{\frac{1}{2}} \equiv [1 + \frac{2I_{FIR}}{I_{SAT}}]^{\frac{1}{2}} > 0.$$

From eqns. (2.25) and (2.26), the FIR output power P_{FIR} can be expressed as

$$P_{FIR} = TSI_{SAT} \left(\frac{[-b_2 + (b^2_2 + 4b_1)^{\frac{1}{2}}]^2}{4} - 1 \right), \tag{2.27}$$

where $s = \pi a^2$ is the waveguide cross-sectional area and b_1 and b_2 are defined by equations 2.24(a) and 2.24(b).

Using equation 2.27, with b_1 and b_2 given by 2.24(a) and 2.24(b), we re-investigate the dependence of FIR output power on pump power, active gas pressure and waveguide diameter for CH_3OH 118 μm line and CH_3F 496 μm line. In addition to the parameters used in the previous model (values of which are

listed in Table 2.3) we have used the known values of saturation intensity for both the pump and FIR transition as listed in Table 2.4.

The results for CH_3F 496 μm line are shown in Fig. 2.8 through Fig. 2.10 and the corresponding results for CH_3OH 118 μm line are shown in Fig. 2.11 through Fig. 2.13. By comparing these figures, it can been seen that for the same waveguide loss parameter the general trend of the corresponding curves is about the same with the following distinctive quantitative features:

(1)   The FIR output for CH_3OH 118 μm line is about 4 to 5 times higher than CH_3F 496 μm line, as expected from the quantum efficiency factor

(2)   The optimum pressure as well as the cutoff pressure for 118 μm line is about twice that for 496 μm line.

Strictly speaking, it is inappropriate to compare performance of the two laser lines for the same waveguide loss parameter as explained in the previous section. Because of the λ^2/a^3 dependence of waveguide loss, 118 μm line is expected to be about 17 times lossier than 496 μm line for the same waveguide radius, and it is, therefore, more appropriate to compare Fig. 2.10 with Fig. 2.11. This reveals that for a given waveguide radius, different performance of the two laser lines may largely be due to the λ^2 dependence of waveguide loss. The 496 μm laser line should be favored by a large waveguide radius because of the large loss factor. Within the range of pump power and waveguide radius under investigation (pump power ~ 5 W to 15 W, waveguide radius ~ 3 mm to 15 mm) the optimum FIR output for CH_3OH 118 μm line may be as high as 12 times that for CH_3F 496 μm line.

In order to estimate the effect of excited state FIR absorption processes (see equation 2.19) we repeat the computation for the CH_3OH 118 μm line with values of all the parameters identical to those given by Lourtioz and Adde [12], and

Table 2.4

Pump and FIR Saturation Intensity
for
CH_3OH 118 μm Laser and CH_3F 496 μm Laser

	CH_3OH 118 μm	CH_3F 496 μm
Pump Saturation Intensity I_o	169 W/cm^2/Torr (Ref.2.24)	6800 W/cm^2/Torr (Ref.2.10 & 2.25)
FIR Saturation Intensity I_s	2.5 W/cm^2/Torr (Ref.2.12)	3.7 W/cm^2/Torr (Ref.2.20)

FIR OUTPUT POWER VS PRESSURE

Fig. 2.8 Performance of CH_3F 496 μm laser as estimated by the simplified Lourtioz and Adde model (waveguide loss parameter C_1 = 0.0125).

For each waveguide radius, pump power = 15 W for the upper curve
10 W for the middle curve
5 W for the lower curve

FIR OUTPUT POWER VS PRESSURE

Fig. 2.9 Performance of CH_3F 496 μm laser as estimated by the
simplified Lourtioz and Adde model (waveguide loss
parameter C_1 = 0.025).

For each waveguide radius, pump power = 15 W for the upper curve
10 W for the middle curve
5 W for the lower curve

FIR OUTPUT POWER VS PRESSURE

Fig. 2.10   Performance of CH_3F 496 μm laser as estimated by the
            simplified Lourtioz and Adde model (waveguide loss
            parameter C_1 = 0.25).

For each waveguide radius, pump power = 15 W for the upper curve
                                       10 W for the middle curve
                                        5 W for the lower curve

FIR OUTPUT POWER VS PRESSURE

Fig. 2.11 Performance of CH_3OH 118 μm laser as estimated by the
simplified Lourtioz and Adde model (waveguide loss
parameter C_1 = 0.0125).

For each waveguide radius, pump power = 15 W for the upper curve
10 W for the middle curve
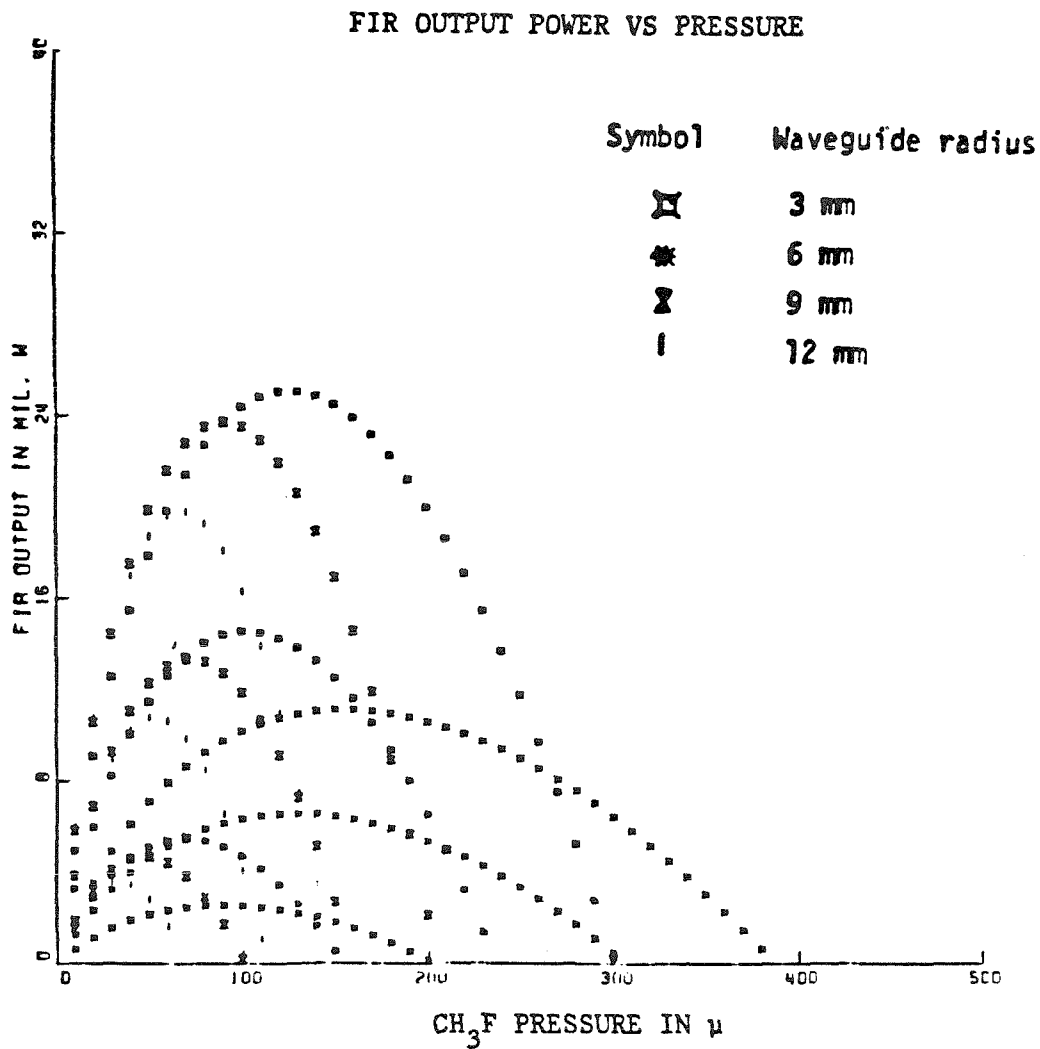5 W for the lower curve

Fig. 2.12   Performance of CH$_3$OH 118 µm laser as estimated by the
simplified Lourtioz and Adde model (waveguide loss
parameter C$_1$ = 0.025).

For each waveguide radius, pump power = 15 W for the upper curve
10 W for the middle curve
5 W for the lower curve

Fig. 2.13 Performance of CH_3OH 118 μm laser as estimated by the
simplified Lourtioz and Adde model (waveguide loss
parameter C_1 = 0.25).

For each waveguide radius, pump power = 15 W for the upper curve
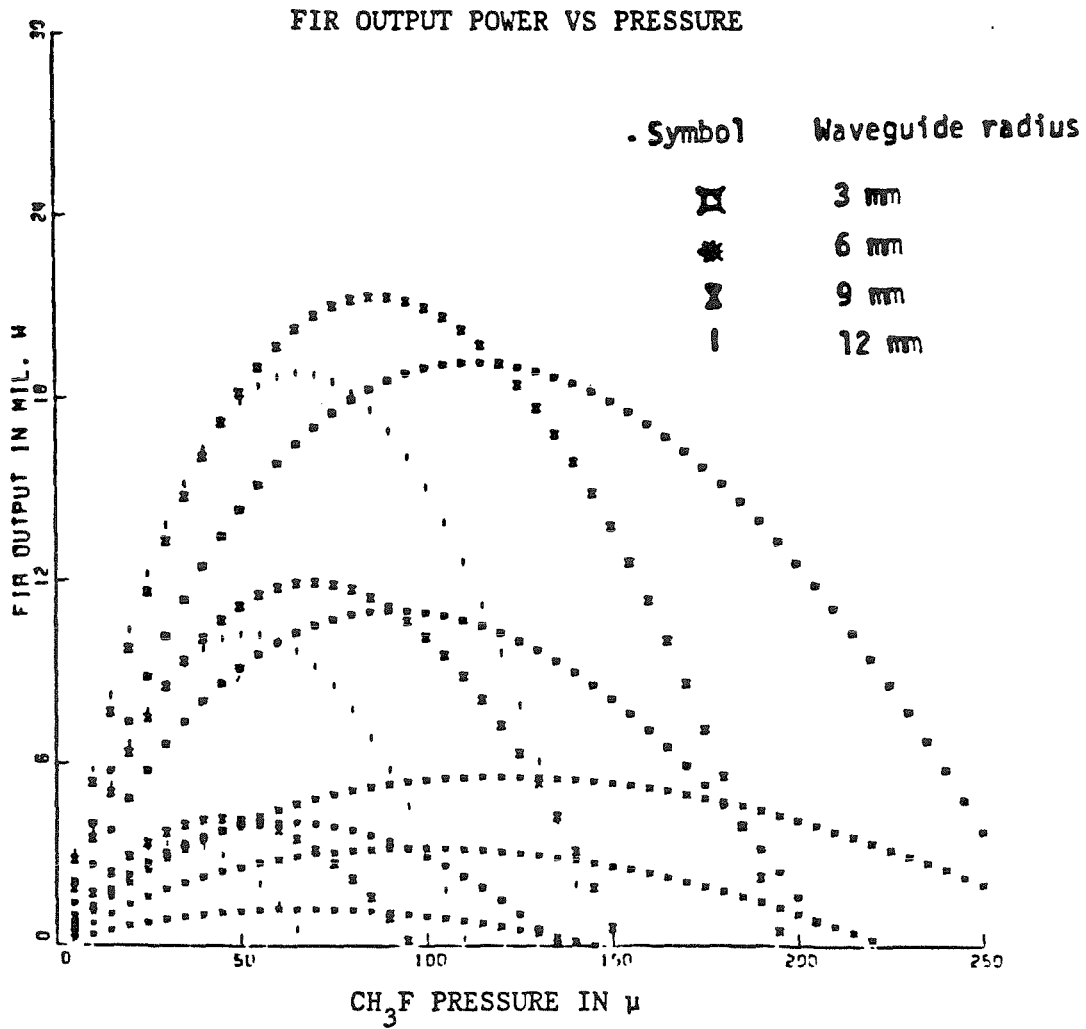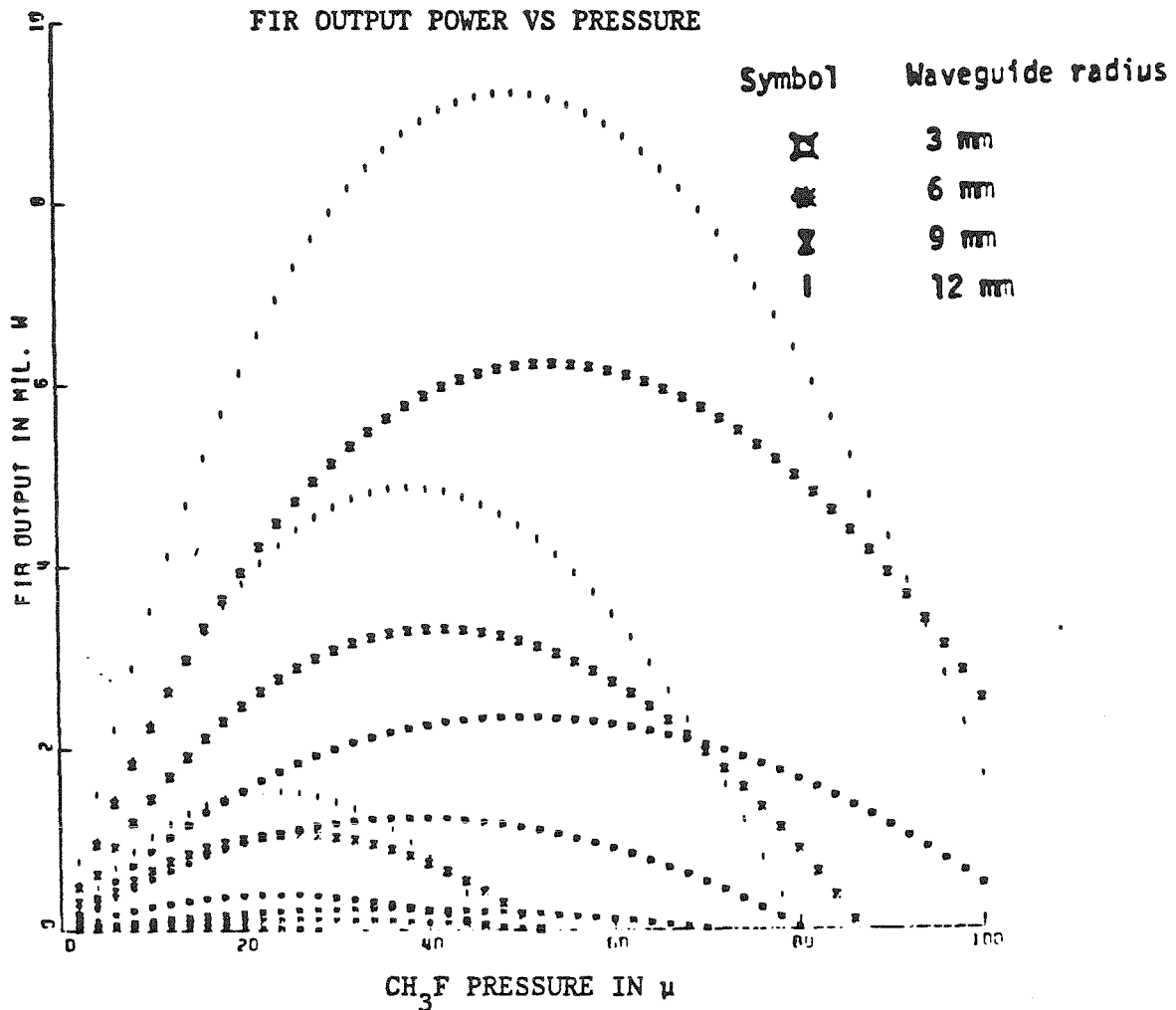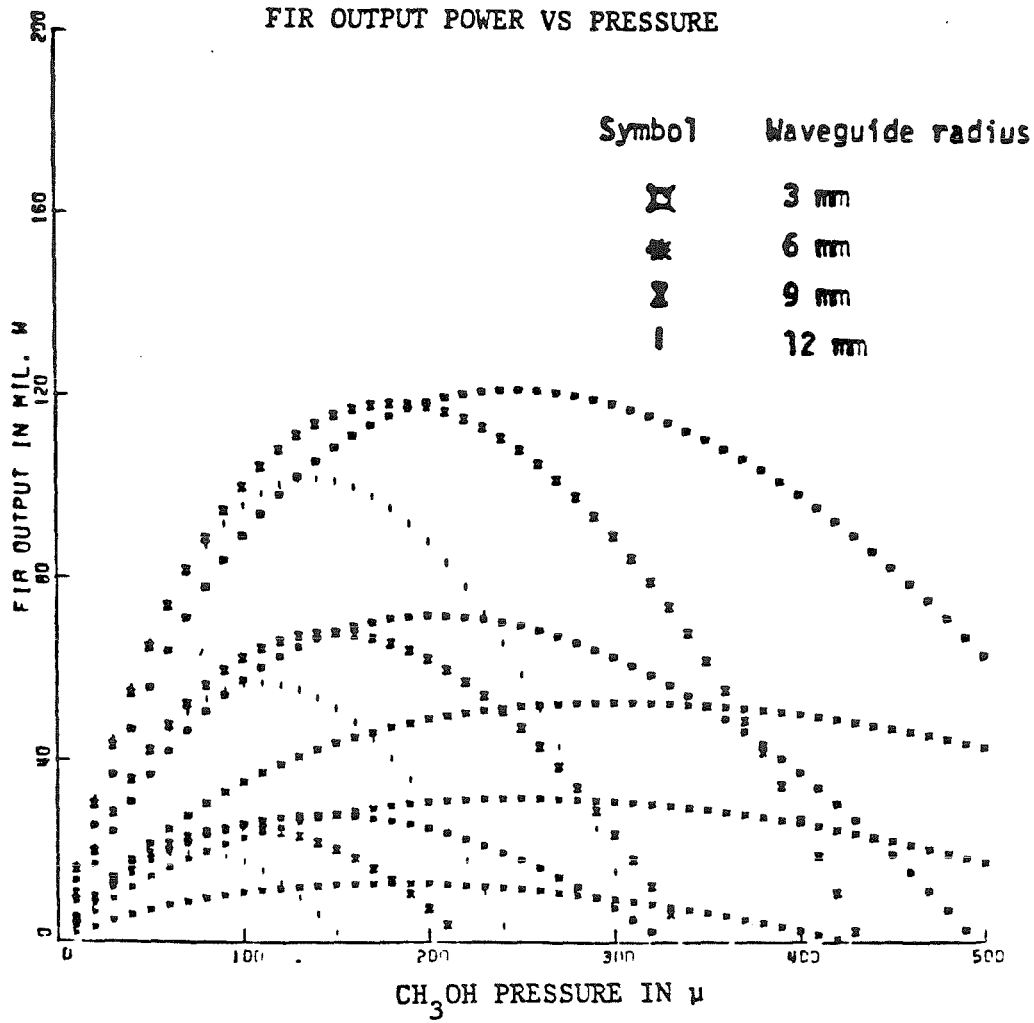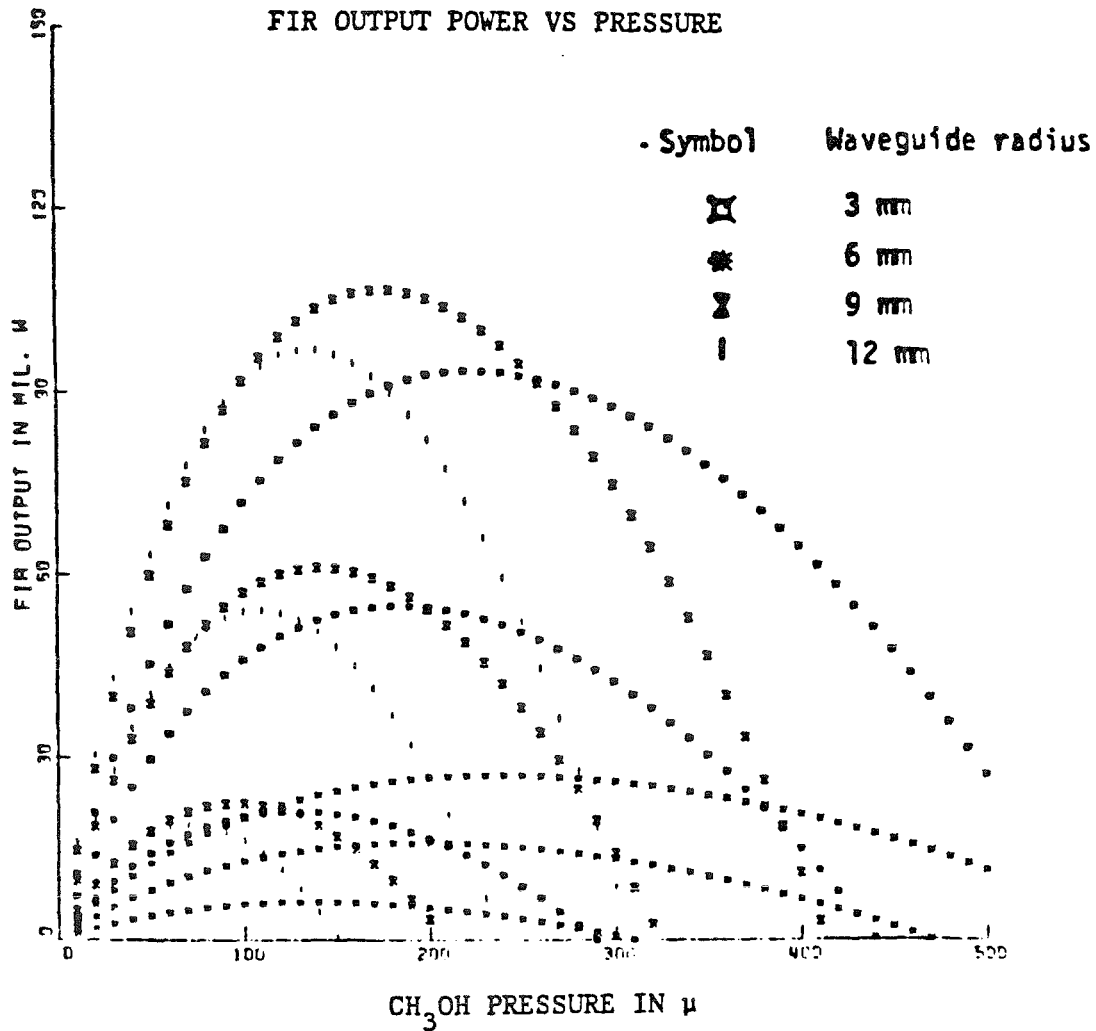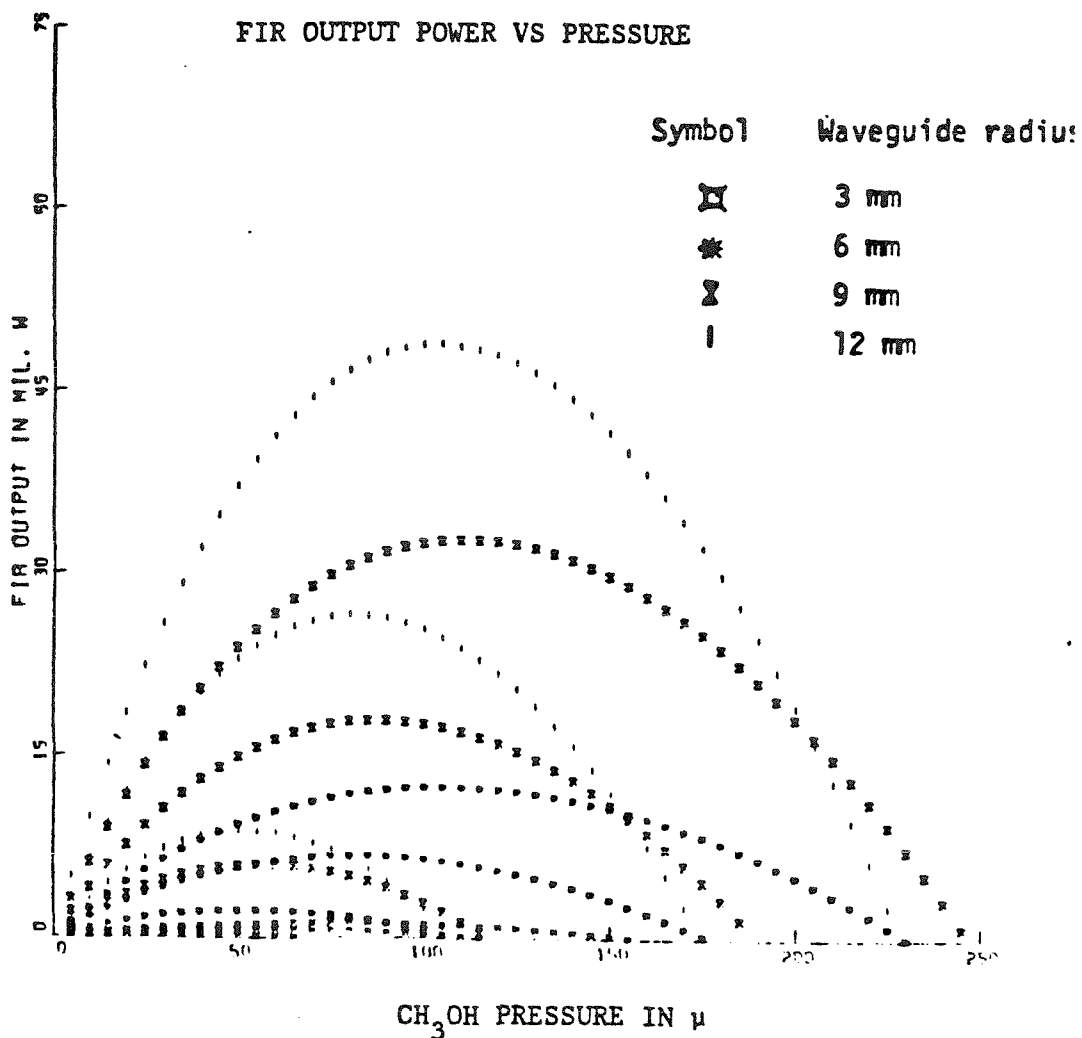10 W for the middle curve
5 W for the lower curve

again we ignore the excited state FIR absorption term by setting $A_e=0$. The results are shown in Fig. 2.14. Comparison of Fig. 2.14 with the result reported by Lourtioz and Adde (reproduced here as Fig. 2.15 for convenience) indicates that excited state FIR absorption may significantly reduce both the output power and the cutoff pressure. Although Lourtioz and Adde have shown that the effect is more significant in the region of small pump power and high operating pressure, its dependence on waveguide radius has not been reported.

2.5 Summary of the Major Results.

Two different models, Hodges' pheonomenological model and Lourtioz and Adde model, were used in section 2.3 and 2.4 to analyzed FIR laser performance. Qualitative pressure dependences of FIR output power predicted by the two models are similar in the sense that there exists an optimum pressure at which the FIR output is maximum, and a cutoff pressure beyond which the FIR laser output is zero. Another common feature is that both the optimum and the cutoff pressures are inversely proportional to the waveguide diameter in most of the range of parameters under investigation.

Quantitatively, the following differences could be noted :

(1) In the simple phenomenological model, the pump power enters the expression for FIR output only as a scaling factor (see equation (2.14)) and affects neither the optimum pressure nor the cutoff pressure. In Lourtioz and Adde model, the dependence on pump power of both the optimum and the cutoff pressures is approximately linear.

(2) In the simple phenomenological model, both the cutoff and the optimum pressures are essentially determined by the diffusional contribution to vibrational relaxation. The cutoff pressure, the optimum pressure and the FIR output power are all approximately doubled when the diffusional contribution to
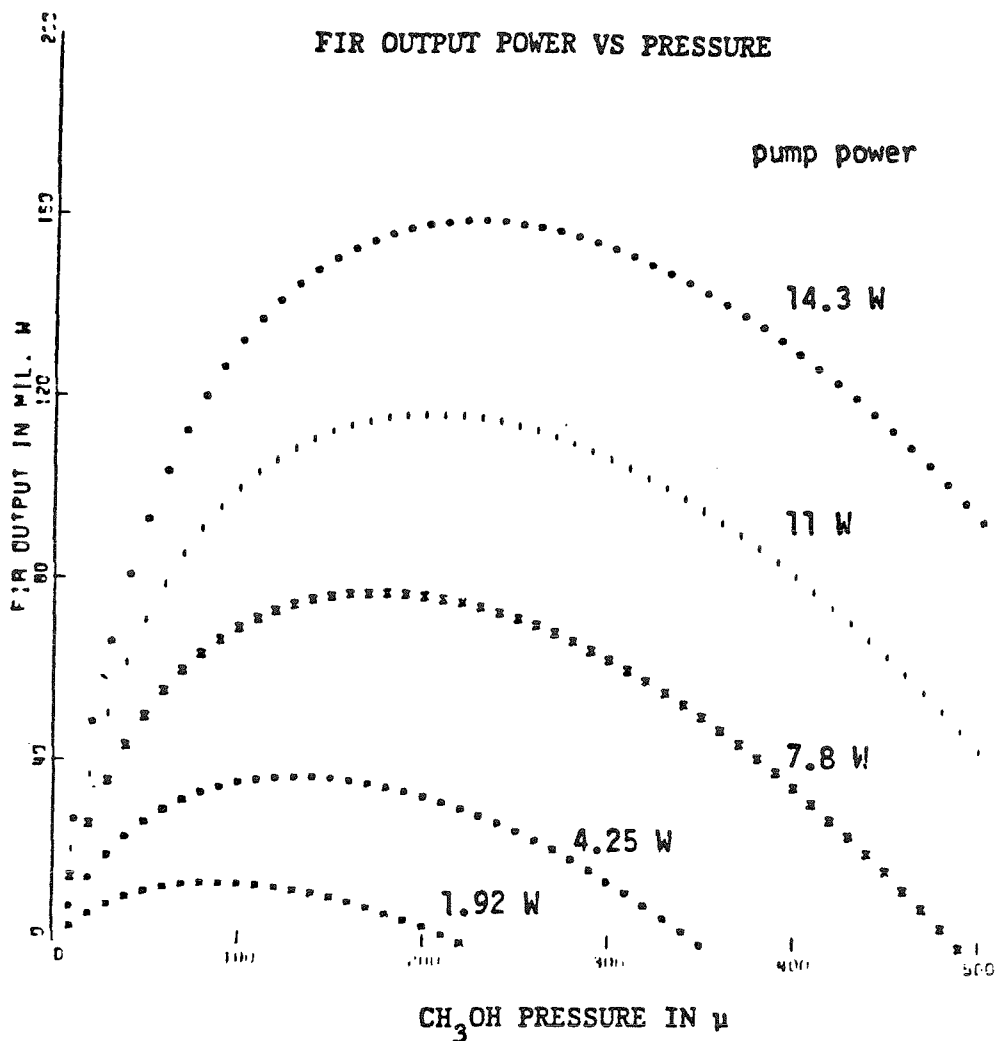
Fig. 2.14 Performance of CH_3OH 118 µm laser as estimated by Lourtioz and Adde model. Values of parameters identical to those reported by Lourtioz and Adde [2.12] are used with the exception that A_e is set to zero to estimate the effect of excited state FIR absorption.
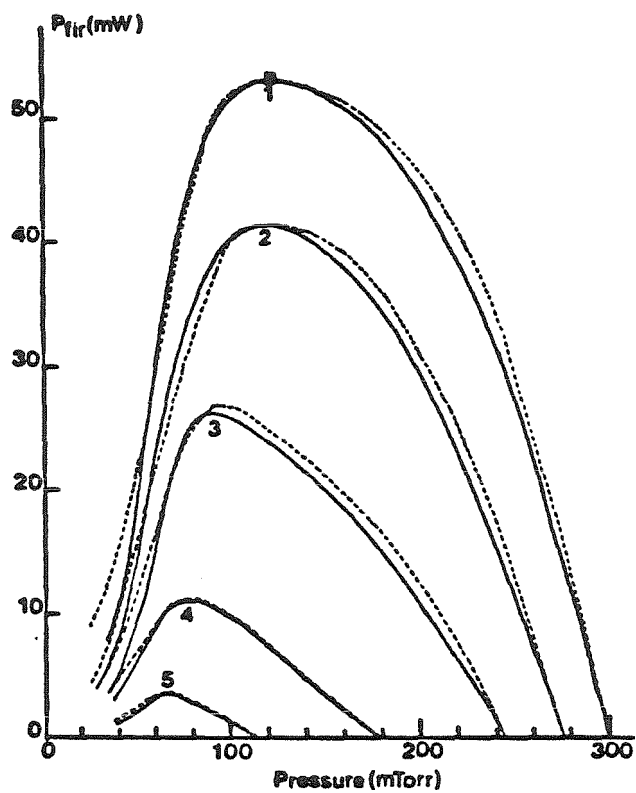
Fig. 2.15   Performance of CH_3OH 118 μm laser (after Lourtioz and
Adde [2.12]).   Values of pump power are : 1) 14.3W,
2) 11W, 3) 7.8W, 4) 4.25W, 5) 1.92W.
Full lines : experiment,   dotted lines : theory.

vibrational relaxation is increased by a factor of ten. In the Lourtioz and Adde model, higher FIR frequency for CH_3OH 118 μm line relative to CH_3F 496 μm line turns out to be the major factor responsible for higher FIR output and higher optimum and cutoff pressures of the former relative to the latter. The contribution from vibrational relaxation, although included in the original expression (equation (2.16)), was completely ignored in the final calculation.

Performances of CH_3F 496 μm laser predicted by the two models agrees reasonably well with each other, considering all the approximation involved. As for the CH_3OH 118 μm line, however, we have to assume that the diffusional contribution to vibrational relaxation is almost ten times larger than that for CH_3F 496 μm line in order to get reasonable agreement between the two models.

Comparison with the experimental results and a more elaborate discussion on the two models will be given in Chapter 6.

References for Chapter 2

2.1 D.T. Hodges, "The FIR waveguide laser - a practical source," *SPIE*, Vol.67, 1975, pp. 41-47.

2.2 L.Frenkel, H.Marantz, & T.Sullivan, "Spectroscopy and collisional transfer in CH_3Cl by microwave-laser double resonance," *Phys. Rev.*, A, 3, 1976 pp. 1640-1651.

2.3 R.L.Shoemaker, S.Stenholm, & R.G.Brewer, " Collision-induced optical double resonance," *Phys. Rev.*, A, 10, 1974, pp. 2037-2054.

2.4 J.W.C.John et al., " Collision-induced Lamb dips in laser Stark spectroscopy," *J. Chem. Phys.*, 62, 1975, pp. 1488-1496.

2.5 E.Weitz & G.W.Flynn, " Partial vibration energy transfer map for methyl fluoride: A laser fluorescence study," *J. Chem. Phys.*, 58, 1973, pp. 2781-2793.

2.6 J.R.Tucker, "Theory of an FIR gas laser ," *Int. conf. on sub-millimeter wave and their applications*, Georgia, Atlanta, June 1974, pp. 17-18.

2.7 J.O. Heningsen and H.G. Jensen, "The optically pump FIR laser : rate equations and diagnostic experiments," *IEEE. J. Quantum electron.*, Vol. QE-11, No. 6, June 1975, pp.248-252.

2.8 R.J.Temkin & D.R.Cohen, "Rate equation for an optically pumped far infrared laser," *Optics Commun.*, Vol. 16, No. 2, Feb. 1976, pp. 213-217.

2.9 T.A.DeTemple & E.J.Danielewicz, "CW CH_3F waveguide laser at 496 μm :Theory and experiment," *IEEE J. Quantum Electron.*, Vol. QE-12, No. 1, Jan. 1976, pp. 40-47.

2.10 G.A.Koepf & K.Smith, "The cw-496 μm methylfluoride laser: Review and theoretical predictions," *IEEE J. Quantum Electron.*, Vol. QE-14, No. 5, May 1978, pp. 333-338.

2.11 Y. Kokubo and etal, "CW CH_3F metallic waveguide laser at 496 μm," *The Trans. of The IECE of Japan*, Vol. J64-C, No.1, Jan. 1981, pp. 16-23.

2.12 J.M. Lourtioz and R. Adde, "Diagnostic experiments and modeling of 118 μm CH_3OH laser," *J. Physique*, 41, March 1980, pp.251-258.

2.13 D. Seligson *et al.*, "Quantum mechanical features of optically pumped cw FIR lasers," *IEEE J. Quantum Electron.*, Vol. QE-13, No. 6, June 1977, pp. 468-472.

2.14 R.J. Temkin, "Theory of optically pumped submillimeter lasers," *IEEE J. Quantum Electron.*, Vol. QE-13, No. 6, June 1977, pp. 450-454.

2.15 Z. Drozdowicz, R.J. Temkin and B. Lax, "Laser pumped molecular lasers - Part I : Theory," *IEEE J. Quantum Electron.*, Vol. QE-15, No. 3, March 1979, pp. 170-178.

2.16 Z. Drozdowicz, R.J. Temkin and B. Lax, "Laser pumped molecular lasers - Part II : Submillimeter laser experiments," *IEEE J. Quantum Electron.*, Vol. QE-15, No. 9, Sept. 1979, pp. 865-869.

2.17 J. Heppner *et al.*, "Gain in cw laser pumped FIR laser gases," *IEEE J. Quantum Electron.*, Vol. QE-16, No. 4, April 1980, pp. 392-401.

2.18 A.Yariv, **Quantum Electronics**, 2nd Ed., John Wiley & Sons, Inc., New York, 1975, Chapter 8.

2.19 D.T.Hodges, "A review of advances in optically pumped FIR lasers," *Infrared Physics*, Vol.18, 1978, pp. 375-384.

2.20 D.T.Hodges, J.R.Tucker, & T.S.Hartwick, "Basic physical mechanisms determining performance of the CH_3F laser," *Infrared Physics*, Vol.16, 1976, pp. 175-182.

2.21 E.A.J.Marcatili & R.A.Schmeltzer,"Hollow Metallic and dielectric waveguide for long distance optical transmission and lasers," *Bell System Tech. J.*, Vol.43, 1964, pp. 1783-1809.

2.22 C.H.Townes and A.L.Shawlow, **Microwave Spectroscopy**, McGraw-Hill Book Co. Inc., New York, 1955, Chapter 3.

2.23 W.W. Rigrod, "Gain saturation and output power of optical masers," *J. Appl. Phys.*, Vol. 34, No. 9, Sept. 1963, pp. 2602-2609.

2.24 C.O. Weiss, "Pump saturation in molecular far-infrared lasers," *IEEE J. Quantum Electron.*, Vol. QE-12, No. 10, Oct. 1976, pp. 580-584.

2.25 D.T. Hodges and J.R. Tucker, "Pump absorption and saturation in CH_3F 496 μm laser," *Appl. Phys. Lett.*, Vol. 27, No. 12, Dec. 1975, pp. 667-669.

CHAPTER 3. FIR LASER STABILIZATION

3.1 Introduction to the Stability Problem.

Since the birth of optically pumped FIR lasers, the relatively poor stability of the FIR output power has been one of the factors that discourages its use in wide varieties of applications.

It is expected that the thermal drift of the FIR cavity length will introduce only a long term power drift which can be reduced by utilizing material with a small thermal expansion coefficient such as invar to construct the mechanical support structure. Furthermore such a simple length drift would be expected to be easily correctable by simply retuning the FIR cavity length. Detailed experimental studies reveal that the tuning process is much more involved than anticipated and may introduce undesirable frequency pulling effects on the CO_2 laser.

The theory presented in section 2.2 indicated that, because of collisional thermalization, the FIR laser can be operated only at relatively low gas pressure (typically 40 to 450 μm). As a consequence, the frequency characteristics of the absorption are, in general, Doppler-broadened, with relatively narrow line widths of the order of 60 MHz. It should not be surprising that the frequency stability of the CO_2 pump laser turns out to be the most crucial factor that determines the power stability of FIR output.

The characteristics of the CO_2 pump laser output and FIR laser gas absorption are treated in section 3.2 and section 3.3. In section 3.4, the principles and experimental methods of opto-acoustic detection and its use in locking the CO_2 laser frequency to the FIR gas absorption peak are treated in detail. The effects of cavity frequency pulling and cavity isolation are treated in section 3.5. Important experimental results are summarized in section 3.6.

3.2 Characteristics of CO_2 Laser Output.

Virtually all the CO_2 lasers used in optically-pumped FIR laser systems utilize a grating to select a particular vibrational transition. A piezo-electrically driven mount for one of the resonator mirrors is used to fine-tune or modulate the cavity length.

The frequency resolution $\Delta\nu$ of a grating, for any particular grating order "n", can be expressed as $\frac{\Delta\nu}{\nu} = 1/\ nN$, where N is the total number of rulings exposed to the beam [3.1]. For grating with 75 lines/mm and a CO_2 intracavity beam width of 3 to 4 mm, $N \approx 300$.

For a grating mounted in the Littrow configuration [3.2], $|n|=1$

$$|\Delta\nu| \approx \frac{\nu}{|nN|} \approx \frac{3\times10^{13}}{300} \text{ Hz} \approx 100 \text{ GHz}$$

Since the frequency separation between adjacent CO_2 vibrational transitions is about 50 GHz [3.3, 3.4], the grating serves to select a particular line, as illustrated in Fig. 3.1(a).

The free spectral range (FSR) [3.5] of a laser cavity is given by FSR = c/2L ; where c is the velocity of light in free space and L is the cavity length. For a typical cavity length of $\approx$1.5 meter, FSR$\approx$100 MHz. The Doppler width of the CO_2 gain profile is $\approx$53 MHz [3.6] at room temperature, while the collisional width is $\approx$ 5 MHz/torr [3.7]. At the typical operating pressure of approximately 30 torr, the CO_2 gain profile is predominantly collision broadened, with line width of approximately 150 MHz. The features within a specific laser transition are illustrated in Fig.3.1(b).

As the cavity length is changed by varying the piezo-electric tranducer (PZT) voltage, the laser frequency varies accordingly, and the output power more or

(a)

(b)
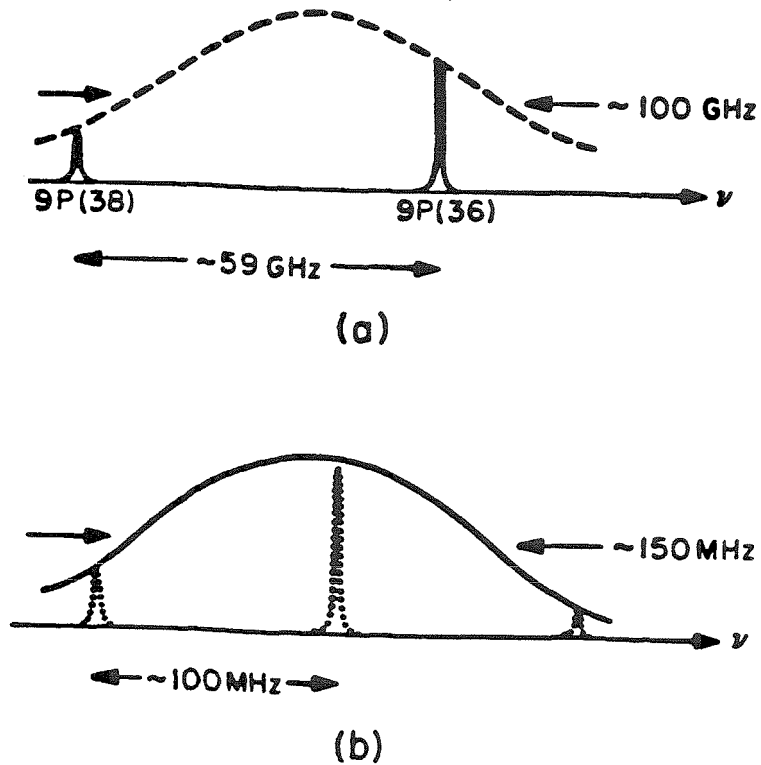
Fig. 3.1.(a)   Comparison of grating reflectivity vs. wavelength and positions of typical CO_2 laser transition.

----   Frequency characteristics of a grating for a particular grating order.

IR pump laser lines (vibrational transitions)

(b)   Comparison of a typical CO_2 laser collision-broadened gain curve with the cavity resonances of a 1.5 meter cavity.

—   Typical gain profile of a CO_2 laser line at gas pressure $\simeq$ 30 Torrs

...   Frequency characteristics of the laser cavity for cavity length $\simeq$ 1.5 meter

less follows the gain profile traversed by one of the cavity resonance peaks to a point where the gain becomes so low that "frequency hopping" to an adjacent cavity peak with much higher gain takes place. This phenomenon appeared consistently in all the CO_2 lasers used in this study [two constructed at Caltech and one commercial unit : Apollo Laser Inc. Model 122]. A typical experimental curve is shown in Fig.3.2.

3.3 Characteristics of Active Gas Absorptions

A typical absorption profile in the vicinity of 9.7 μm for methanol (CH_3OH) vapor at pressure of the order of 200 μ is shown in Fig. 3.3(a) together with the probe laser beam intensity profile and the FIR laser output at 118 μm. These experimental data were taken with the opto-acoustic technique described in the next section. The extremely sharp FIR laser output profile clearly indicates that out of the relatively broad absorption band, only a very narrow range of pump laser frequencies (not resolved in the absorption curve) is effective in creating the population inversion required for the laser action.

The CO_2 output power profile ,the CH_3OH absorption profile, and the FIR output power in Fig. 3.3(a) are sampled at representative points and reproduced in Fig. 3.3(b) together with the normalized absorption signal defined as the absorption signal / pump power. Although the detailed structure of the normalized curve may not be exact due to the noise involved in the original experimental data as well as the sampling process, it does, however, indicate that some fine structure exists within the broad absorption profile. The overall match of the absorption responsible for FIR laser action and the CO_2 power curve results in FIR laser action: on a number of wavelengths. Only the strong 118 μm laser was studied in this investigation, and its optimum pump frequency is indicated in Fig. 3.3 (b). Other FIR lasers exhibit different optimum pump frequencies within

CO_2 output power (arbitrary unit)

PZT driving voltage

≈ 1000 Volts
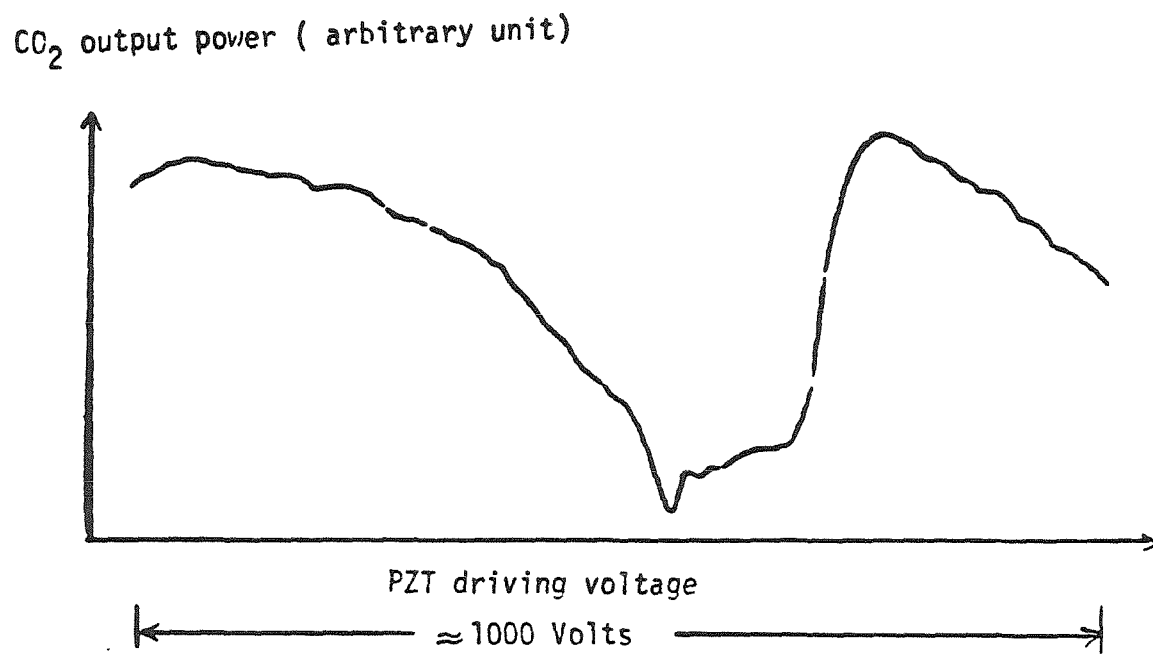
Fig. 3.2 CO_2 laser output power v.s. PZT driving voltage
(typical experimental results).

CO$_2$ LASER
OUTPUT POWER

CH$_3$OH
ABSORPTION
SIGNAL

FIR LASER
OUTPUT POWER

PZT DRIVING
VOLTAGE

0   200   400   600   800   1000 volt
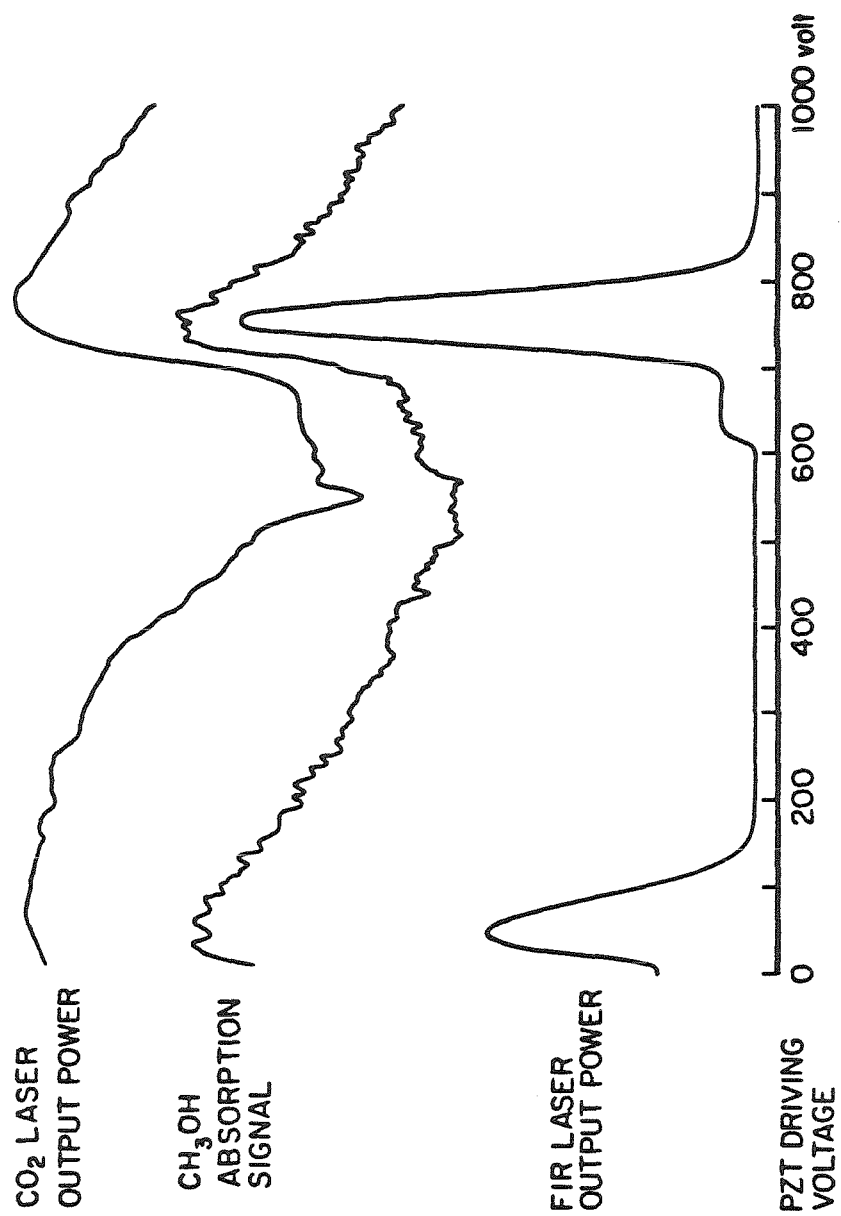
Fig. 3.3(a) CO$_2$ laser output power, CH$_3$OH absorption signal
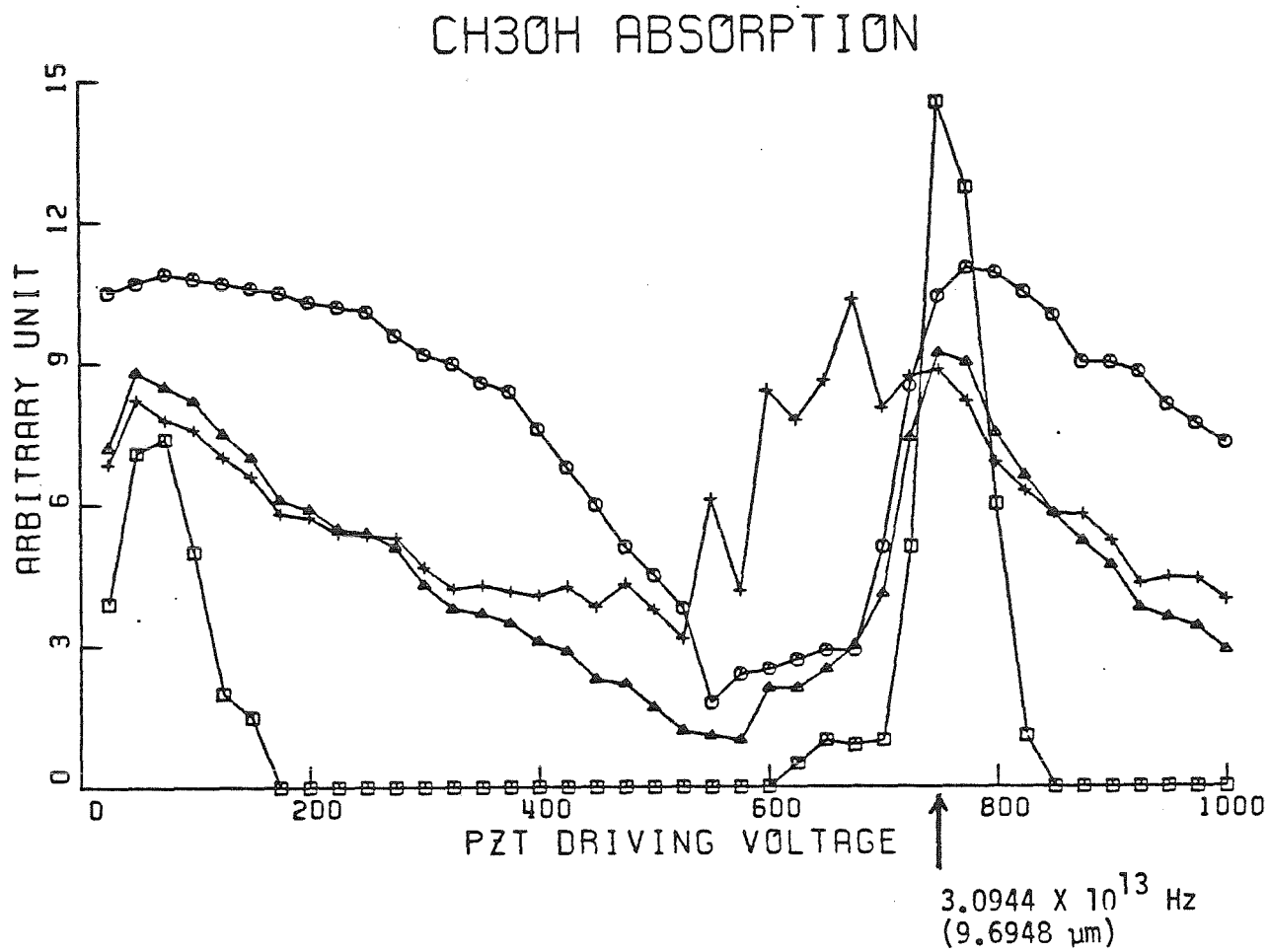and FIR laser output power vs PZT driving voltage.

CH3OH ABSORPTION

Fig. 3.3(b) CO_2 laser output power, CH_3OH absorption signal,

FIR laser output power and normalized CH_3OH absorption

vs PZT driving voltage [discrete sampling of Fig. 3.3(a)].

o : CO_2 pump power;   Δ : CH_3OH absorption signal;
+ : Normalized absorption curve,   □ : FIR output power.

the CO_2 tuning curve, according to their rotational levels.

3.4 Optoacoustic Frequency Locking.

3.4.1 Basic Principles.

The basic idea of the optoacoustic detector or "spectrophone" [3.8, 3.9, 3.10] is to incorporate a microphone in a sample gas cell to sense the pressure variation due to changes in pump laser power absorbted in the gas. Such changes could be produced by modulating the amplitude of the laser pump power. Alternatively, if the amplitude of the pump laser is constant, the amount of the power absorbed can be modulated by changing the frequency of the laser. Since the degree of absorption in the gas is strongly frequency dependent, the amplitude of the pressure variation and hence the microphone signal will depend on the slope of the absorption profile. If the microphone signal is detected by a phase sensitive detector, the integrated dc output of the detector will be as is illustrated in Fig. 3.4. Frequency modulation of the pump laser is typically achieved by applying an a.c. signal on top of a d.c. bias voltage to a piezoelectric transducer (PZT) that controls the position of one the laser cavity reflectors. The first derivative signal can then be used as an error signal to actively correct the d.c. biased voltage on PZT so that the resonance peak of the laser cavity coincides with the peak of the absorption.

3.4.2 Experimental Set-up and Results.

Fig. 3.5 is a schematic diagram of the experimental set-up. The first derivative signal for IR resonance absorption of CH_3OH vapor in the vicinity of 9.7 μm is shown in fig 3.6, together with the FIR laser output power. These experimental curves are obtained by applying an a.c. signal on top of a ramp voltage to dither and scan the CO_2 laser cavity length. Note that the FIR laser lases at points where the first-derivative signal crosses the zero level as indicated by arrows in

BASIC IDEA OF FREQUENCY LOCKING

ABSORPTION PROFILE   ABSORPTION SIGNAL

TIME

SIGNAL FROM PHASE
SENSITIVE DETECTOR

TIME

TIME

CO_2 PZT VOLTAGE

TIME

SINUSOIDAL DITHER
+
RAMP

CO PZT VOLTAGE

FIRST DERIVATIVE SIGNAL
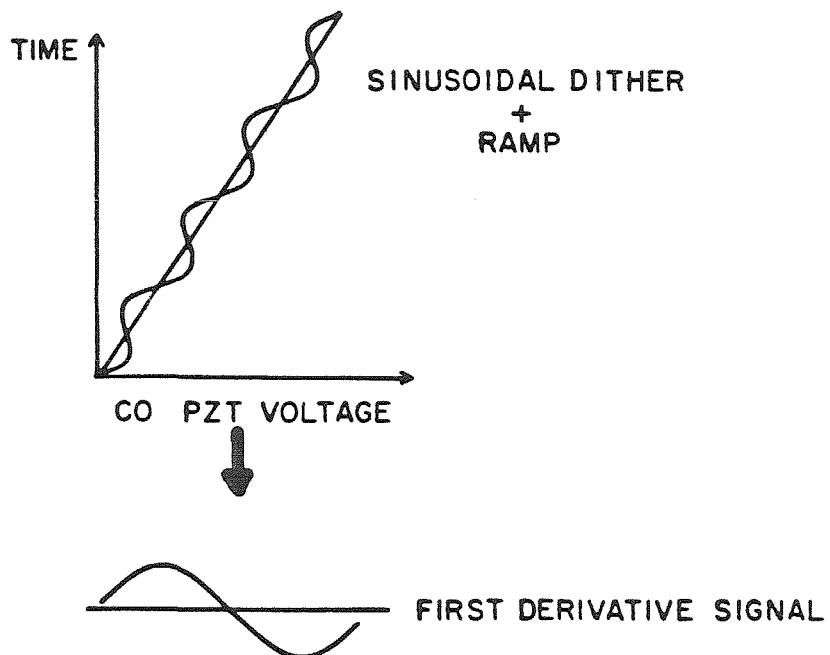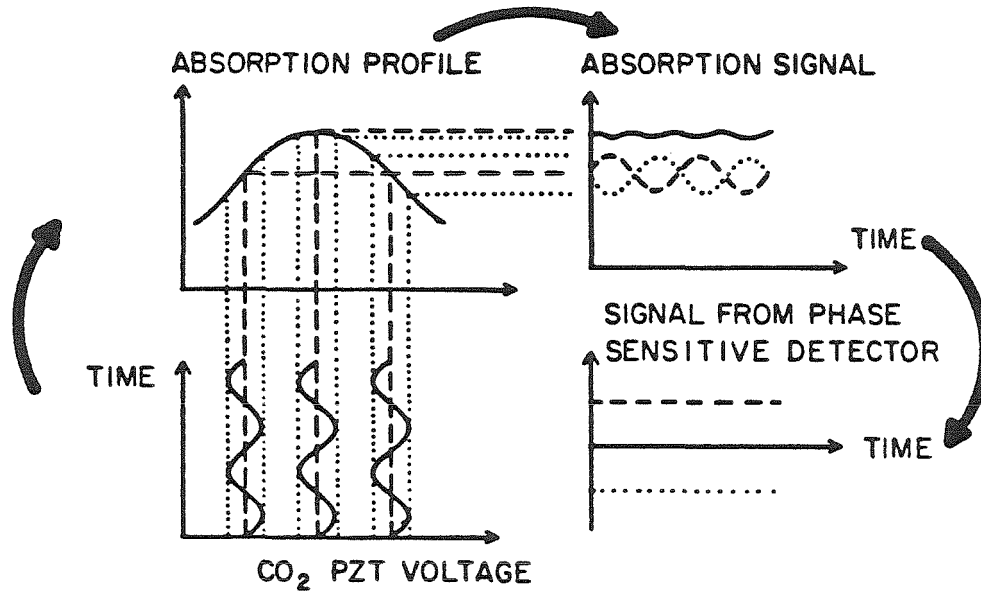
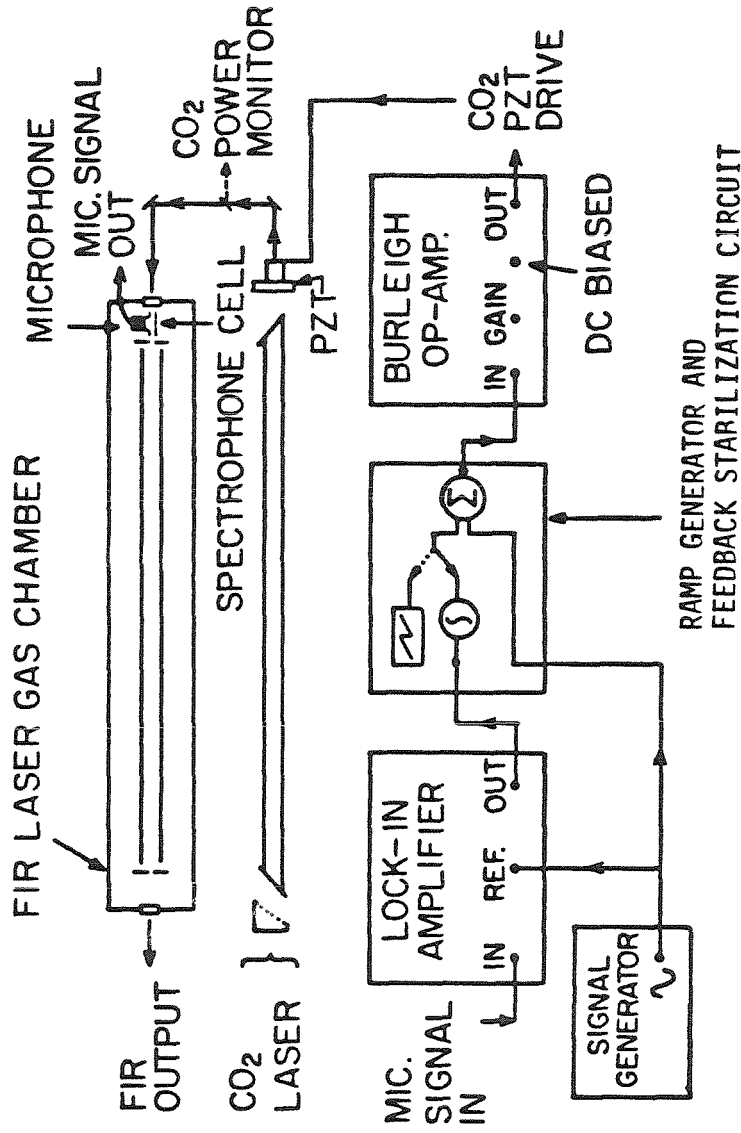Fig. 3.4 Basic idea of opto-acoustic frequency locking.

Fig. 3.5. Schematic diagram of the experimental setup for frequency locking of CO_2 laser to active gas absorption peak.
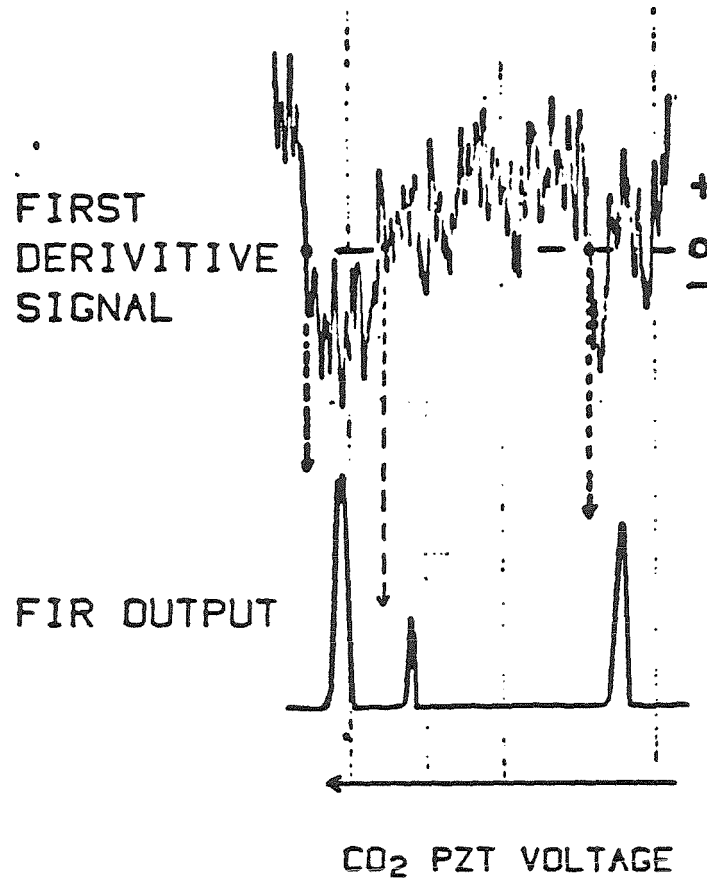
Fig. 3.6 First derivative signal of CH_3OH absorption curve and FIR
laser output power v.s. PZT driving voltage (all in arbitrary
units).The dotted arrows indicate the actual position of the
FIR output peaks.

Fig. 3.5. Obviously, these are the points where the CO_2 laser has to be locked to make the FIR laser lase at that particular frequency.

The FIR output power of the CH_3OH 118 μm line obtained with the active frequency locking of CO_2 laser by optoacoustic method as described above is shown in Fig. 3.7. For comparison, the output power of the same run with the active loop turned off is shown in the same figure. Without active frequency locking, severe FIR power drift due to slow frequency drift of CO_2 laser in time over 10 to 30 min is typical. With the active frequency locking, the FIR laser can typically by operated for hours with short term power fluctuation of the order of $\pm$ 3% and long term power drift of the order of $\pm$ 8%.

If the CO_2 laser cavity length is scanned by applying a ramp voltage to the PZT, without superposition of the a.c. dither signal, and the CO_2 laser beam is chopped, the integrated d.c. signal from the phase sensitive detector will then trace out the absorption profile instead of its first-derivative. The absorption profile shown in Fig.3.3(a) in the previous section is obtained by this procedure.

3.4.3 The Spectrophone.

A spectrophone consists of a gas cell that contains a microphone to sense the pressure variation due to resonance absorption of radiation. It is obviously the key element in the opto-acoustic frequency locking technique. Various properties of the spectrophone in general, and the problems of signal to noise ratio enhancement in particular, had been investigated recently by Kavaya [3.10]. This thesis may be consulted for a detailed theory of operation and S/N performance, as well as a comprehensive guide to previous work. Qualitatively speaking, a smaller cell volume tends to increase the signal to noise ratio and is therefore desirable.

The spectrophone, if properly designed, can be mounted either inside the FIR

frequency locking feedback loop

off   on   off

CO$_2$ laser
pump power

manual frequency
tuning of CO$_2$ laser

FIR laser
output power

CO$_2$ laser zero
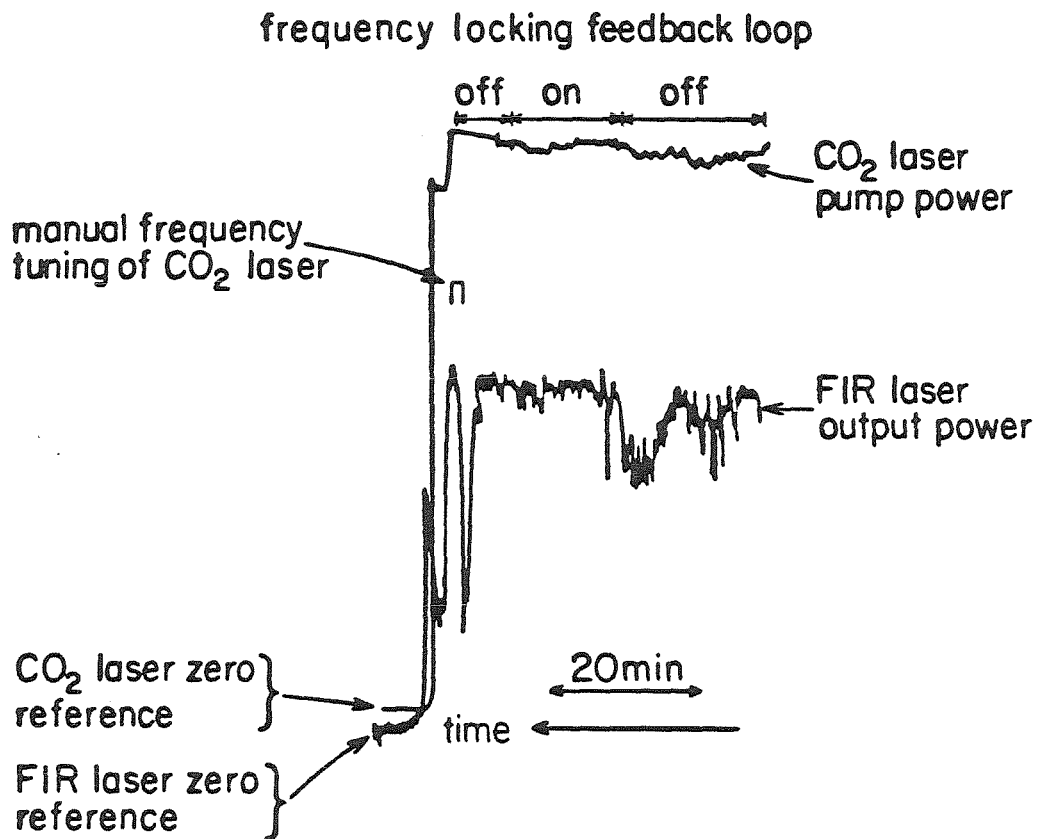reference

20min

FIR laser zero
reference

time

Fig. 3.7 Typical FIR output power stability with and without active
frequency stabilization of pump laser.

laser gas chamber or outside the chamber. A schematic diagram of an extremely simple internal spectrophone and the layout illustrating how it is incorporated in our experimental setup are shown in Fig. 3.8. Some of the advantages and disvantages of an internal spectrophone and an external spectrophone are compared in table 3.1.

3.4.4 Comparison With Other Stabilization Methods.

Some of the other methods that have been used to stabilize the CO_2 laser frequency for FIR laser application are :

(1)   Stabilization feedback loop based on the FIR laser output power [3.11].

(2)   Optogalvanic frequency stabilization of CO_2 laser [3.12] to the center of the CO_2 power curve.

(3)   Frequency stabilization of CO_2 laser to an external Fabry-Parot interferometer [3.13].

The major disadvantage of the first method lies in the fact that any change in the FIR laser output power due to any part or parts of the FIR laser cavity itself will be sensed and fed back to the CO_2 laser, forcing the CO_2 laser to make undesirable frequency adjustment. Furthermore, the feedback loop is active only when the FIR laser is lasing at significant power level. These disadvantages are unacceptable, in particular, for an experimental parametric study of FIR laser, where parameters such as pump power and active gas pressure are among the variables of interest.

The second and third methods, although being very effective in frequency stabilization of the CO_2 laser, are subjected to the drawback that there is nothing inherent to the loops to search or indicate the frequency of the optimum point with respect to the FIR laser gas absorption, and one may have to go through a rather time consuming "trial and error tuning" procedure to find the optimum
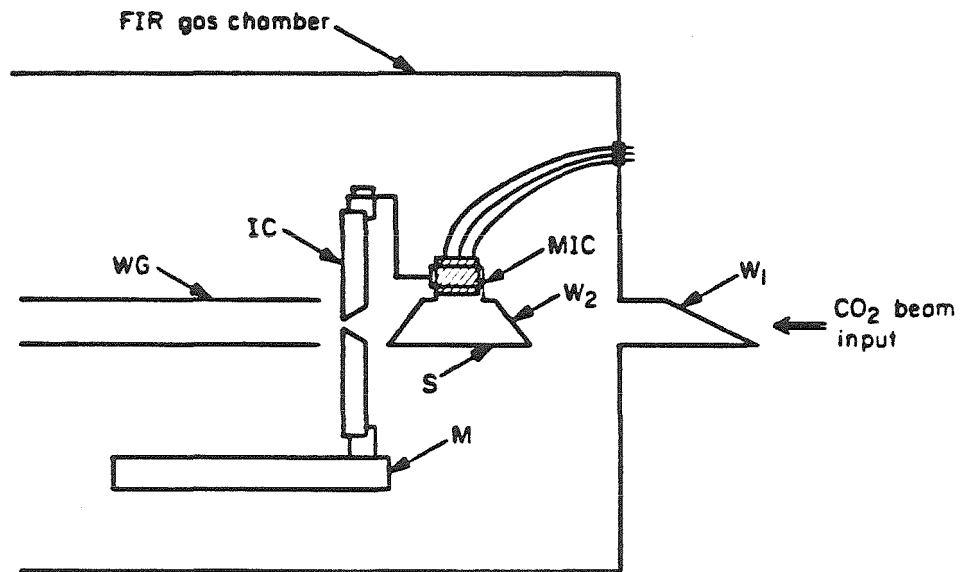
Fig. 3.8 Schematic diagram of the experimental setup incorporating an extremely simple internal spectrophone.

W_1 : ZnSe window at Brewster Angle ;

W_2 : NaCl window at Brewster Angle ;

S : Spectrophone cell ; MIC : microphone ;

IC : input coupling copper morror ; M : input coupler mount ;

WG : pyrex tube waveguide.

Table 3.1

Comparison of Some Advantages and Disadvantages of Internal

and External Spectrophones

Internal Spectrophone	External Spectrophone
Monitoring the absorption siganl of the gas which forms part of the laser media and is therefore in the same physical environment (pressure, temperature ..) as the lasing gas.	Monitoring an independent sample gas cell whose physical enviroment may be different from that of the lasing medium.
Constrainted to the FIR laser operating condition and cannot be controlled independently.	Not coupled to the FIR laser operation and can, therefore, be controlled (varying the parameters) independently.
Some of the useful pumped power is wasted because of the Fresnel reflection at the spectrophone windows as well as absorption of the windows and gas.	Can utilizing the fraction of the pump beam (typically ~ 5% to 10%) split off for power monitoring purposes, with no extra loss of pump power.
Operates on the full pump flux, which maximizes the signal.	Uses only split-off fraction of the pump flux.

point at which the CO_2 laser should be locked.

3.5 Frequency Pulling Effects.

An optically-pumped FIR laser is a laser-pumped-laser system. In the typical experimental setup illustrated schematically in Fig 1.3 or 3.5, there usually exists a significant coupling between the FIR laser cavity and the CO_2 laser cavity by reflection of the CO_2 laser beam from the FIR cavity mirrors.

The output power of the CO_2 laser monitored by the power meter (PM) [see Fig. 3.5] is shown in Fig. 3.9. When the FIR cavity is blocked, the typical short term power fluctuation is less than ± 1%. It jumps to the values of ± 2% to ±5% immediately after the FIR cavity is unblocked and relaxes back to the steady state value in time of the order of a few minutes (for reasons not fully understood). Similar effects have also been observed when a beam attenuator such as a polished rock salt flat or zinc selenide flat is inserted in the CO_2 laser beam path. Occasionally, the effect may be strong enough to drive the CO_2 feedback loop out of lock, so that the PZT driving voltage has to be readjusted manually.

The effect of cavity frequency pulling and a passive isolation method to minimize such an undesirable effect are discussed by Mansfield [3.14]. For the CH_3OH 118 μm line, the effect is, however, much less pronounced than the case reported by Mansfield.

3.6 Conclusion.

To summarize, we conclude that optoacoustic active frequency locking of CO_2 pump laser to the resonance absorption peak of the FIR laser gas via an internal spectrophone is a simple and efficient means of improving the long term FIR power stability. It can typically hold the FIR laser power to within ± 8% for hours without attendance. The fact that the integrated output from the phase sensitive detector can serve as "a preliminary indicator for optimum point" adds
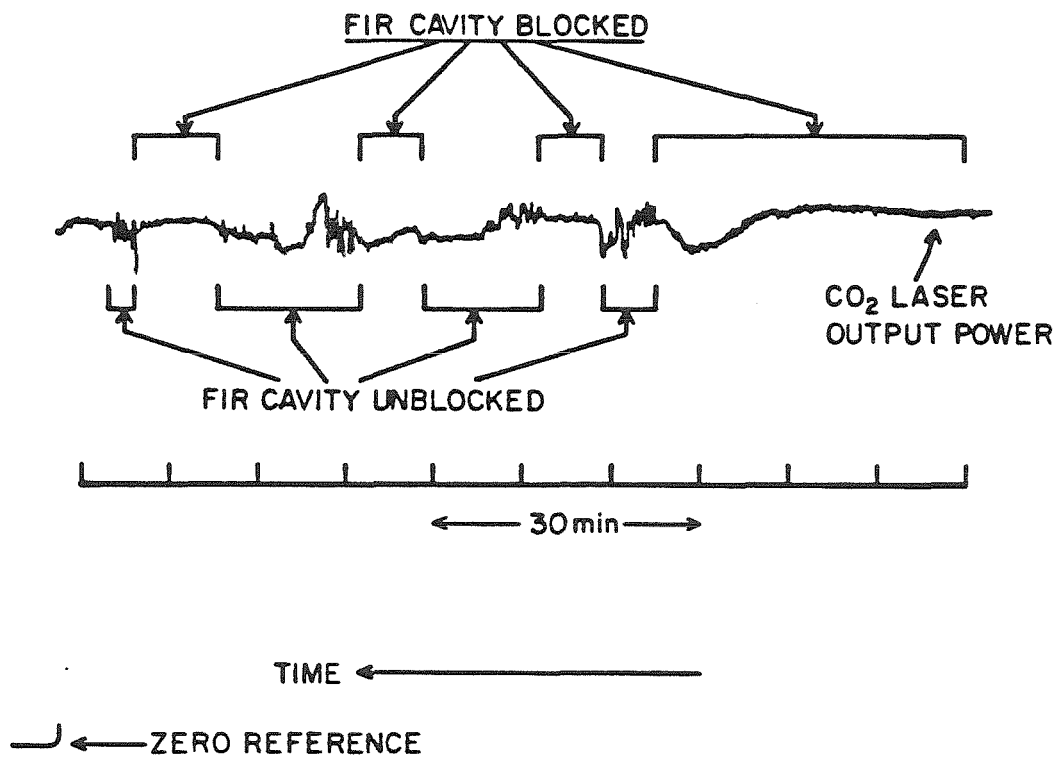
Fig. 3.9 CO_2 laser power fluctuation (cavity pulling effect).

another ingredient to this method as compared to the others.

References for Chapter 3

3.1 See, for example, **Principles of Optics**, M. Born and E. Wolf, 3rd ed., Pergamon Press, 1964, p. 406.

3.2 See, for example, ref. 3.1 , p. 412.

3.3 Springer Series in Optical Science, Vol.2, **Table of Laser Lines in Gases and Vapors**, 2nd ed., Berlin, West Germany, 1978, pp. 79-90.

3.4 P. D. Coleman, "Far-Infrared Laser," sec. 3.3 in **CRC Handbook of Laser Science and Technology**, Vol II, Gas Lasers. M. J. Weber, Editor, CRC Press, Miami, 1982.

3.5 See, for example, **Optics**, E. Hecht and A. Zajac, Addison-Wesley Publishing Co. Menlo Park, California. 1974, pp.311-361.

3.6 See, for example, **An Introduction to Lasers and Masers**, A. E. Siegman, McGraw Hill Book Co., New York. 1971, pp.123-360.

3.7 See, for example, ref. 3.6, p. 123.

3.8 L. B. Kreuzer, "Ultralow gas concentration infrared absorption spectroscopy," *J. Appl. Phys.*, Vol. 42, No. 7, June 1971, pp. 2934-2943.

3.9 L. G. Rosengren, "Optimal optoacoustic detector design," *Appl. Opt.*, Vol.14, No. 7, Aug. 1975, pp. 1960-1970

3.10 M. Kavaya,"Optoacoustic detection employing Stark voltage modulation and Stark polarization modulation," Ph.D Thesis, Electrical Engineering Dept., California Institute of Technology, 1982.

3.11 **Instruction Manual, Far Infrared Laser System Model 122**, Apollo Laser Inc., Los Angeles, California, 1981.

3.12 A. L. S. Smith & S. Moffatt, "Opto-galvanic stabilized CO_2 laser", *Opt. Commu.*, Vol. 30, No. 2, Aug. 1979, pp. 213-218.

3.13 P. W. Smith, "Stabilized, single-frequency output from a long laser cavity," *IEEE. J. Quantum Electron.*, Vol. QE-1, No.3, Nov. 1965, pp. 343-348.

3.14 D. K. Mansfield., "Effects of passive isolation on several optically pumped far-infrared laser lines," *Optics Letts.*, Vol. 6, no. 5, May 1981, pp. 230-232.

Chapter 4. RESONATOR MIRRORS FOR OPTICALLY PUMPED FIR LASERS.

4.1 A General Survey of Various Output Coupling Schemes.

4.1.1 Basic Requirements.

The resonator mirrors for optically pumped FIR lasers must simultaneously possess desired properties at two separated wavelengths, namely, the infrared pump wavelength and the far infrared laser wavelength. Ideally, they should

(i)   Reflect 100% of the radiation over the whole range of the pump laser bands (yet allow the pumped radiation to enter the cavity through one mirror, the input coupler)

(ii)   Partially transmit a specified fraction (5% to 40%) of the radiation at the FIR laser wavelength through one mirror, the output coupler

(iii)   The absorption loss at both wavelengths should be minimum (ideally zero)

In most of the situations, where minimum FIR output beam divergence is desired, the FIR laser EH_{11} mode is preferred, and the coupling should be uniform across the whole aperture of the mirrors. Obviously, it is very difficult to satisfy all these requirements, and much work has been done toward this end. This work is reviewed briefly below.

4.1.2 Various Output Coupling Schemes.

Various mirror types have been used in optically pumped FIR lasers to optimize performance, particularly the FIR output coupling mirror:

(1) Simple hole (SH) couplers [4.1-4.6]

(2) Metal dielectric hole (MDH) couplers [4.6-4.7]

(3) Metal mesh (MM) couplers [4.8-4.9]

(4) Hybrid metal mesh dielectric (MMD) couplers [4.10-4.13]

(5) Hybrid capacitive mesh hole (CMH) couplers [4.13]

(6) Dielectric-coated etalon (DCE) couplers [4.7-4.14]

(7) Variable interferometric couplers [4.15-4.19]

A brief description of the structure, characteristics, advantages and disadvantages of each of them is given in the following section, and summarized in Fig. 4.1.

4.1.3 A General Survey.

(1) Simple hole (SH) couplers.[4.1-4.6]

Simple hole couplers were used in almost all the early versions of optically pumped FIR lasers [4.1-4.3]. They are rugged, relatively simple and inexpensive to fabricate. They can be operated over a very broad spectral range with very low FIR loss. Their major disadvantage lies in the fact that the coupling hole size is the only independent parameter that controls the transmittance/reflectance of both the pump and the FIR laser beams. The laser rarely operates in the EH_{11} mode if the coupling hole is larger than a small fraction of the mode diameter. FIR output from the hole is highly divergent because of its oscillation in combination of higher order EH_{mn} modes. In addition, the pump laser escapes through the FIR output coupling hole.

(2) Metal dielectric hole (MDH) couplers.[4.6,4.7]

MDH coupling is an improved version of SH coupling in the sense that the simple hole is replaced by a substrate with a multilayer dielectric coating for high IR pump reflection. FIR absorption loss can be minimized by proper choice of substrate material (high purity silicon, for instance) and coating material (germanium and zinc sulphide, for instance). FIR transmittance is essentially controlled by the size of this central non-metallic "hole". Because of the Fresnel reflection at the substrate, this "hole" can be relatively large compared to case
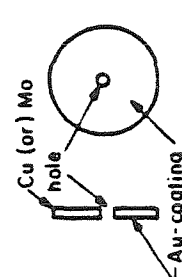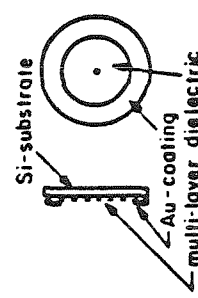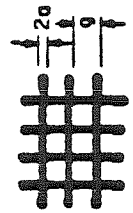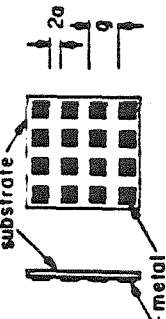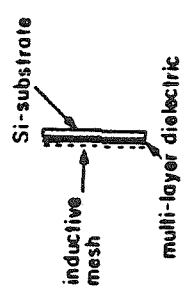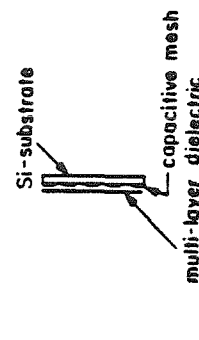
OUTPUT COUPLING SCHEME	IR REFLECTANCE	FIR TRANSMITTANCE	FABRICATION	REF.
(1) Simple Hole (SH)	high	non-uniform	simple comercially available (inexpensive)	[1-6]
(2) Metal Dielectric Hole (MDH)	very high	non-uniform to some extent	fair	[6,7]
(3) Metal Mesh (MM)				
(a) Inductive	very low	uniform	comercially available (inexpensive)	[8,20]
(b) Capacitive	low	uniform	fair	[9,20]
(4) Hybrid Metal Mesh Dielectric				
(a) Version #1	high	uniform	fairly complicated	[10,11,12]
(b) Version #2	high	uniform	fairly complicated	[12]

Cu (or) Mo
hole
Au-coating

Si-substrate
Au-coating
multi-layer dielectric

2a
g

2a
g
substrate
metal

Si-substrate
inductive mesh
multi-layer dielectric

Si-substrate
capacitive mesh
multi-layer dielectric

Fig. 4.1 A general survey of various output coupling schemes.
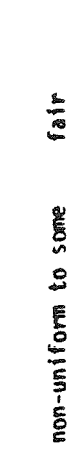
(5) Hybrid Capacitive Mesh Hole — high — non-uniform to some extent — fair — [13]

(6) Dielectric-coated Etalon — high — uniform typically over-coupled — fair, comercially available relatively expensive — [7,14]

(7) Variable Interferometric Coupler

(a) Michelson Type — medium — uniform optimal coupling — simple — [15,16]

(b) Fabry-Perot Type

(i) Double-Mesh — medium — uniform optimal coupling — simple — [17]

(ii) Double-Si Etalon — lo — uniform optimal coupling — fair — [18,19]

Labels on diagrams: substrate, capacitive mesh, Au-coating, 2a, g, Si-etalon, multi-layer dielectric, output window, mesh beam splitter, movable mirror, mesh, Si-etalon

Fig. 4.1 (continued)   A general survey of various output coupling schemes.

(1). The FIR laser mode structure is still coupled to the size of the hole as in case (1).

(3) Metal mesh (MM) couplers.[4.8,4.9]

A metal mesh structure can be either inductive or capacitive [4.20]. Wood, et al. [4.8] used a free-standing metal mesh for both input and output coupling in their metallic waveguide laser. A well- collimated FIR output beam with a half-angle divergence less than .03 radian was achieved, and the observed intensity patterns corresponding to TE_{01} and TE_{02} metallic waveguide modes [4.21]. The characteristics of a capacitive mesh structure coated on a z-cut crystal quartz substrate have been investigated by Wolfe, et al. [4.9]. Although the transmission of a metal mesh coupler at any particular FIR wavelength can be controlled by proper choice of the grid period (g) and grid width (2a) , the IR reflectance can not be controlled independently. The IR wavelength is typically in the diffraction region $(\lambda < q)$, and the reported 65% specular reflection [4.9] is relatively poor compared to other schemes.

(4) Hybrid metal mesh dielectric (MMD) couplers.[4.10-4.13]

In the MMD couplers, first reported by Danielewicz, et al. [4.10], the specified FIR transmittance is controlled by a proper choice of the metal mesh parameters (grid period g and grid width 2a), while high IR reflectance is achieved by a multi-layer dielectric coating. Two variations of MMD geometry have been investigated [4.12]. The original version [4.10], fabricated in the order: substrate, metal mesh, multi-layer dielectric IR reflector (see Table 4.1) has the disadvantage that the IR reflector is in the interior of the FIR cavity and may cause significant FIR absorption. A later version [4.12], fabricated in the order: substrate, IR reflector, metal mesh, tends to reduce FIR loss by placing the IR reflector outside the FIR cavity. Diffraction of the IR pump wavelength by the

metal mesh, however, may result in larger IR loss relative to the original version. In both cases, the output coupling is uniform over the mirror, and laser oscillation in the lowest loss EH_{11} dielectric waveguide mode [4.22] have been identified. Each MMD coupler can be designed for specified reflectance at relatively narrow band around any particular FIR wavelength. The complicated fabrication procedure is the major factor that has precluded their widespread use; these mirrors are not commercially available.

(5) Hybrid capacitive mesh hole (CMH) couplers.[4.13]

The CMH coupler described by Weitz, et al. [4.13], is based on the same idea as the MDH coupler except that the multi-layer dielectric is replaced by a capacitive mesh structure. It is a result of the tradeoff among uniform output coupling property, IR reflectance and complexity of fabrication. It is particularly useful for short FIR wavelength (for instance, CH_3OH 70 μm line) where the FIR absorption loss due to IR-reflecting multilayer dielectric becomes more pronounced.

(6) Dielectric-coated etalon (DCE) couplers.[4.7,4.14]

DCE couplers fabricated from high purity single crystal silicon with multilayer dielectric coatings on one side for high IR reflectance, were first described by Hodges, et al. [4.7], and investigated by Durschlag, et al. [4.14]. The major disadvantage of this single-element etalon is that the maximum FIR reflectance achievable (70%), overcouples the FIR laser radiation for most transitions.

(7) Variable interferometric couplers.[4.15-4.19]

Variable interferometric couplers with a Michelson configuration [4.15,4.16] and a Fabry-Perot configuration [4.17-4.19] have been investigated. The advantage of having variable rather than fixed output coupling is obvious. For the

Michelson configuration, the FIR transmittance can be varied from zero to a maximum value of 4RT where R and T are the reflectance and transmittance of the beam splitter respectively. By proper choice of beam splitter such that 4RT exceeds the optimum transmittance, one can achieve the optimal coupling by simple tuning [4.15]. Ideally the beam splitter should be transparent to IR pump radiation and reflects approximately 50% at FIR wavelength (so that $4RT \approx 1$). Typically metal meshes are used as beam splitters due to their low absorption loss at both pump and FIR wavelengths. The transmittance at the pump wavelength is, however, far from ideal and in some cases appropriate meshes for optimal output coupling may not be readily available [4.16].

In the Fabry-Perot configuration, double wire mesh reflectors [4.17], coated double germanium etalons [4.18], uncoated double silicon etalons [19], and uncoated triple silicon etalons [4.19] have been reported. With a triple silicon etalon output coupler, Julien and Lourtioz [4.19] were able to achieve FIR reflectance of approximately 90 % over a reasonably wide band (60 cm^{-1} to 200 cm^{-1}). Evenson, et al.[4.23] also reported a triple-plate etalon consisting of two uncoated silicon flats and one uncoated crystal quartz flat separated at fixed distance. Reflectance of approximately 90% was achieved at 71 μm wavelength.

Ideally, the output coupling is uniform over the whole waveguide aperture. In practice, both the uniformity of the output coupling and loss may depend on the alignment of the surfaces. With the exception of a special design incorporating extra optical element to ensure that the fraction of IR pump radiation that "leaks" out of the cavity is properly reflected back [4.19], the IR loss is expected to be significant in these couplers. No estimation of IR loss has been reported in the literature, however.

4.2 Choice of Output Coupling Schemes.

Although it would be ideal if one could simply point out which output coupling scheme is the "best", it should not be surprising that there exist no universal criteria for selecting the "best" output coupler in a general sense. Depending on the specific experimental condition and requirements, and taking into account various other factors such as fabrication cost, availability, durability and ease of operation, each scheme is in fact unique in one way or another.

For this parametric study of optically pumped FIR lasers, a uniform output coupling coefficient independent of the size of waveguide was crucial. This was necessary so that the effects exclusively due to variation of waveguide radius could be investigated while keeping the FIR laser operating only in a fixed mode (EH_{11}), independent of waveguide size. A multi-layer dielectric coated silicon etalon configuration was chosen for our experiment for the following reasons:

(1)   Fabrication was commercially available.

(2)   It is reasonably easy to align and adjust.

(3)   Although the characteristics of coated silicon etalons had been investigated by Durschlag, et al. [4.14], no evaluation of their performance as uniform output couplers in FIR lasers has been reported.

The design, characteristics and performance of multi-layer dielectric coated silicon etalon will be treated in the next section.

4.3 Multi-layer Dielectric-Coated Silicon Etalon Output Couplers

To study the feasibility of using multi-layer dielectric coated silicon etalons as uniform output couplers for FIR lasers, an estimation of the FIR properties of uncoated silicon, based on the data given in table 4.1 and 4.2 , is carried out as follows: The single surface reflectance is given by the Fresnel equations [4.26]

Table 4.1

Index of Refraction of Pure (resistivity>10 ohm-cm) Silicon

at Various FIR Wavelengths and Temperatures [2.24, 2.25].

λ＼＼T	1.5°K	300°K
	n(λ, T)	
70 μm	3.385	3.419
118 μm	3.384	3.418
496 μm	3.381	3.415

The estimated error on n given in the table is ±0.001

$(\Delta n/\Delta \lambda) \simeq - 8 \times 10^{-6}$ /μm.

$(\Delta n/\Delta T) \simeq 1.13 \times 10^{-4}$ / °K

$\left.\begin{array}{c} \\ \\ \end{array}\right\}$ for λ=118μm, at T≃ 300°K

Table 4.2

Absorption coefficient of Pure Silicon (resistivity > 10 Ωcm)
at Various FIR Wavelengths and Temperatures [4.25, 4.26].

λ \ T	1.5°K	300°K
	$\alpha(\lambda, T)$ in neper/ cm	
70 μm	0.5	1.1
118 μm	0.3	0.8
496 μm	0.1	0.3

The estimated error of α given in the table is
±0.2 neper/cm

$(\Delta\alpha/\Delta T) \simeq 1.6 \times 10^{-3}$ neper/cm/°K   for $\lambda \approx 118$ μm, at $T \approx 300$°K

$$R = \frac{(n-1)^2 + k^2}{(n+1)^2 + K^2} \approx \frac{(n-1)^2}{(n+1)^2} \approx \frac{(2.4)^2}{(4.4)^2} \approx 30\%$$

The transmittance, reflectance and loss at resonance (i.e. at the transmission peak of the etalon) are given by

$$T_{res} = T_{max} = \frac{(1-R_1)^2 e^{(-at)}}{[1-R_1 e^{(-at)}]^2}$$

66% for t = 1 mm

93% for t = 0.5 mm

where a is the absorption coefficient and t is the thickness.

$$R_{res} = R_1 \frac{[1-e^{(-at)}]^2}{[1-R_1 e^{(-at)}]^2}$$

0.37%   for t = 1 mm

0.1%   for t = 0.5mm

Loss = A = 1-T-R

14%   for t = 1 mm

7%   for t = o.5 mm

At anti-resonance (i.e. transmission minimum of the etalon) these quantities are:

$$T_{ar} = T_{min} = \frac{(1-R_1)^2 e^{(-at)}}{[1+R_1 e^{(-at)}]^2}$$

27.7% for t = 1 mm

28.3% for t = 0.5 mm

$$R_{er} = R_1 \frac{[1+e^{(-at)}]^2}{[1+R_1 e^{(-at)}]^2}$$

67.9% for t = 1 mm

69.5% for t= 0.5%

$$\text{Loss} = A = 1\text{-}T\text{-}R \qquad \begin{array}{l} 4.4\% \text{ for } t = 1 \text{ mm} \\[6pt] 2.8\% \text{ for } t= 0.5 \text{ mm} \end{array}$$

In Fig. 4.2, the transmittance, reflectance, and loss of an etalon are plotted against the phase shift per pass ($2\pi nt/\lambda$), for silicon wafers of three different thicknesses.

Since the optimum output coupling coefficient for most of the FIR laser transitions lies in the range of 5% to 30%, it is obvious from the simple analysis given above, that the thickness of the silicon etalon has to be in the vicinity of anti-resonance at the operating FIR wavelength (i.e. $t \approx (2p+1)\lambda/4n$,where n is the index of refraction and p, an integer). The simple analysis also reveals that for a silicon wafer with thickness t $\approx$ 1 mm, the allowed uncertainty (variation) in thickness is 1 μm, so that the reflectance will lie in the range of $R_{max} \pm 2\%$. From the known linear expansion coefficient of Si ($\approx 4 \times 10^{-6}/$ °K at room temperature [4.29]) it follows that the allowed temperature variation is $\approx$400 °K.

Fifteen pieces of two inch diameter silicon wafers (an assorted mixture of single-side polished and double-side polished pieces) were obtained from various sources, with resistivities ranging from 20 ohm-cm to 2000 ohm-cm and thicknesses ranging from 0.3 mm to 1.2 mm . These pieces were first ultrasonically cleaned in TCE (Trichloro-ethylene), acetone and methanol, followed by etching in 20% HF, then in RCA solution ($H_2O_2+NH_4OH+H_2O$ in a ratio of 1:1:5) and a final etch in 6% HF. Their FIR properties (reflectance, transmittance and
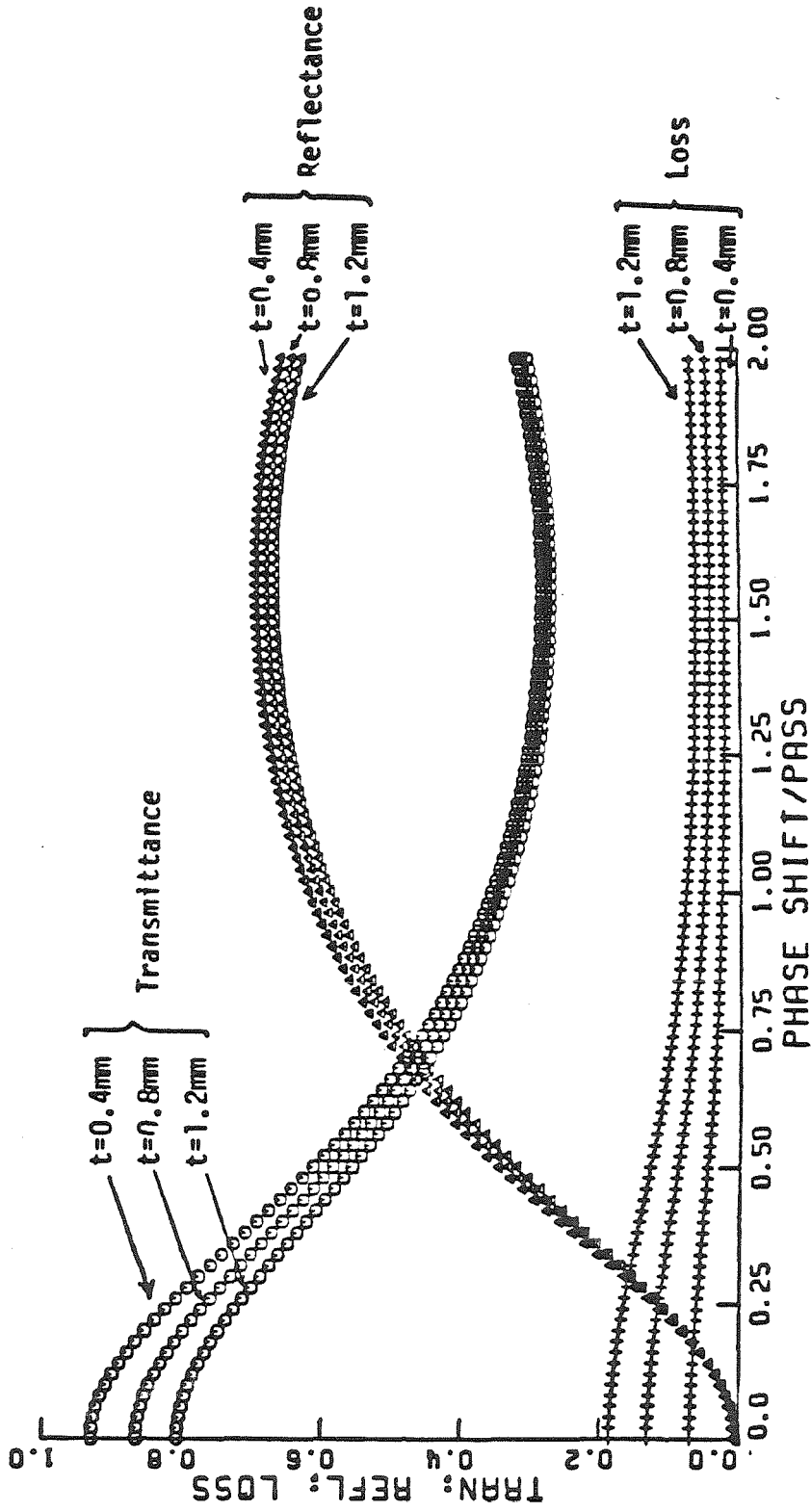
Fig. 4.2 Optical characteristics of silicon etalon at FIR region for three different wafer thicknesses.

loss at 118 μm) were then measured using a CH$_3$OH FIR laser as described below. The output power I of the CH$_3$OH 118 μm laser was first measured directly by a Scientech calorimeter D_1 as illustrated in Fig. 4.3 (a). The sample mounted on a horizontal rotating mount was then inserted into the beam and the transmitted intensity I(0) was measured again by detector D_1 for perpendicular incidence as shown in Fig. 4.3 (b). The transmittance I(0)/ I turned out to be reproducible to within ± 3%. A second identical calorimeter D_2 located at the other side of the sample, at equi-distant but slightly offset to avoid input beam interruption, was used to measure the reflected beam at near normal incidence (approximately 12 degrees as limited by the geometry of the detector) as shown in Fig. 4.3 (c). Fractional loss and reflectance at normal incidence were then estimated by the expression given in the caption of Fig. 4.3. The results of some representative samples are given in Table 4.3. Because the parameters involved (resistivity, thickness, surface flatness) were not well characterized, it is very difficult to correlate the measured FIR properties with the parameters cited above.

Ten samples were selected for relatively high FIR reflectance and low loss, and sent out for IR reflective multi-layer dielectric coating (fabricated by Laser Power Optics Inc.), based on the prescription given by Durschlag, et al. [4.14] and Danielecwicz [4.28]. The FIR properties of the coated silicon wafers were again measured by the same procedure (see Fig. 4.3) and the results for some of the selected samples before and after the coating process are compared in Table 4.4. It is interesting to note that although the thickness of the coating is fairly small compared to FIR wavelength (thickness $\approx$ 10 μm, λ = 118 μm [4.28]), it did significantly alter the FIR properties. For sample A, for instance, FIR transmittance changed from $\approx$ 35% to $\approx$ 85%. The effect of coating, although not totally unexpected, considering the high index of refraction of coating
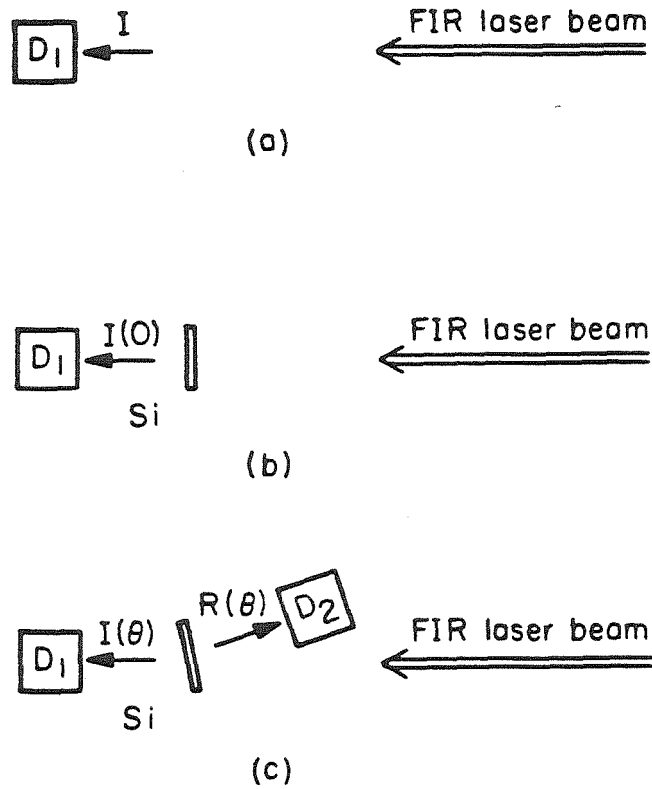
Fig. 4.3 Schematic diagram for measurement of FIR

properties of Si wafers.

Transmittance = T(0) = I(0)/I

Fractional Loss = A(0) ≃ [I-I(θ)-R(θ)]/I

Reflectance = R(0) ≃ [I-I(0)-A(0)]/I

Table 4.3

FIR Properties (at 118 μm) of Some Representative Silicon Wafers.

Sample	Thickness (in mm)	Resistivity (in ohm-cm)	Transmittance	Reflectance	Loss
A	0.524	2000	35%	60%	5%
B	0.322	100	50%	50%	0%
C	0.328	100	45%	55%	0%
D	0.986	20	37%	53%	10%
E	0.886	20	45%	45%	10%

Table 4.4

Comparison of FIR Properties (at 118 µm) of Some Representative Silicon
Wafers Before and After Multi-layer Dielectric Coating.

Sample	Transmittance		Reflectance		Loss	
	before coating	after coating	before coating	after coating	before coating	after coating
A	35%	85%	60%	10%	5%	5%
B	50%	54%	50%	41%	0%	5%
C	45%	55%	55%	40%	0%	5%
D	37%	50%	53%	20%	10%	30%
E	45%	40%	45%	45%	10%	15%

materials (4.0 for Ge and 2.17 for Zns), is however contrary to Durschlag's result [4.14]. The maximum FIR reflectance obtained from our coated samples is $\approx$ 52%, and turned out to be somewhat below the threshold value for our FIR laser system with pump power of the order of 9 watts.

Various combinations of coated silicon wafers and uncoated silicon wafers or free standing meshes, with and without mylar ring spacers in between (see Fig.4.4), were tested for high FIR reflectance. Significant improvement in reflectance was achieved in two particular combinations (see Fig. 4.4(b) and Fig. 4.4(c)) whose FIR properties are given in table 4.5. These two particular combinations (Si-SS-Coated Si and M-coated Si) were used as output couplers for our FIR laser throughout the experimental parametric study described in the next chapter.
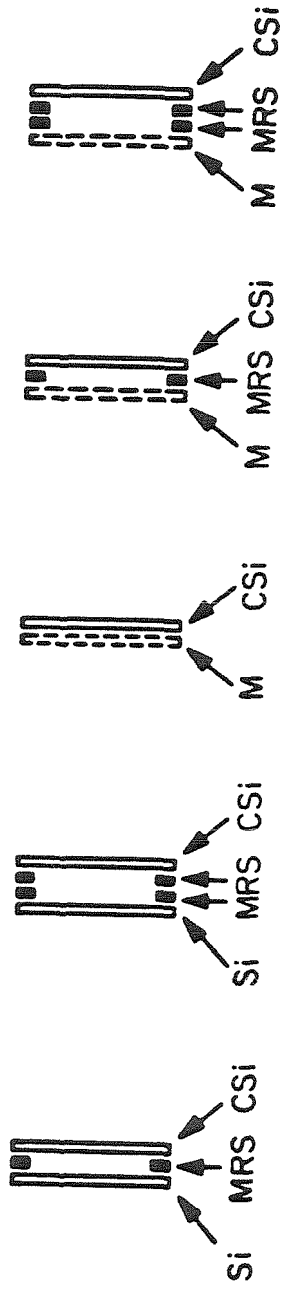
Fig. 4.4 Various combinations of coated silicon wafers and uncoated silicon wafers or free standing meshes with or without mylar ring spacer/spacers in between.
Si : uncoated silicon wafer;   CSi : coated silicon wafer;
MRS : mylar ring spacer;   M : metal mesh.

Table 4.5

FIR Properties (at 118 μm) of Two Uniform Output Couplers.

Output Couplers Type	Transmittance	Reflectance	Loss
Si-SS-Coated Si see Fig. 4.3 (b)	35%	60%	5%
Mesh-Coated Si see Fig. 4.3 (c)	10%	85%	5%

References for Chapter 4

4.1   T.Y. Chang, T.J. Bridges and E.G. Burkhart, "Cw submillimeter laser action in optically pumped methyl fluoride, methyl alcohol and vinyl chloride gases," *Appl. Phys. Lett.*, Vol. 17, No. 6, Sept. 1970,pp. 249-251.

4.2   D.T. Hodges and T.S. Hartwick, "Waveguide laser for the far-infrared pumped by a CO laser," *Appl. Phys. Lett.*, Vol. 23, Sept. 1973,pp. 252-253.

4.3   H.R. Fetterman, H.R. Schlossberg and C.D. Parker, "Cw submillimeter laser generation in optically pumped Stark tuned NH_3," *Appl. Phys. Lett.*, Vol. 23, No. 12, Dec. 1973,pp. 684-686.

4.4   L.D. Fesenko and S.F. Dyubko, "Optimization of the parameters of optically pumped submillimeter lasers," *Sov. J. of Quantum Electron.*, Vol. 6, No. 7, July 1976, pp. 839-843.

4.5   A Tanaka, et al.,"Cw efficient optically pumped far-infrared waveguide NH_3 lasers," *Opt. Commun.*, Vol. 22, No. 1, July 1977,pp. 17-21.

4.6   D.T. Hodges, F.B. Foote and R.D. Reel, "High power operation and scaling behavior of cw optically pumped FIR waveguide lasers," *IEEE, J. Quantum Electron.*, Vol. QE-13, No. 6, June 1977, pp. 491-494.

4.7   D.T. Hodges, F.B. Foote and R.D. Reel, "Efficient high power operation of the cw far infrared waveguide laser," *Appl. Phys. Lett.*, Vol. 29, No. 10, Nov. 1976, pp. 662-664.

4.8   R.A. Wood et al.,"An optically pumped waveguide laser with mesh reflectors," *Opt. Commun.*, Vol. 14, No. 3, July 1975,pp. 301-303.

4.9   S.W. Wolfe, et al.,"Modulated submillimeter laser interferometer system for plasma density measurements," *Appl. Opt.*, Vol. 15, No. 11, Nov. 1976,pp. 2645-2648.

4.10 E. J. Danielewicz, T.K. Plant and T.A. Detemple, "Hybrid output mirror for optically pumped far-infrared lasers," *Opt. Commun.*, Vol.13, No. 4, Apr. 1975,pp. 366-369.

4.11 E.J. Danielewicz and P.D. Coleman, "Hybrid metal mesh dielectric mirror for optically pumped far-infrared lasers," *Appl. Opt.*, Vol. 15, No. 3, Mar. 1976,pp. 761-767.

4.12 M.R. Schubert, M.S. Durschlag and T.A. DeTemple, "Diffraction limited cw optically pumped lasers," *IEEE J. Quantum Electron.*, Vol. QE-13, No. 6, June 1977,pp.455-459.

4.13 D.A. Weitz, W.J. Skocpol and M. Tinkham, "Capacitive mesh output couplers for optically pumped far-infrared lasers," *Opt. Lett.*, Vol. 3, No. 1, July 1978, pp. 13-15.

4.14 M.S. Durschlag, S.J. Petuchowski and T.A. DeTemple, "Infrared-far-infrared dichroic dielectric mirrors," *Infrared Physics*, Vol. 20, 1980, pp. 309-312.

4.15 S.R. Kumar, R.J. Tansey and J. Waldman, "Optically pumped sub-millimeter wave laser with Michelson interferometric output coupling," *IEEE J. Quantum Electron.*, Vol. QE-13, No.1,January 1977,pp.30-33.

4.16 G. Duxbury and H. Herman, "CW optically pumped far-infrared waveguide laser with variable output Michelson coupler," *J. Phys. E : Sci. Instrum.*, Vol. 11, 1978, pp. 419-450.

4.17 C.O. Weiss, "Optically pumped FIR laser with variable Fabry-Perot output coupler," *Appl. Phys.*, Vol. 13, 1977, pp. 383-385.

4.18 F. Brown, "High power optically pumped far-infrared lasers," *Infrared Phys.*, Vol. 16, 1976, pp. 171-174.

4.19 F. Julien and J-M. Lourtioz, "Silicon Fabry-Perot interferometer as an optical FIR component: application to variable couplers with uniform transmission of FIR optically pumped lasers," *Intern. J. of Infrared and Millimeter Waves*, Vol. 1, No. 2, 1980, pp. 175-194.

4.20 R. Ulrich, "Far-infrared properties of metallic mesh and its complementary structure," *Infrared Phys.*, Vol. 7, 1967, pp. 37-55.

4.21 See, for example, **Fields and Waves in Communication Electronics** by S. Ramo, J.R. Whinnery and T. Van Duzer. John Wiley & Sons, 1965, ,Chapter 8.

4.22 E.A.J. Marcatili and R.A. Schmeltzer, "Hollow metallic and dielectric waveguide for long distance optical transmission and lasers," *Bell System Tech. J.*, Vol. 43, 1964, pp. 1783-1809.

4.23 K.M. Evenson, et al.,"Optically pumped FIR lasers: frequency and power measurements and laser magnetic resonant spectroscopy," *IEEE J. Quantum Electron.*, Vol. QE-13, No. 6, June 1977, pp. 442-444.

4.24 E. V. Loewenstein, et al.," Optical constants for far-infrared materials, 2 : crystalline solids," *Appl. Optics*, Vol. 12, No. 12, Feb. 1973, pp. 398-406.

4.25 W. F. Passchier, et al.,"A new method for determination of complex refractive index spectral of transparent solids in the far-infrared spectral region: Results of pure silicon and crystal quatrz," *J. Phys. D, Appl. Phys*, Vol. 10, 1977, pp. 509-517.

4.26 See, for example, **Principle of Optics**, M. Born and E. Wolf, 3rd ed., Pergamon Press., Oxford, England. 1964, page 620.

4.27 **The Infrared Handbook**, Ed. W.L. Wolfe and G.J. Zissis, Office of Naval Research, Washington D. C. 1978.

4.28 E. J. Danielewicz, private conversation.

CHAPTER 5. EXPERIMENTAL PARAMETERIC STUDIES.

5.1 Introduction.

As we have seen in Chapter 2 output power of an optically pumped FIR laser depends on various factors such as :

* IR pump power

* pressure of the active gas

* waveguide diameter

* FIR cavity length

* output coupling coefficient.

Although hundreds of papers on optically pumped FIR lasers exist in the literature, only a few of them deal with experimental parametric studies. This lack of data is undoubtedly due to the difficulties associated with the problems of stability and reproducibility. Systematic parametric studies are extremely important not only for optimization of design parameters but also for a deeper understanding of the physics involved.

Yamanaka and Yoshinaga [5.1] gave some general power law relationships between FIR output power, optimum pressure, waveguide diameter, FIR cavity length and pump power, together with some experimental results for the NH_3 copper waveguide laser at 81.5 μm. Neither the assumptions involved in the theory nor its derivation was discussed in their paper.

The first systematic and fairly extensive experimental parametric study was reported by Fesenko and Dyubko [5.2] in 1976. Using a conventional FIR laser cavity 1.2 meter long with mirrors of 10 cm diameter and 0.9 meter radius of curvature, the dependence of FIR output power on pump power, active gas pressure, resonator length and diameter of exit aperture for various FIR laser transitions in CH_3OH, CH_3F, CH_3I and $HCOOH$ was investigated. Hole couplers (4mm

hole) were used for both input and output coupling.

Tanaka *et al* [5.3] investigated the relationship between FIR output power, IR pump power, active gas pressure and waveguide diameter for various FIR laser transitions in NH_3, CH_3OH and CH_3CN, using hole output couplers and a copper waveguide, as well as an open (TEM_{00}) laser cavity. Experimental curves are given, however, only for NH_3 laser transition at 81.5 μm. As was pointed out in chapter 3, hole coupling is intrinsically non-uniform, with the FIR output transmittance strongly coupled to both IR reflectance and waveguide diameter, so that it is extremely difficult to single out the effects exclusively due to waveguide diameter.

Lourtioz and Adde [5.4] observed the relationship between FIR output power, pump power and active gas pressure for CH_3OH laser at 118 μm, using a 25 mm ID pyrex waveguide with hole coupling mirrors at both ends (2 mm injection hole and 4mm output hole). By varying the pressure of the gas in a separate FIR gas attenuator cell, they were able to vary the pump power continuously. The experimental results agree fairly well with their analysis based on a rate equation model.

Kokubo, *et al.* [5.5] investigated the dependence of FIR output power on pump power, active gas pressure, waveguide diameter and output coupling coefficient for the CH_3F laser transition at 496 μm, using a metalic waveguide and MDH (metal mesh dielectric hybrid) uniform output coupler. Fairly good agreement with theory was reported.

Out of the many important parameters and thousands of FIR laser transitions, we have chosen to investigate the relationship between FIR output power, IR pump power, active gas pressure and waveguide diameter for CH_3OH laser transition at 118 μm for the following reasons :

(1)   The CH_3OH laser transition at 118 μm is one of the strongest cw FIR laser lines known to date.

(2)   Although parametric studies on this particular laser line had been reported, some of the important relationships remain either unexplored or the results inconclusive.

(3)   Dependence of various parameters on waveguide diameter is of particular interest because it may lead to a better understanding of the role of wall-collisional de-excitation processes in the FIR laser transition cycle. Furthermore, the waveguide diameter is obviously one of the most important design parameters in the practical realization of a compact waveguide FIR laser.

The experimental setup and procedures are discussed in section 5.2. In section 5.3, the experimental results are analyzed and compared with those available in the literature.

5.2 Experimental Detail.

The experimental setup used for parametric study is essentially identical to the one schematically illustrated in Fig. 3.5, except that two mounts for NaCl and ZnSe flats respectively are incorporated into the system immediately outside the input window of FIR laser gas chamber. These were used as an IR beam attenuator to vary the pump power and were mounted in such a way that they could be independently and precisely switched into and out of the pump laser beam. Four different pump power levels approximately in the ratio of 1 : 0.91 : 0.58 : 0.53 were available by various combinations of the two beam attenuators. Pump power was measured before and at the end of each run by placing the detector (Scientech Calorimeter Model 360001 and/or Coherent Power Meter Model 201) right inside the FIR cavity. The results were found to agree to within

3%.

Although continuous variation and control of the pump power by varying the CO_2 gas pressure and/or discharge current had been attempted, it turned out to be impractical because of the instability resulting from the nonlinear and hysteresis nature of CO_2 laser power dependence on discharge current and gas pressure.

The variation of the FIR output power with a continuous variation of active gas pressure was recorded by controlling the CH_3OH inlet and outlet valves while keeping all the other variables constant. Typical experimental results are shown in Fig. 5.1. By comparing the two curves for successive runs it is obvious that, although qualitative feature of the curves remain essentially unchanged, both the optimum pressure and particularly the FIR output power for a given pressure vary significantly from run to run. This is probably due to the dynamic nature of the gas pumpout procedure, and the slow time response of the pressure gauge, and the mechanical instability introduced by the process.

An alternative procedure was to leave the system untouched and let it relax to a steady state pressure. The FIR output power is then measured for different values of pump power at that particular steady state pressure by switching the two beam attenuators on and off while keeping all the other parameters constant. By gently manipulating the inlet and/or outlet valves of FIR laser gas chamber, the active gas in the chamber is then allowed to relax to a new steady state pressure before the measurement procedure described above is repeated. This second approach proved to be much more reliable, and the results were reproducible because the system remains in steady state and is not significantly disturbed during the data acquisition process.

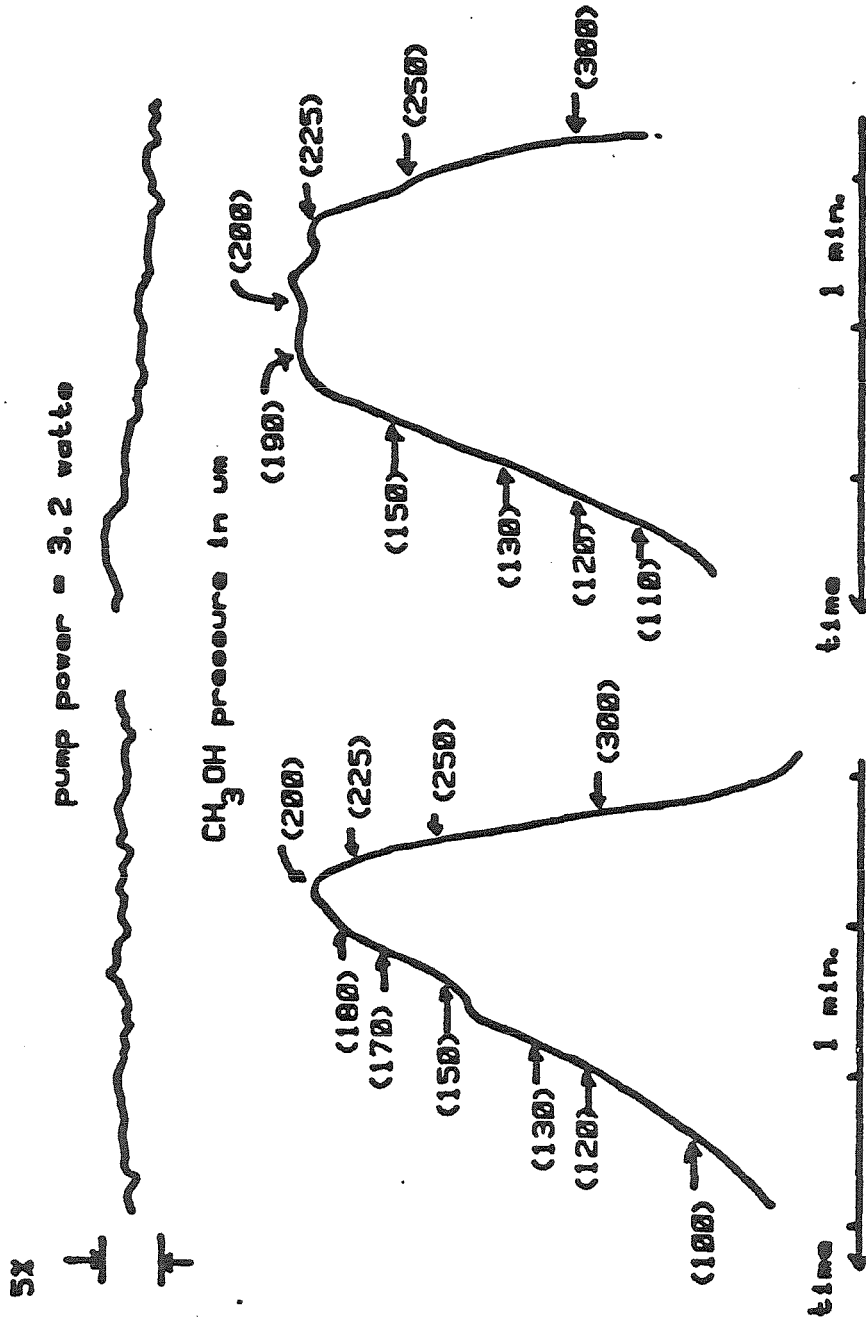Although pyrex tubes with diameter ranging from 6mm to 25 mm were tried,

Fig. 5.1 Dynamic pressure dependence of FIR output power -- experimental results for two successive runs under "identical" conditions. (Values of CH_3OH pressure are shown in the brackets and the monitored CO_2 pumped power is shown on the top)

a strong localized focusing of the pump radiation by the small diameter tubes tended to "burn" the cavity mirrors and the tube wall. As a consequence, data from waveguides with diameter 11 mm were disregarded.

Components and data associated with the FIR laser system are listed in Table 5.1, and the experimental results are discussed in the next section.

5.3 Experimental Results.

Dependence of FIR output power on active gas pressure for four different pump power levels and three different waveguide diameters are summarized in Fig. 5.2 which clearly reveals the following qualitative features :

(1)   For a given waveguide diameter, the optimum pressure increases slowly as the pump power increases.

(2)   For a given pump power, optimum pressure increases significantly as the waveguide diameter decreases.

(3)   Dependence of FIR output power on IR pump power is much stronger in the high pressure region than in the low pressure region.

By carefully analyzing Fig. 5.2, together with similar curves for other waveguide diameters, we were able to deduce several quantitative relationships between some important parameters as explained below.

The dependence of the optimum pressure on waveguide diameter, as illustrated in Fig. 5.3, is consistent with Hodges' result [5.6]. Linear regression gives an excellent fit with correlation coefficients of 0.998 and 0.958 for pump power of 5.6 W and 9.6 W respectively. Similar $1/d$ (d = waveguide diameter) dependence of optimum pressure can also be deduced for CH_3F metallic waveguide laser at 496 um from Kokubo's result [5.5]. This may imply that the vibrational relaxation in CH_3OH laser is essentially diffusion limited, as is the case for the

Table 5.1

Some Components and Parameters Associated With the FIR Laser System.

CO_2 Laser

    gas pressure $\approx$ 30 torr

    discharge current $\approx$ 1.6 mA

    wavelength $\approx$ 9.7 µm $(9P_{36})$

    output power $\approx$ 13 watts

FIR Laser

    input window : uncoated ZnSe flat at Brewster angle

    output window : Z - cut crystalline quartz

    input coupler : 2" diameter copper mirror with 2.5 mm coupling

                 hole at the center

    output coupler : 1000 lines/inch nickel mesh (grid wirth = 0.3

                 milli-inch), mylar ring spacers and coated

                 silicon wafer

                 (R $\approx$ 82%, T $\approx$ 12% at 118 µm ; R $\approx$ 95% at 9.6 µm)

    output clearance aperture : 1" (limited by the output window)

    waveguide : pyrex tubes with inner diameter ranging from 11.5 mm

          to 25 mm

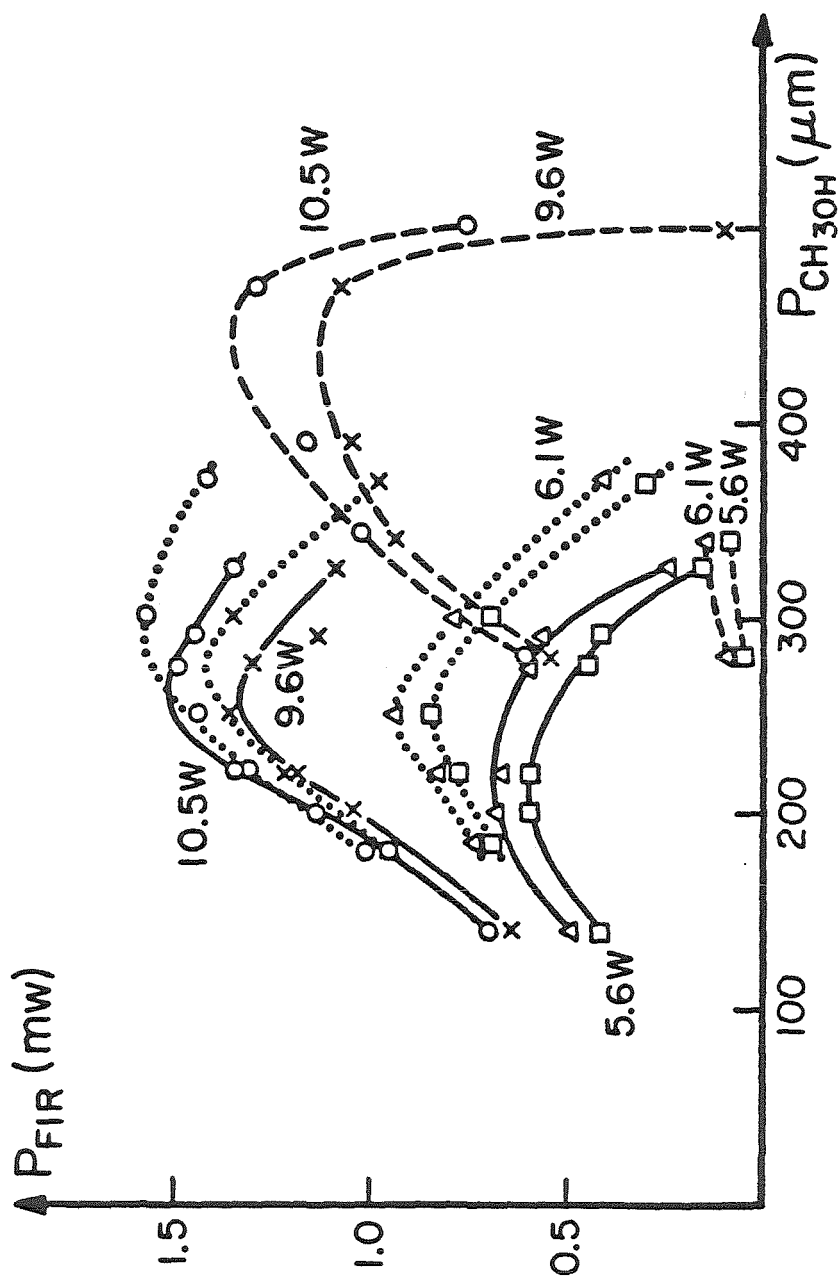Fig. 5.2 FIR output power vs CH_3OH pressure for various waveguide diameters and pump powers. (Solid lines, dashes and dots are used to interpolate between experimental points to distinguish the results for different waveguide diameters.)
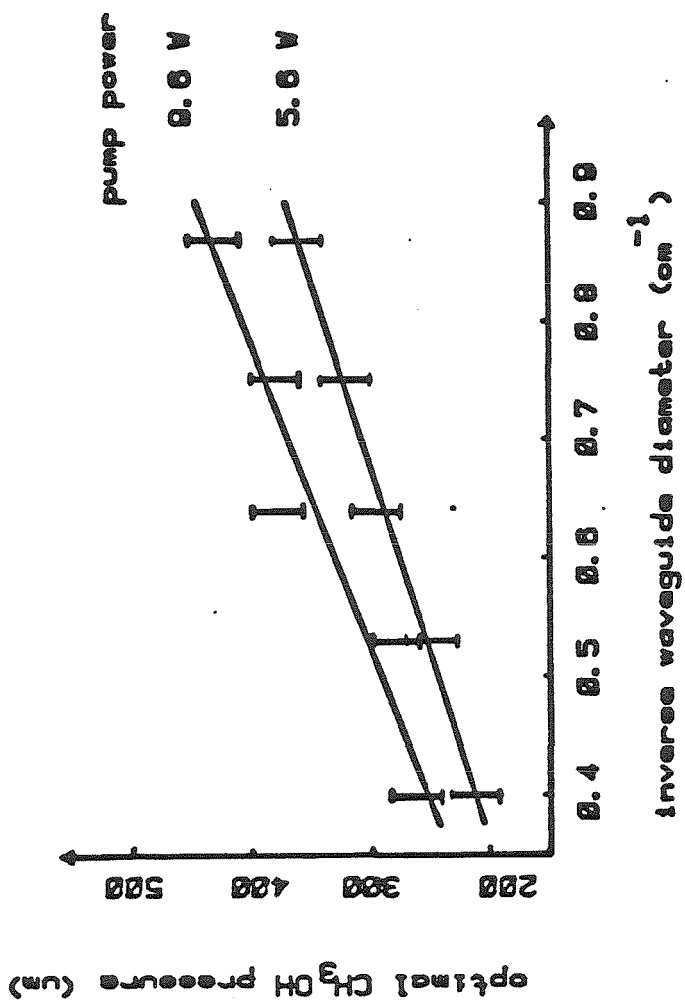
Fig. 5.3 Optimum CH_3OH pressure vs inverse waveguide diameter for two different pump power levels.
(I : experimental data ; Solid lines : linear regression)

CH_3F laser at 496 m, and in contrast with CH_2F_2 laser, whose optimum pressure shows no waveguide diameter dependence [7.7].

The dependence of optimum pressure on pump power for constant waveguide diameter also turns out to be linear (Fig. 5.4) with correlation coefficients of linear regression $\gtrsim 0.98$. This is consistent with the results deduced from the work reported by Lourtioz and Adde [5.4]. Our results further reveal that the slopes tend to be steeper for smaller waveguide diameter, although the dependence is mild. It is interesting to note that although both the CH_3F laser at 496 μm and the CH_3OH laser at 118 um show the same 1/d dependence on waveguide diameter, the dependence of optimum pressure on pump power for CH_3F metallic waveguide laser at 496 μm was shown (both theoretically and experimentally) to be far from linear by DeTemple and Danielewicz [5.8].

Another interesting linear relationship turns out to be the dependence of FIR output power (at optimum pressure) on pump power for various waveguide diameters (Fig. 5.5). The correlation coefficients for the fit are better than 0.995 in all cases. Similar linear dependence can be deduced from the work of Lourtioz and Adde [5.4] for the same laser transition for 25 mm ID pyrex waveguide with a 4 mm hole output coupler. Roser and Schultz [5.9] however, reported a nonlinear dependence [optimum FIR output power (pump power)] for the same laser transition, using a 14mm ID brass waveguide with a 1.5 mm diameter hole coupling. Neither experimental curves nor error estimates were given in their report. Since the range of pump power covered in their work ($P_{pump} \approx 1.5$ W) is much narrower than ours, ($P_{pump} \approx 5.5$ W to 10.5 W), we are convinced that the linear model represents a better approximation in general. The 1.85 power dependence, if applicable, is certainly restricted to only a very narrow region in the vicinity of threshold pump power.
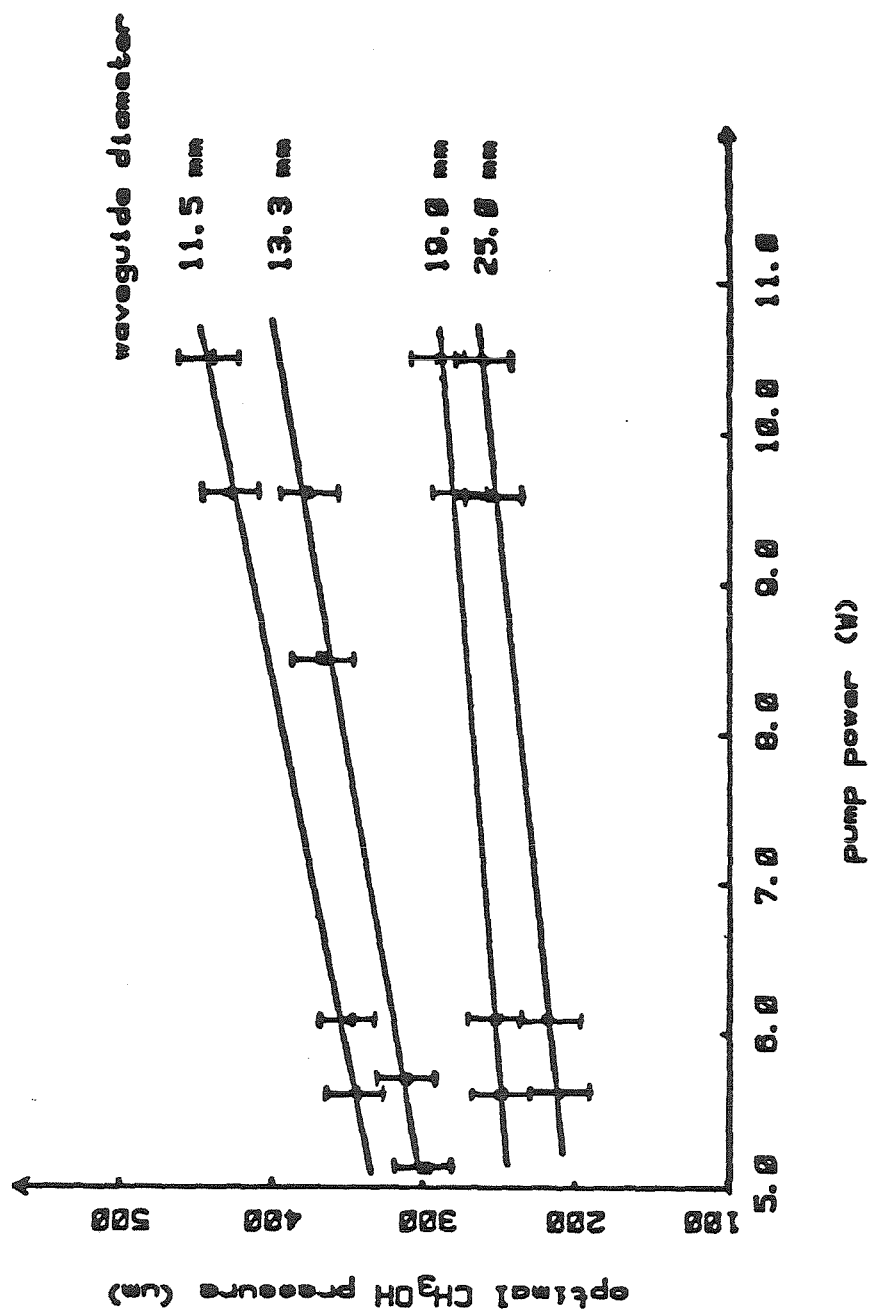
Fig. 5.4. Optimum CH₃OH pressure vs pump power for various waveguide diameters.
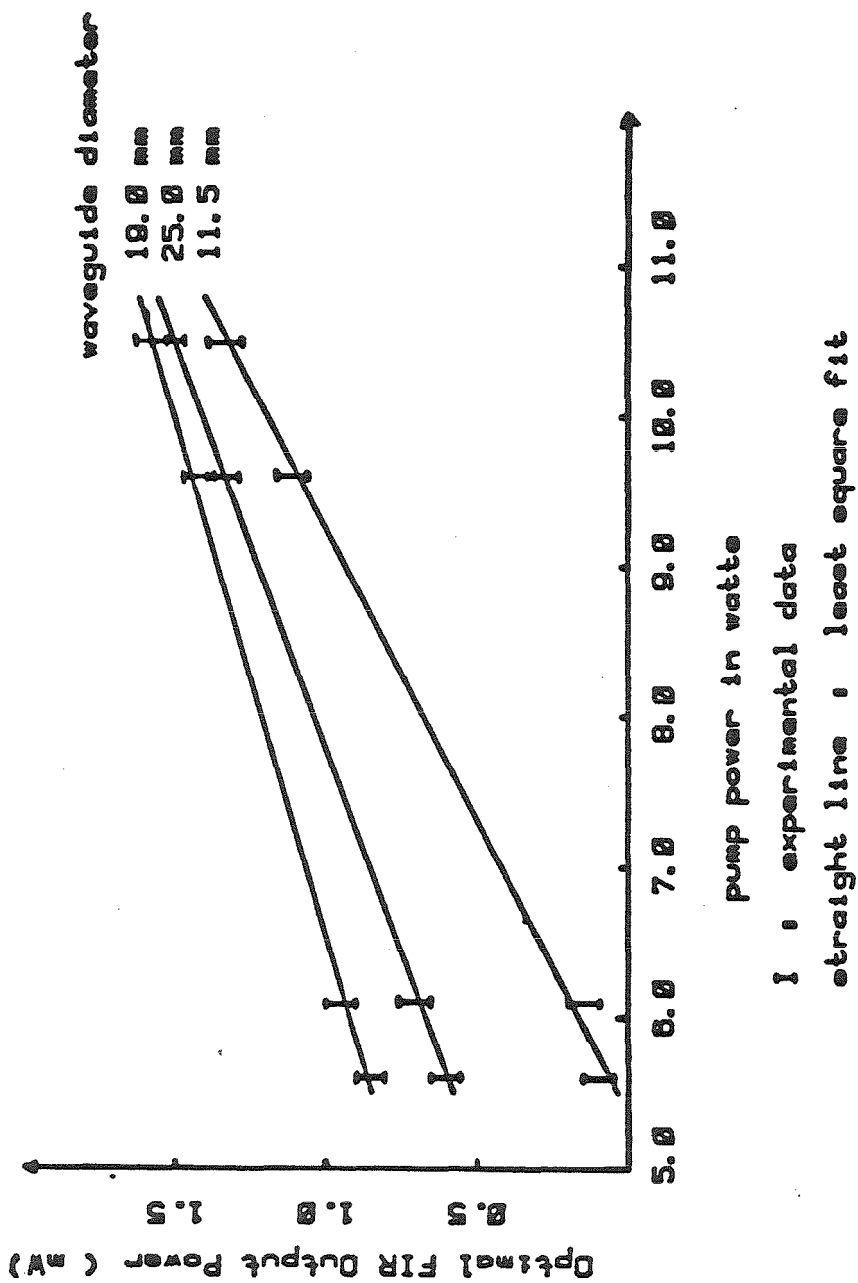(I : experimental data ;   solid lines : linear regression)

Fig. 5.5 FIR output power (at optimum pressure) vs pump power for various waveguide
diameters. (I : experimental data ; solid lines : linear regression)

The theoretical result of Kokubo, et al. [5.4] also shows a linear (or approximately linear) dependence of FIR output power on pump power at optimum pressure and optimum output coupling coefficient for CH_3F metallic waveguide laser at 496 μm.

In Fig. 5.6, FIR output power at optimum pressure is plotted against waveguide diameter for four different pump power levels. A similar result was reported by Hodges [5.6] for the same laser transition with pyrex tubes at 15 W constant pump power. The following interesting points should be noted from Fig. 5.6 :

(1)   The optimum waveguide diameter is almost independent of pump power, for pump power level in the range of 5 to 11 W. It may, however, depend on the output mirror transmittance, and our results for R$\approx$ 82% and T$\approx$ 12% show that the optimum waveguide diameter is around 20 cm.

(2)   Small waveguide diameter is in general unfavorable for low pump power. This can be understood qualitatively from the fact that at relatively low pump powers, the excitation rate is slow enough so that fast vibrational relaxation with the aid of wall collision is not particularly important, and the 1/d pump loss [10] dominates the 1/d intensity gain factor at small waveguide diameter.

(3)   For high enough pump power, the dependence of the optimum FIR output power on waveguide diameter becomes very mild, and the realization of a compact waveguide FIR laser at 118 μm with reasonable output power is therefore highly feasible.

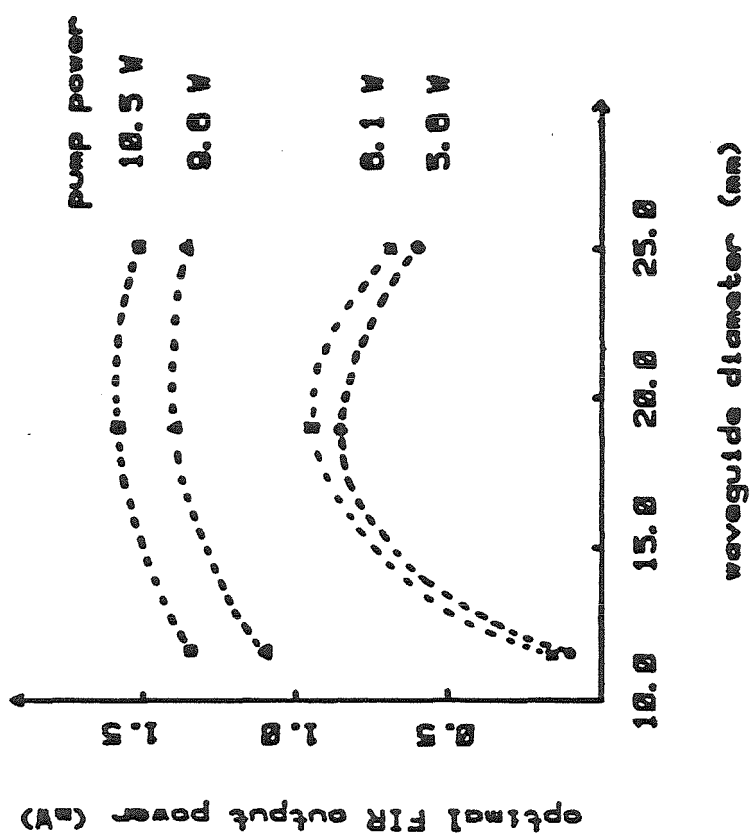Fig. 5.6 FIR output power (at optimum CH$_3$OH pressure) vs
waveguide diameter for various pump powers.

References for Chapter 5

5.1   M. Yamanaka and H. Yoshinaga, "Compact waveguide lasers in the submillimeter and millimeter wave regions," Conf. Digest, *International Conf. on Submillimeter Wave and Their Applications*, Atlanta, June 1974, pp. 26-27.

5.2   L.D. Fesenko and S.F. Dyubko, "Optimization of the parameters of optically pumped submillimeter lasers," *Sov. J. Quantum Electron.*, Vol. 6, No. 7, July 1976, pp. 839-843.

5.3   A. Tanaka, et al.,"CW efficient optically pumped FIR waveguide NH_3 lasers," *Optics Comm.*, Vol. 22, No. 1, July 1977, pp. 17-21.

5.4   J.M. Lourtioz and R. Adde, "Diagnostic experiments and modeling of 118 μm CH_3OH laser," *J. Physique*, 41, March 1980, pp.251-258.

5.5   Y. Kokubo, et al.,"CW CH_3F metallic waveguide laser at 496 μm," *The Trans. of The IECE of Janpan*, Vol. J64-C, No.1, Jan. 1981, pp. 16-23.

5.6   D.T. Hodges, F.B. Foote and R.D. Reel, "High power operation and scaling behavior of cw optically pumped waveguide lasers," *IEEE. J. Quantum Electron.*, Vol. QE-13, No.6, June 1977, pp. 491-494.

5.7   T.A. Galantowicz, et al.,"Characteristics of non-diffusion-limited optically pumped cw lasers : experimental results for CH_2F_2", *Proceeding of The International Conf. on Lasers*, 1978 Ed. V. J. Cocoran, STS Press, Mc Lean, Virginia 1979. pp. 121-125.

5.8   T.A. DeTemple and E.J. Danielewicz, "Continuous wave CH F waveguide laser at 496 μm: theory and experiment," *IEEE. J. Quantum Electron.*, Vol. QE-12, No. 1, Jan. 1976, pp. 40-47.

5.9   H.P. Roser and G.V. Schultz, "Development of an optically pumped molecular laser," *Infrared Phys.*, Vol. 17, 1977, pp. 531-536.

CHAPTER 6. SUMMARY OF THE EXPERIMENTAL AND THEORETICAL FINDINGS.

This thesis is the result of an exploration of some of the fundamental problems in optically pumped FIR waveguide lasers; the work was undertaken in order to reach a better understanding of the physics involved and to obtain a better set of engineering design parameters. Of particular interest here are the effects of small waveguide on FIR laser performance so that the factors that limit the compactness of an FIR waveguide laser can be exposed.

In order to distinguish the effects due to waveguide diameter from those produced by changing the output mirror coupling configuration it was necessary to develop and use a uniform output coupler, with unique IR and FIR properties. Since such a coupler was not commercially available, various options were analyzed, and a successful configuration was designed and built. The major results of our investigation on dielectric-coated silicon mirrors can be summarized as follow :

(1)　A simple silicon etalon, with or without a multilayer dielectric coating for high IR reflectance, typically overcouples the FIR radiation, and the laser performance is far from optimum.

(2)　Even for an IR coating as thin as a few microns, the measured FIR properties for the same sample before and after the coating may differ significantly, in contrast to Durschlags' results.

(3)　A tradeoff between absorption loss and diffraction loss due to surface distortion has to be made in choosing the appropriate wafer thickness. Our experience with thin silicon wafers (thickness $\sim 300~\mu m$ to $700\mu m$) reveals that the surface distortion due to mechanical stress induced by the mounting method can result in significant loss because of the mode distortion.

(4) A coated silicon mirror can be used in conjunction with another uncoated silicon wafer or a metal mesh to increase the FIR reflectance to approximately 85 % with only a small increase (typically 3% to 10%, depending on the quality of the latter) in FIR loss.

FIR output power stability was found to be a critical requirement for a reliable experimental parametric study. There are some apparent conflicts between the requirements for rigidity of the FIR laser structure (for better power stability) and the requirements on experimental flexibility (to vary the parameters of interest within a reasonably wide range). The factor that plays the most crucial role in our case, however, turned out to be the frequency stability of CO_2 pump laser output. The CO_2 laser frequency has to be locked to within an extremely narrow window in the vicinity of the CH_3OH absorption peak in order that the FIR laser output power be reasonably stable. The optoacoustic frequency stabilization technique using a simple internal spectrophone proved to be very convenient and effective.

The results of the experimental parametric study given in Figs. 5.1-5.6 can be summarized as follow :

(1) For a given set of experimental conditions, with laser gas pressure being the only varying independent parameter, there exists a specific pressure at which the FIR output is optimum and a cutoff pressure beyond which the FIR laser ceases to lase.

(2) For a given waveguide diameter, the optimum pressure varies linearly with pump power (for pump power ranging from 5 W to 11.5 W and waveguide diameter in the range of 11.5 mm to 25 mm).

(3) For a given pump power, the optimum pressure varies linearly with the inverse waveguide diameter $(1/d)$.

(4) The optimum FIR output power varies linearly with the pump power.

(5) For a given pump power, the optimum FIR output power (optimized with respect to laser gas pressure) increases as the waveguide diameter increases from a small value, achieves a local maximum, and decreases as the waveguide diameter increases further. The optimum waveguide diameter is in the vicinity of 19 mm in our case and is independent of the pump power.

Two different theoretical models were used in sections 2.3 and 2.4 to analyze FIR laser performance. In Hodges' phenomenological model (Sec. 2.3), Tucker's positive gain criterion plays the crucial role, and the dependence of FIR output power on pressure is essentially controlled by the diffusion contribution to vibrational relaxation. Note that the factor $[1 - f_2 (\frac{f_3/g_3}{f_2/g_2} - 1)\frac{\Gamma_j}{\Gamma_0}]$ is a monotonically decreasing function of pressure and changes from positive to negative values at a certain pressure (the cutoff pressure), depending only on the molecular dynamics, and the statistical properties of the energy levels. Existence of an optimum pressure is ensured by the pump absorption term $[\frac{\gamma L}{\gamma L + A_p}]$ which vanishes as the pressure goes to zero, and saturates to a constant value approximately equal to unity at the high pressure limit. Although the exact location of the optimum pressure is affected by both factors, the dependence on the former turns out to be much stronger.

The factor $[1 - f_2 (\frac{f_3/g_3}{f_2/g_2} - 1)\frac{\Gamma_j}{\Gamma}]$ also appears in Lourtioz and Adde's model via the excited state FIR absorption term A_e. This term was however considered to be small compared with the other contribution and was neglected by Lourtioz and Adde in their calculation. Without justification, we have made the further approximation $A_e = 0$ to make the mathematics manageable with waveguide

diameter and pressure as independent variables. Comparison with Lourtioz's result indicates that the excited state FIR absorption may strongly affect not only the FIR output power but also the optimum pressure and the cutoff pressure. For the particular cases we compared, the output power is reduced to about 1/3 of our calculated values, and both the optimum and the cutoff pressures are reduced to approximately half of our calculated values.

The agreement between the results predicted by the two models is surprisingly good for the case of the CH_3F 496 μm line, considering all the simplifications and approximations involved. We speculate that the diffusion contribution to vibrational relaxation for CH_3OH 118 μm line is indeed approximately ten times compared with that for CH_3F, because the same degree of agreement is expected for the case of CH_3OH 118 μm line.

Although the results predicted by the simplified model of Lourtioz and Adde's agree, at least semi-quantitatively, with all our experimental observations, there are too many adjustable parameters for the model to be useful as a design tool. Better knowledge of these parameters and the development of a suitable numerical algorithm for solving the implicit equation for FIR output power are certainly required for further analysis. Unless the λ^2/a^3 waveguide loss can be significantly reduced by one way or another, compact FIR waveguide laser will be difficult to realize, particularly for those laser lines in the long wavelength end of the FIR spectrum.

PART II

FOLDED FABRY-PEROT QUASI-OPTICAL RING RESONATOR DIPLEXER :

THEORY AND EXPERIMENT

CHAPTER 1. INTRODUCTION

The coherent detection technique also known as heterodyne radiometry is well known in the microwave and radio frequency regions. The basic idea is to direct the incoming signal of interest and a local oscillator signal onto the surface of a radiation detector where a current at the difference frequency of the two beams is generated via the nonlinear process. The beat current is called the signal current. The effect of mixing the incoming signal beam with a powerful local oscillator is to generate the signal current and the rms shot noise current both proportional to the square root of the local oscillator power. Thus the signal to noise ratio in the signal beam can be preserved, while the incoherent background noise is submerged. A diplexer is a component in the system that should serve, ideally, the dual purpose of injecting the two beams onto the surface of the detector with minimum loss and rejecting the noise from the local oscillator. This is illustrated schematically in Fig. 1.1.

With the invention of lasers, an opticl heterodyne detection system using laser as the local oscillator with appropriate optical components replacing the microwave counterparts has been developed. The design of diplexers is a difficult problem in the far-infrared region because the local oscillators available in this spectral region produce limited output power, and a successful design must not waste any of that scarce local oscillator power. Conventional microwave techniques cannot be used for diplexing because of their high losses in the FIR region of the electro-magnetic spectrum.

incoming signal of interest

local oscillator (lo)
signal

diplexer

narrow band pass for
lo noise rejection and
low loss for lo signal
transmission.

f_{lo} f_s

wide band pass and
low loss for signal
transmission.

mixer

$f_{lo} \pm f_s$

I-F
amplifier

$f_{lo} - f_s$
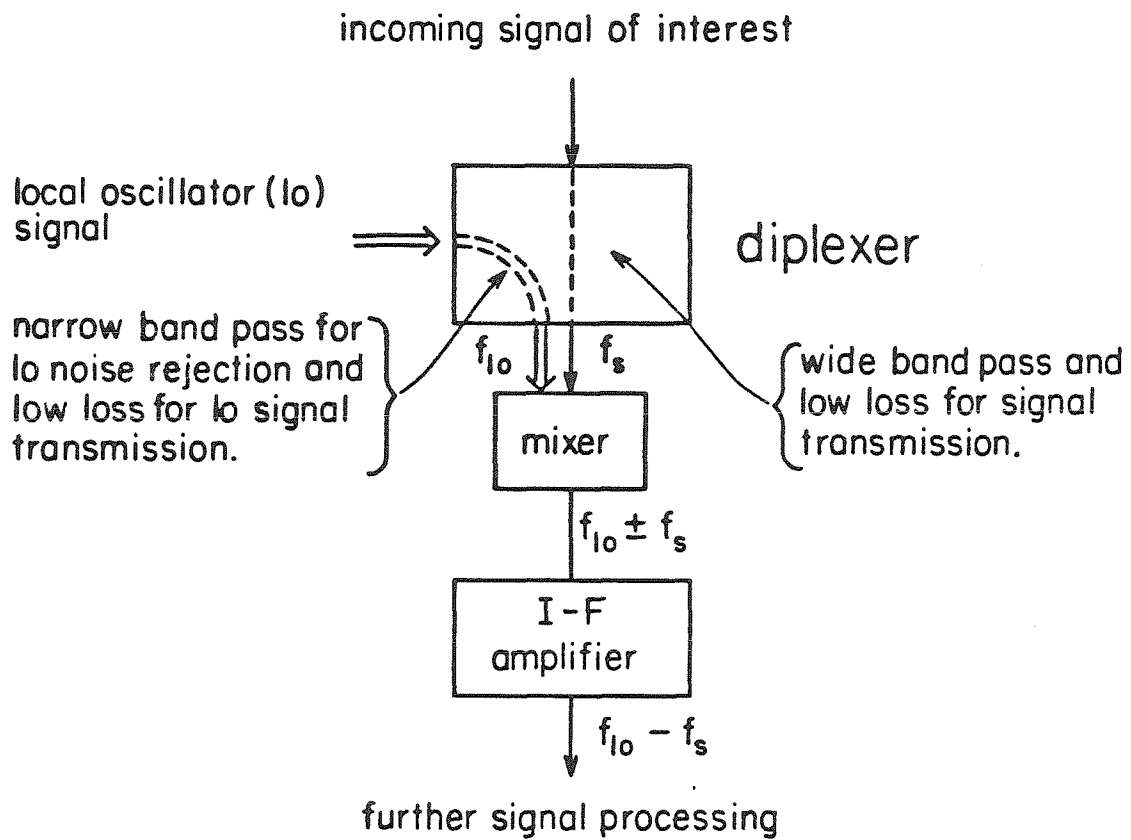
further signal processing

Fig. 1.1   Schematic diagram of the role of a diplexer in a
           heterodyne detection system.

A folded Fabry-Perot resonator with plane parallel reflectors, which serves the purpose of filtering the noise and diplexing the local oscillator and signal energies into the mixer, was described and tested by Gustincic [1], [2]. The basic idea is illustrated in Fig. 1.2. The resonator is tuned by moving the mirror block so that the local oscillator input from port I is at resonant peak of the cavity and gets transmitted into port IV. The signal input at a slightly different frequency lies in the anti-resonant band of the cavity and gets reflected from port III into port IV. The transmission characteristic of the Fabry-Perot cavity is the well known Airy Function [3]. The advantage of the Fabry-Perot ring resonator diplexer over the two beam interferometer diplexer [4], whose transmission characteristic is of sinusoidal nature, lies in the fact that the Fabry-Perot resonator, with the Finesse $F \gg 1$, has a better noise rejection factor for the local oscillator input port and also a much wider reflection band for the signal port. The advantage of this type of Fabry-Perot cavity over the infinite slab Fabry-Perot resonator analyzed by Arnaud et al [5] and by Goldsmith [6] is that geometrical walk-off loss is eliminated. Other types of diplexers were described by Nakajima and Watanabe [7].

In chapter 2, we give qualitative treatment on how diffraction limits the performance of the diplexer and introduces a simple solution to minimize diffraction. Mathematical formulation of the problem on diplexer performance, its underlying assumptions, detailed analysis, and theoretical results are given in chapter 3. Some of the mathematical details are given in the Appendix. Experimental results at 100 GHz are presented in chapter 4. In chapter 5, we conclude by summarizing our results with a description on how they can be applied to estimate the figure of merit of the diplexer with a curved reflector as compared to one with plane reflectors.

PORT IV
(OUTPUT TO MIXER)

PORT III
(SIGNAL INPUT)

MESH

FIXED
MIRROR

MOVABLE
MIRROR
BLOCK

MESH

TOP VIEW
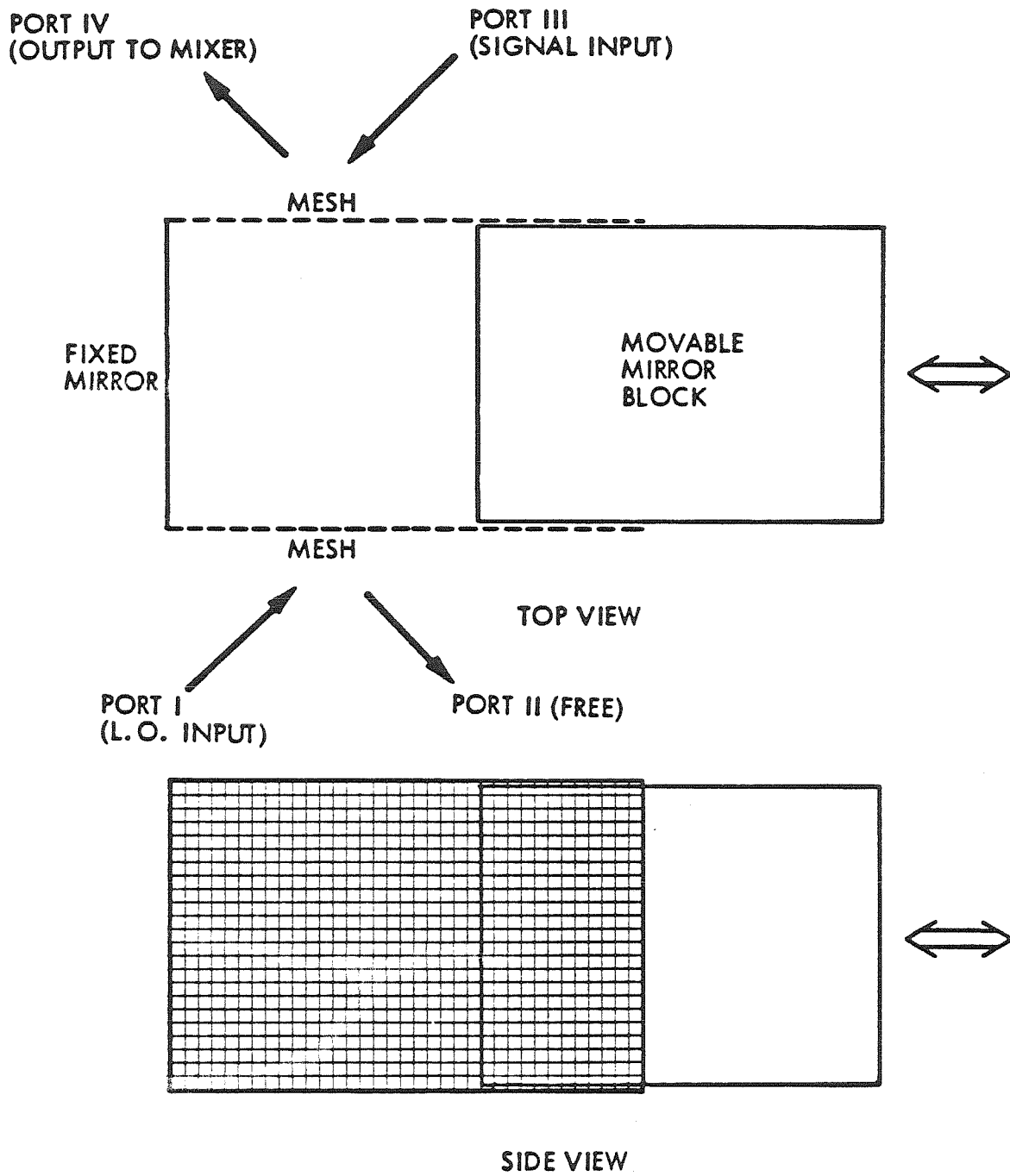
PORT I
(L.O. INPUT)

PORT II (FREE)

SIDE VIEW

Fig. 1.2 Schematic diagram of a folded Fabry-Perot ring resonator diplexer.

Chapter 2. EFFECT OF DIFFRACTION AND THE RELATED DESIGN PROBLEM

For applications in the millimeter and submillimeter wave regions, the performance of the diplexer is essentially limited by diffraction effects. Diffraction in the vertical direction results in energy loss of the system, since the top and bottom of the cavity are open, while diffraction in horizontal direction couples port III and port IV together so that a significant fraction of the local oscillator input energy is distributed into port III. This can be visualized by conceptually propagating the input beam through a lattice of virtual cavities, as is illustrated in Fig. 2.1. These diffraction problems can be reduced by replacing one of the plane reflectors with a curved mirror with surface properly designed to phase match a Gaussian beam with an appropriate beam waist at the plane reflector, as shown in Fig. 2.2. A toroidal surface with horizontal radius of curvature twice that of the vertical turns out to be a very good approximation to the exact shape.

Steps leading to solution of the diplexer design problem follow:

(1) Choose the free spectral range (FSR) of the cavity so that it is twice the intermediate frequency f_{IF} of the system (i.e. FSR = $2f_{IF}$). The condition above fixes the width (W) and length (L) of the square cavity to $W = L = c/4\sqrt{2}f_{IF}$ where c is the velocity of light in free space.

(2) The appropriate beam waist radius (w_0) and the Raleigh length (Z_R) are given by $w_0 = W/3\sqrt{2}$; $Z_R = \pi w_0^2/\lambda$ where λ is the free space space wavelength. This choice gives a Gaussian amplitude on the mesh which has a waist parameter equal to 1/3 of the cavity width.

(3) The horizontal and vertical radii of curvature for the torodial surface are determined by $R_h = 2L + Z_R^2/L$; $R_v = R_h/2$.

Fig. 2.1 Horizontal diffraction effect: a schematic illustration.
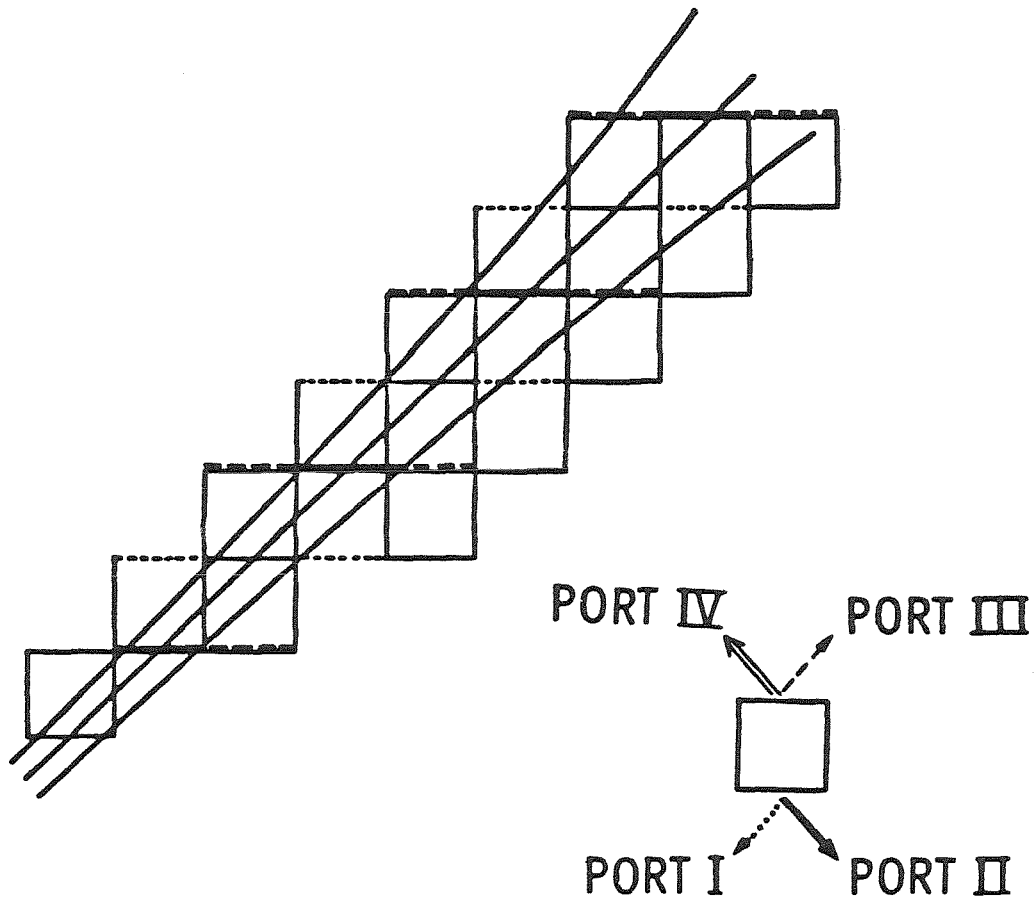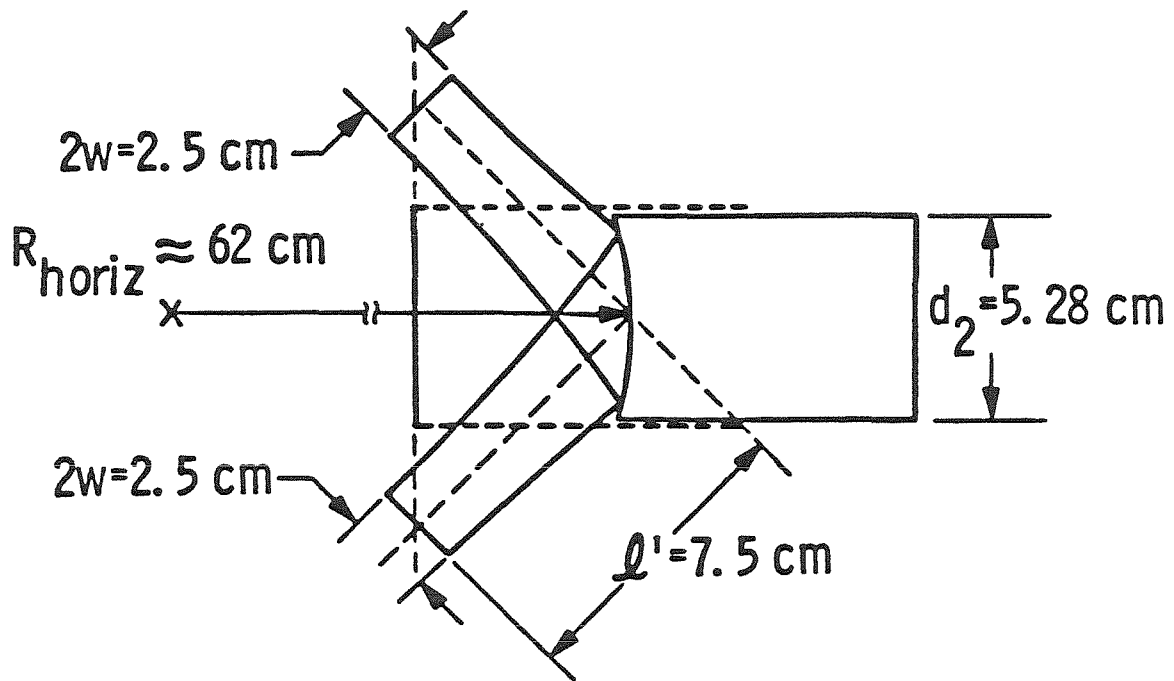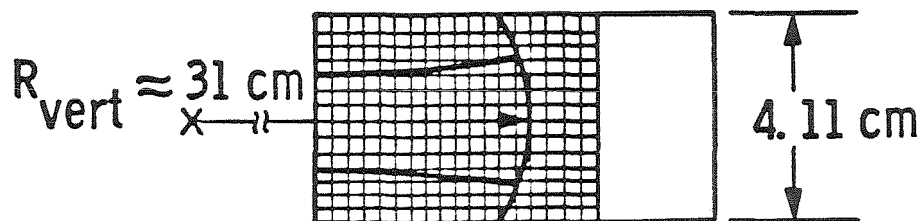
2w=2.5 cm

$R_{horiz} \approx 62$ cm

2w=2.5 cm

d_2=5.28 cm

ℓ'=7.5 cm

(a)

$R_{vert} \approx 31$ cm

4.11 cm

(b)

Fig. 2.2 Reflector surface design for minimum diffraction.
(a) Top view. (b) Side view.

Following the steps listed above, we have constructed an experimental model based on the following parameters: f_{IF} = 1 GHz, W = L= 5.30cm, w_0 = 1.25cm, λ = 0.3cm, R_h = 62cm, R_v = 31cm. In order to separate the effect of diffraction in vertical direction from that in horizontal direction, a resonator with a cylindrical reflector designed to control only the vertical diffraction loss was also constructed and tested. Our experimental models also included a diplexer with plane reflectors, so that the total effect of diffraction in both directions can also be observed. Preliminary experimental results of these studies were reported at the Sixth International Conference on Infrared and Millimeter Waves [8].

Although the simple cavity model described above leads us to the optimum curvature with minimum diffraction effect, it is far too simple to predict how much improvement one should expect by introducing the phase-matching curved reflector. The formalism used by Arnaud et al [5] can be in principle used to predict transmission of the flat wall and curved wall geometries. However, the results of the walk-off analysis presented in that paper are not applicable here because of the special boundary conditions imposed by the reflecting mirrors. The flat mirror case is formally equivalent to the case treated by Arnaud if the single detector is replaced by an array of detectors. The curved mirror case is more difficult because edge diffraction from the aperture of the cavity becomes significant. Description of the cavity in terms of its resonant modes is more convenient in the high finesse case where edge diffraction is important because the effects are included implicitly. An analysis based on a modal expansion will be described in the next section.

Chapter 3. MATHEMATICAL FORMULATION AND ANALYSIS

An exact three-dimensional analysis of the diplexer performance with a curved reflector is fairly complicated, so we seek some simplifying approximation. For practical application in the millimeter and submillimeter wave region, where the curvatures are mild, we can assume that diffraction effects in vertical and horizontal directions can be decoupled. The original problem is thus resolved into two simpler problems, namely, a one-dimensional infinite strip resonator problem for treatment of vertical diffraction loss, and a two-dimensional waveguide problem for treatment of horizontal diffraction effects. The two are decoupled in the sense that solution from the first part enters only as a parameter into the second.

3.1   Infinite Strip Resonator Model

For the plane resonator diplexer, the infinite strip plane resonator model of Barone [9] is used to approximate the eigenfunction and the diffraction loss associated with each mode in the vertical direction. The excitation efficiency of each mode by various input beams (plane wave and Gaussian beams with various beamwaist sizes) is evaluated by the overlap integral of the input function and the eigenfunction of each mode. For the cylindrical and toroidal resonator diplexers, the diffraction loss in the vertical direction is estimated by the infinite-strip cylindrical resonator model of Boyd and Gordon [10]. The dimensions of the actual cavity and the associated models are illustrated in Fig. 3.1, with Fresnel Numbers and round-trip amplitude diffraction losses of the fundamental modes given in the lower part of the figure.

PLANE RESONATOR   CYLINDRICAL RESONATOR

$d_1 = 5.28$ cm

$R \approx 31$ cm (FOR $2w = 2.5$ cm)

SIDE VIEW $2a = 4.11$ cm

TOP VIEW $d_2 = 5.28$ cm

L = 3.74 cm

1-D MODEL

$2a = 4.11$ cm

$L'' = 4L = 15$ cm

$R \approx 31$ cm

$L' = L = 3.74$ cm

FRESNEL NO. $N' = a^2 / \lambda L' \approx 3.8$ $N'' = a^2 / \lambda L'' \approx 1$

DIFFRACTION LOSS   0.34   0.002
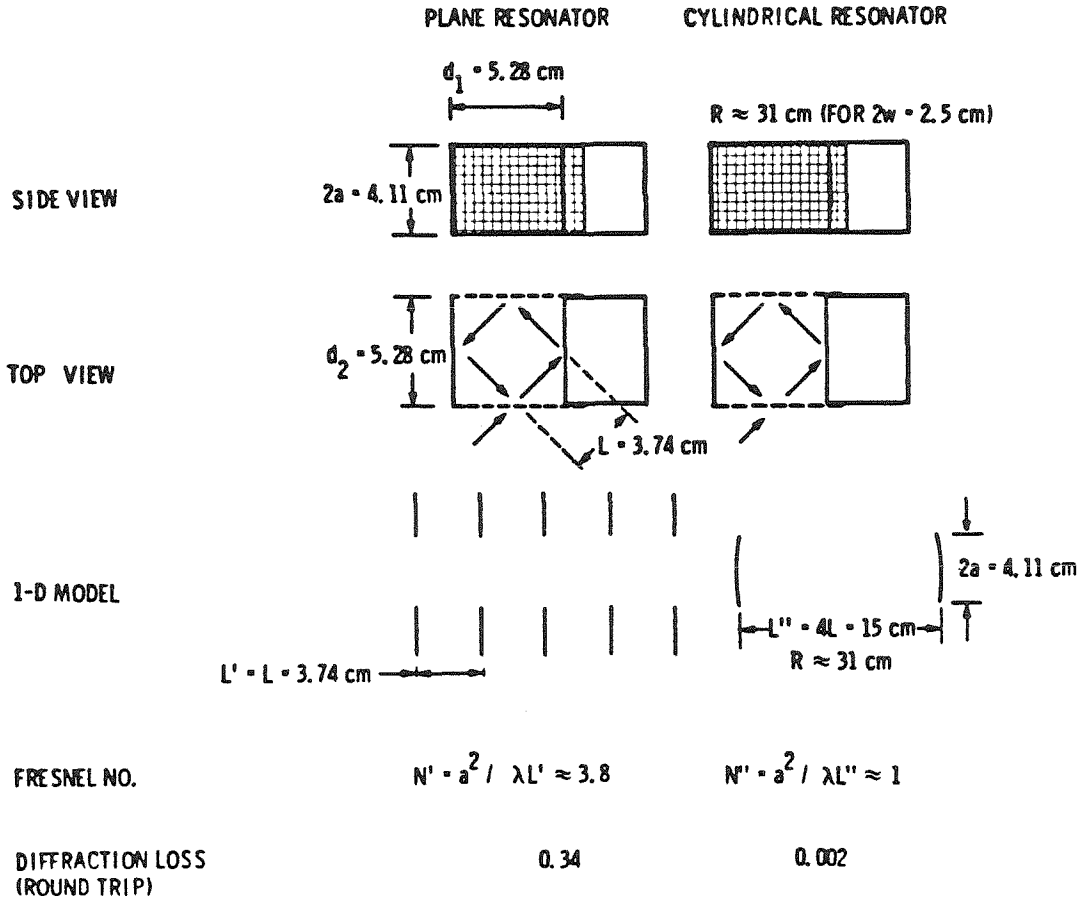(ROUND TRIP)

Fig. 3.1   Estimation of vertical diffraction loss by one dimensional
ifinite strip resonator model.

3.2 Two Dimensional Waveguide Problem

The mathematical formulation of the two dimensional waveguide problem, together with the appropriate coordinate system is illustrated in Fig. 3.2. The dependence on the y-coordinate is ignored, since the effect of field variations in y direction is separately taken into account by section 3.1, as explained at the beginning of this section. The electric and magnetic fields at z=0 and z=W can be expanded in terms of the complete basis set as

$$E_y(z=0) = \sum_n e_n \sqrt{2/L_g} \sin(n\pi x/L_g) \tag{3.1a}$$

$$H_x(z=0) = \sum_n h_n \sqrt{2/L_g} \sin(n\pi x/L_g) \tag{3.1b}$$

$$E_y(z=W) = \sum_n e'_n \sqrt{2/L_g} \sin(n\pi x/L_g) \tag{3.1c}$$

$$H_x(z=W) = \sum_n h'_n \sqrt{2/L_g} \sin(n\pi x/L_g) \tag{3.1d}$$

where all the e'_n, h'_n, e_n, and h_n are complex in general.

Symbolically, we can express the expressions above as

$$\begin{pmatrix} E \\ H \end{pmatrix}_{z=0} = \begin{pmatrix} e \\ h \end{pmatrix} \tag{3.1e}$$

$$\begin{pmatrix} E \\ H \end{pmatrix}_{z=W} = \begin{pmatrix} e' \\ h' \end{pmatrix} \tag{3.1f}$$

For an input beam linearly polarized in y direction, we consider only the TE modes since the TM modes are not significantly coupled to our input beam.

Assume that we have a transmission matrix $\underset{\sim}{T}$ that transforms the E and M fields at z=0 to those at z=W, so that

$$\begin{pmatrix} e' \\ h' \end{pmatrix} = \underset{\sim}{T} \begin{pmatrix} e \\ h \end{pmatrix} \tag{3.2}$$
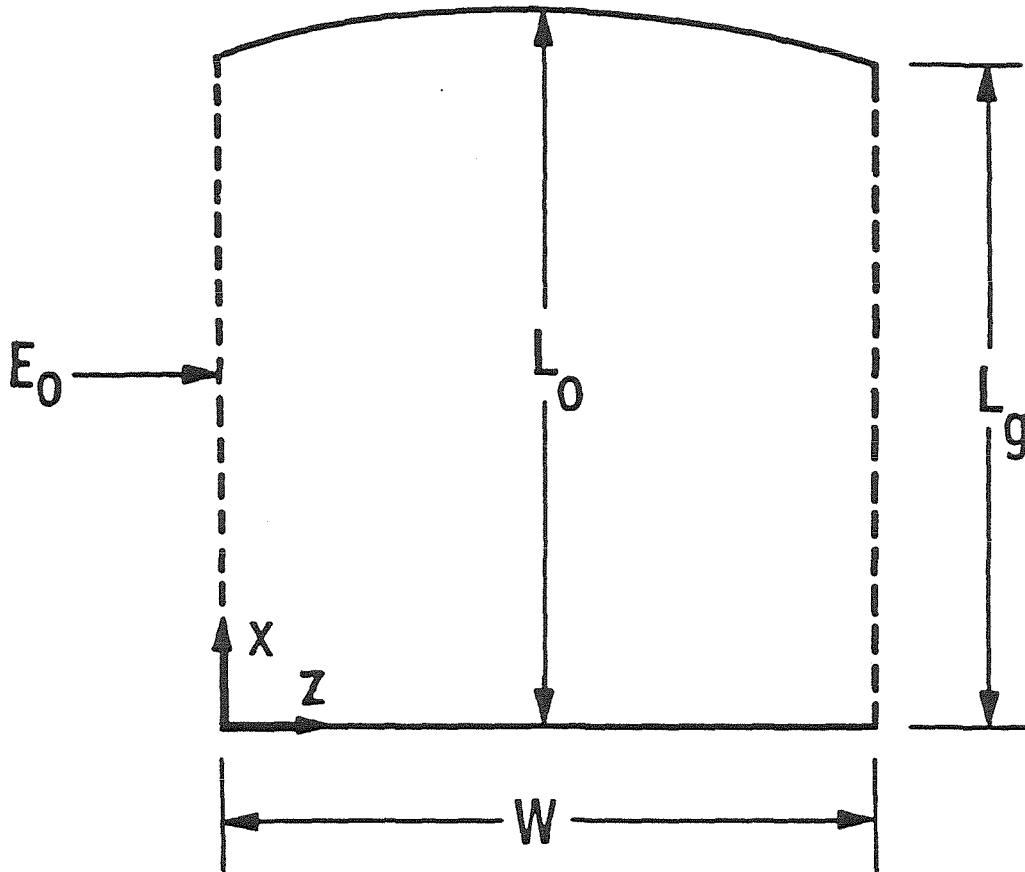
Fig. 3.2 Dimensions and coordinates associated with the two
dimensional waveguide analysis.

The eigenvalue problem of the waveguide can then be expressions

$$\underset{\sim}{T}\, \underset{\sim}{u}_\alpha = \Lambda_\alpha \, \underset{\sim}{u}_\alpha = \exp(i\phi'_\alpha)\underset{\sim}{u}_\alpha \tag{3.3}$$

where $\underset{\sim}{u}_\alpha$ and Λ_α are the eigenvectors and the eigenvalues of the waveguide. The procedure for determination of the $\underset{\sim}{T}$ matrix will be described in the Appendix.

In general, $\underset{\sim}{T}$ will be a non-symmetric real matrix, and the eigenmodes will appear in pairs with eigenvalues given by $\exp(\pm i\phi')$, representing forward and backward going waves.

If we represent the eigenvectors in the basis set as

$$U_\alpha = \begin{pmatrix} u_{1\alpha} \\ u_{2\alpha} \\ \cdot \\ \cdot \\ \cdot \\ \cdot \end{pmatrix} \, , \tag{3.4}$$

then the associated eigen-functions ψ_α will be given by

$$\psi_\alpha = \sum_n u_{n\alpha} \sqrt{2/L_g} \, \sin(n\pi x/L_g) \tag{3.5}$$

Consider a linearly polarized input beam from port I with the electric field vector given by $\underset{\sim}{E} = E_0(x)\underset{\sim}{y}$ at z=0. If we ignore the magnetic part and also the impedence mismatch between free space and the waveguide, we can expand the incoming field in terms of the complete set of basis functions as

$$E_0(x) = \sum_n S_n \sqrt{2/L_g} \, \sin(n\pi x/L_g), \tag{3.6}$$

where $\quad S_n = \sqrt{2/L_g} \int_0^{L_g} \sin(n\pi x/L_g)E_0(x)dx. \tag{3.7}$

$E_0(x)$ can also be expressed in terms of the eigenfunctions as

$$E_0(x) = \sum_\alpha{}' n_\alpha \psi_\alpha, \tag{3.8}$$

where the prime is used to symbolize the fact that the summation should run

only over the "E-parts" of the eigenfunctions with eigenvalues representing the forward-going waves. Using (3.5), we can rewrite (3.8) as

$$E_0(x) = \sum_{\alpha n} n_\alpha V_{n\alpha} \sqrt{2/L_g} \sin(n\pi x/L_g),$$

(3.9)

where V is the submatrix of u which couples the E field with the forward going eigenmodes. By comparing (3.6) and (3.9), we have

$$\sum_\alpha n_\alpha V_{n\alpha} = S_n,$$

(3.10)

or

$$n_\alpha = \sum_n V^{-1}{}_{\alpha n} S_n.$$

(3.11)

Each eigenmode propagates independently through the Fabry-Parot, with amplitude transmittance and reflectance given by [3]

$$t_\alpha = n_\alpha t^2 \Lambda_\alpha / (1 - r^2 \Lambda_\alpha^2),$$

(3.12a)

$$r_\alpha = n_\alpha [r + t^2 \Lambda_\alpha^2 / (1 - r^2 \Lambda_\alpha^2)],$$

(3.12b)

where r and t are the amplitude reflection coefficient and the amplitude transmission coefficient of the interfaces. From (3.9), (3.11) and (3.12), the total transmitted and reflected amplitudes can be expressed as

$$E_t = \sum_{\alpha n m} V^{-1}{}_{\alpha m} S_m V_{n\alpha} \sqrt{2/L_g} \sin(n\pi x/L_g)[t^2\alpha/(1-r^2\Lambda_\alpha^2)]$$

(3.13a)

$$E_r = \sum_{\alpha n m} V^{-1}{}_{\alpha m} S_m V_{n\alpha} \sqrt{2/L_g} \sin(n\pi x/L_g)[r+t^2\Lambda_\alpha^2/(1-r^2\Lambda_\alpha^2)]$$

(3.13b)

The fields E_t and E_r can be Fourier analyzed into far-field patterns. Alternatively, the amplitude received by a detector (receiver) can be determined by conceptually treating it as a transmitter and taking the overlap integral of its emitted amplitude distribution at an appropriate plane with the normalized amplitude distribution at the same plane of the field

to be detected. If the detector at port IV has the same geometry as the transmitter at port I, we have, from (3.6) and (3.7)

$$E_4^* = E_0 = \sum_n S_n \sqrt{2/L_g} \sin(n\pi x/L_g), \tag{3.14}$$

and

$$S_n = \sqrt{2/L_g} \int_0^{L_g} E_4^* \sin(n\pi x/L_g) \ dx. \tag{3.15}$$

The amplitude received by the detector at port IV is then given by

$$t_4 = \int_0^{L_g} E_4^* E_t \ dx. \tag{3.16}$$

Using (3.13a) and (3.14), we obtain

$$t_4 = \sum_{\alpha nm} V_{\alpha m}^{-1} \ V_{n\alpha} S_m \ S_n [t^2 \Lambda_\alpha / (1 - r^2 \Lambda_\alpha^2)] \tag{3.17}$$

Similarly, if $Q_n = \sqrt{2/L_g} \int_0^{L_g} E_3^* \sin(n\pi x/L_g) dx,$ $\tag{3.18}$

then $t_3 = \sum_{\alpha nm} V_{\alpha m}^{-1} V_{n\alpha} \ S_m Q_n [t^2 \Lambda_\alpha / (1 - r^2 \Lambda_\alpha^2)].$ $\tag{3.19}$

For port I and port II, we have

$$r_1 = \sum_{\alpha nm} V_{\alpha m}^{-1} \ V_{n\alpha} \ S_m S_n [r + t^2 \Lambda_\alpha^2 / (1 - r^2 \Lambda_\alpha^2)], \tag{3.20}$$

$$r_2 = \sum_{\alpha nm} V_{\alpha m}^{-1} \ V_{n\alpha} \ S_m \ Q_n [r + t^2 \Lambda_\alpha^2 / (1 - r^2 \Lambda_\alpha^2)]. \tag{3.21}$$

As an illustrative example, let us apply the procedure described above to analyze the simplest special case where both side-walls of the waveguide are flat. The transformation matrix $\underset{\sim}{T}$ is given by

$$\underset{\sim}{T} = \underset{\sim}{T_1} \times \underset{\sim}{T_2} \times \ldots \times \underset{\sim}{T_n} \times \ldots \qquad (3.22)$$

$$\underset{\sim}{T_n} = \begin{pmatrix} \cos(k_n W) & \sin(k_n W)/k_n \\ -k_n \sin(k_n W) & \cos(k_n W) \end{pmatrix}, \qquad (3.23)$$

and $k_n^2 = (2\pi/\lambda)^2 - (n\pi/L_g)^2.$ \qquad (3.24)

The eigenvectors $\begin{pmatrix} 1 \\ ik_n \end{pmatrix}$ and $\begin{pmatrix} 1 \\ -ik_n \end{pmatrix}$ satisfy the eigenvalue equations

$$\underset{\sim}{T_n} \begin{pmatrix} 1 \\ ik_n \end{pmatrix} = \exp(ik_n W) \begin{pmatrix} 1 \\ ik_n \end{pmatrix} \text{ and } T_n \begin{pmatrix} 1 \\ -ik_n \end{pmatrix} = \exp(-ik_n W) \begin{pmatrix} 1 \\ -ik_n \end{pmatrix},$$

as can be easily verified.

For an input plane wave from port I with incident angle $= \theta$

$$E_0(x) = \sqrt{2/L_g} \exp[ik_0 \sin\theta(x - L_g/2)] = E_4^*(x), \qquad (3.25)$$

$$E_3^*(x) = \sqrt{2/L_g} \exp[-ik_0 \sin\theta(x - L_g/2)]. \qquad (3.26)$$

From (7) and (18) we have

$$S_n = \sqrt{2/L_g} \int_0^{L_g} \sin(n\pi x/L_g) \exp[ik_0 \sin\theta(x - L_g/2)] dx, \qquad (3.27)$$

$$Q_n = S_n^*. \qquad (3.27a)$$

By straightforward integration, we get

$$S_n = -i\, 1/2\, [\exp(n\pi i/2)\mathrm{sinc}(k_0 L_g \sin(\theta/2) + n\pi/2)$$
$$- \exp(-n\pi i/2)\mathrm{sinc}(k_0 L_g \sin(\theta/2) - n\pi/2)]. \qquad (3.28)$$

The field amplitude as "seen" by the detector at each port can be determined from (3.17) and (3.19) through (3.21).

The rapid decay of the "sinc" function with increasing argument ensures that the infinite sums over index n and m in the expression for t_4, t_3, r_2 and r_1 will have only a few terms (modes) adjacent to $q \simeq k_0 L_g \sin\theta/\pi$

that make a significant contribution. Furthermore, the V matrix turns out to be "almost diagonal" (i.e. the elements that are significantly different from zero are those along the diagonal, and in some cases, those adjacent to the diagonal), so that the infinite sum over index α also converges rapidly within a few terms in the neighborhood of $\alpha = q$. Most of the energy is thus carried via the mode $q \simeq k_0 L_g \sin\theta/\pi$ and the adjacent modes.

It is the interference between the q mode and adjacent modes which leads to the directivity. In Eq. (3.17) the contribution of the q mode to the sum by product $S_q S_q$ has a magnitude of ~1/2. The two adjacent modes together contribute 0.405. For t_4 the phase is such that these three modes add, while for t_3 the phase is such that these modes subtract. This picture, in which directivity is a consequence of interference between modes, persists to the case of the diplexer with a curved mirror. For the waveguide with one curved wall, most of the energy comes in two adjacent modes with propagation phase factors separated by almost π.

Using parameters for our experimental model with a curved mirror, theoretical phase dispersion curves for four of the eigenmodes have been computed and are plotted in Fig. 3.3. Note that the eigenmodes are labeled by index q such that $|u_{q\alpha}| \geq |u_{n\alpha}|$ for all n. Although this scheme introduces some ambiguity when two or more basis modes are almost equally dominant, it is convenient because it labels the particular basis mode that has maximum contribution.

The results of the numerical calculation also indicate that, for optimal Gaussian beam input excitation, only two of the eigenmodes are significantly coupled, and their phase difference δ turns out to be a crucial parameter that determines the transmission characteristics. We define δ as the fractional part of the phase difference measured in units

130
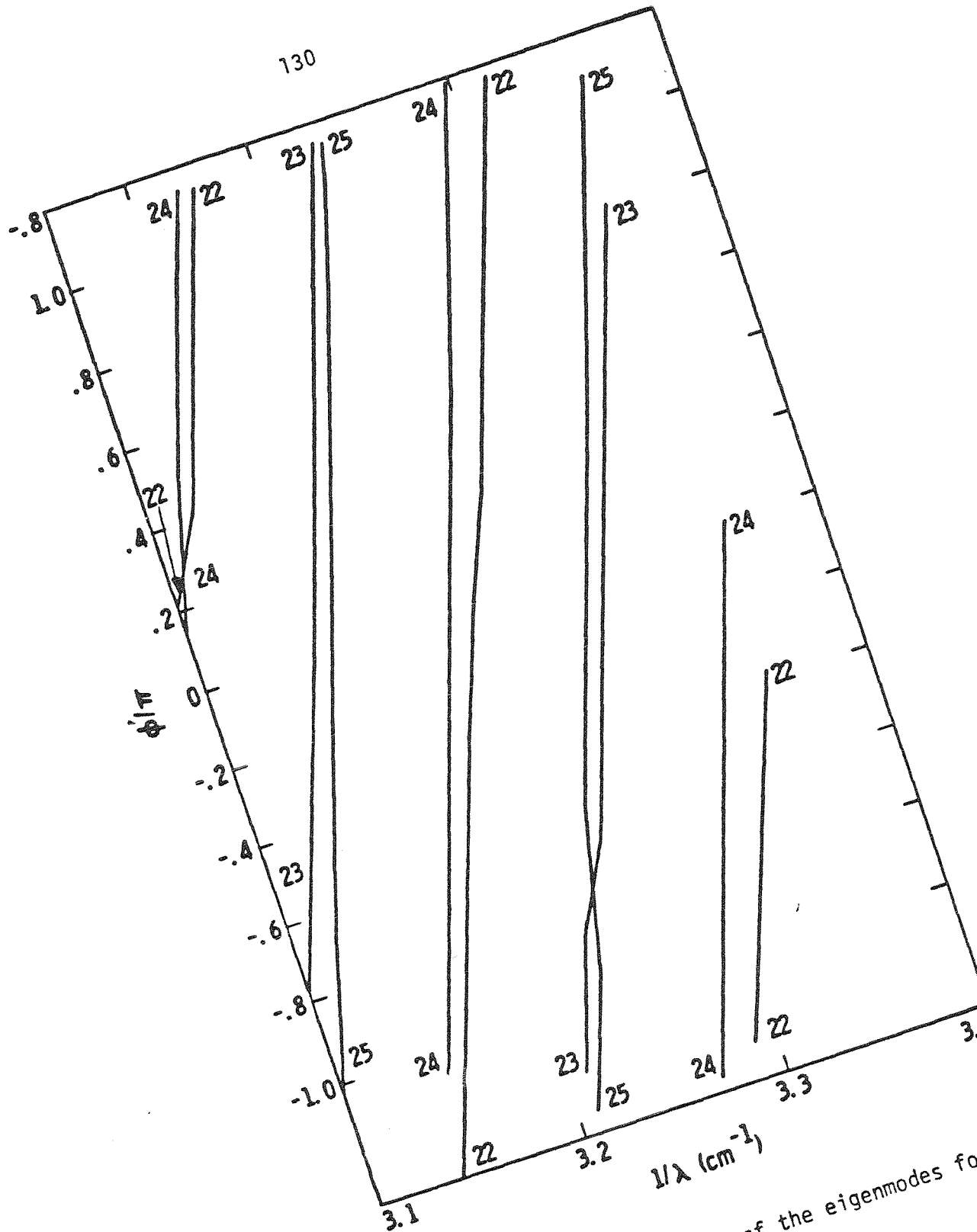
dispersion of four of the eigenmodes fo...
...5 28 cm, R = 60cm.

of π. Equivalently, δ is the frequency separation of the modes divided by the free spectral range. In Fig. 3.4, values of δ are plotted against L_0/R with $m \equiv 2L_g/\lambda$ as parameters. λ is the free space wavelength and the meaning of L_0, R and L_g are defined in the inset for Fig. 3.4. It is interesting to note that the results (circles) are fit very well by the empirical relation $\delta = \exp(-.0283m^2L_0/R)/m$ (straight lines).

The transmission into port IV, $|t_4|^2$, is plotted against the input Gaussian beamwaist-size with the radius of curvature of the waveguide as a parameter in Fig. 3.5 The arrows in the figure indicate the waist-sizes for which the input Gaussian beam is phase-matched to the curved surface illustrated in Fig. 2.2. The agreement with our waveguide analysis is excellent.

So far we have completely ignored the existence of metal meshes at the input and output planes of our waveguide. Reflectivities for metal meshes determine the finesse, F, of the diplexer. In practice, values of F are set by the system requirements. Since the finesse is the free spectral range in units of transmission linewidth, and δ is the phase difference of the two dominant eigenmodes in units of the free spectral range, the product $F\delta$ can be interpreted as the ratio of phase difference of the two dominant eigenmodes to that of the transmission linewidth. Transmission into port IV, $|t_4|^2$, for diplexers with flat and curved reflectors, are compared in Fig. 3.6 for various values of $F\delta$.

3.3 <u>Solutions to the three dimensional problem</u> - To convert the solutions (3.17), (3.19), (3.20) and (3.21) of the two-dimensional problems into those of the orignal three-dimensional diplexer problem, we have to consider the effects of finite size and curvature of the walls in the vertical direction. Diffraction loss due to finite size can easily be taken into account simply
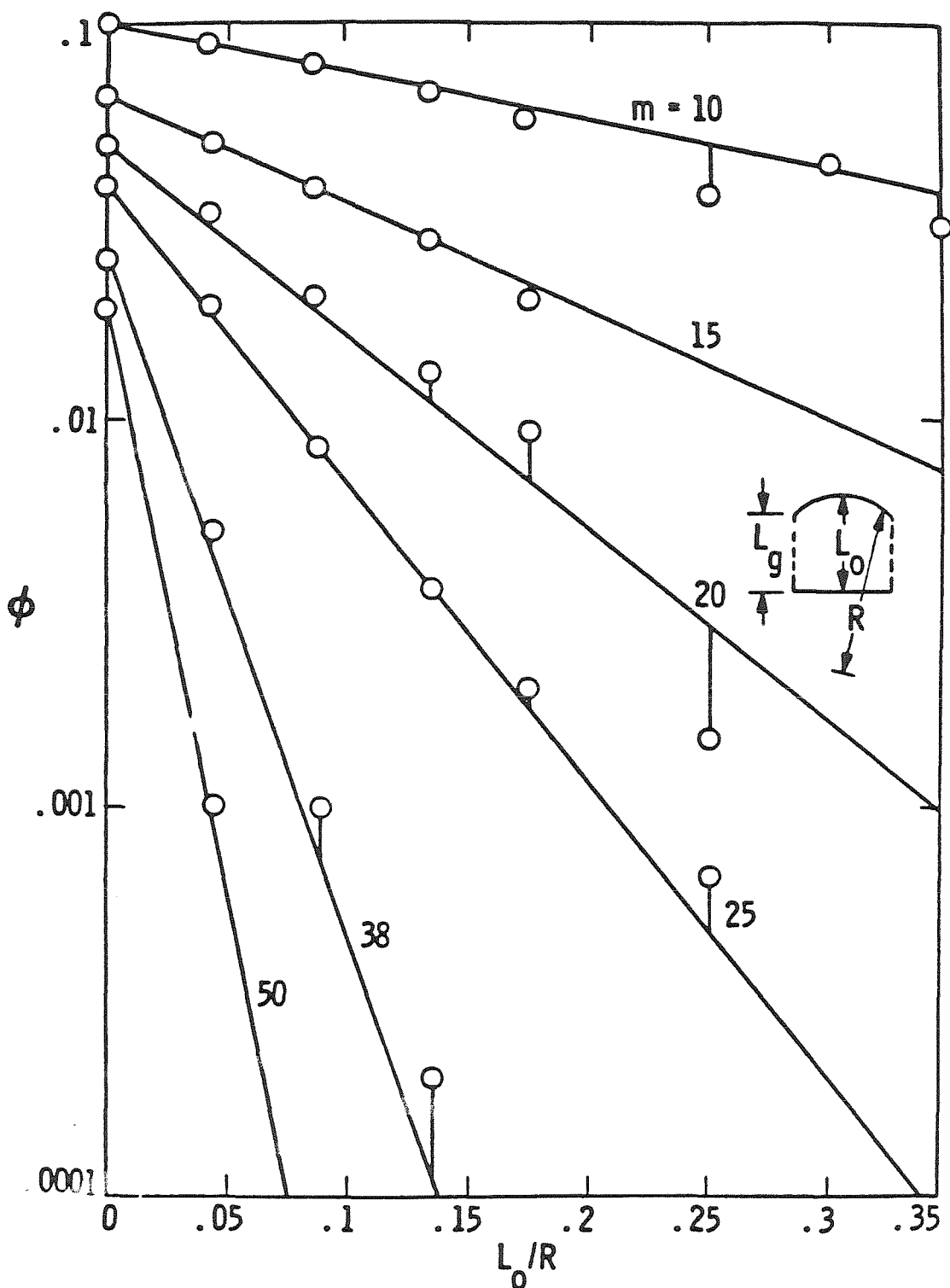
Fig. 3.4 Normalized phase difference, ϕ, of the two dominant eigenmodes vs. L_0/R. $m = 2L_g/\lambda$ is the resonant order. Straight lines represent the fit by the empirical relation $\phi = \exp(-0.0283m^2 L_0/R)/m$.
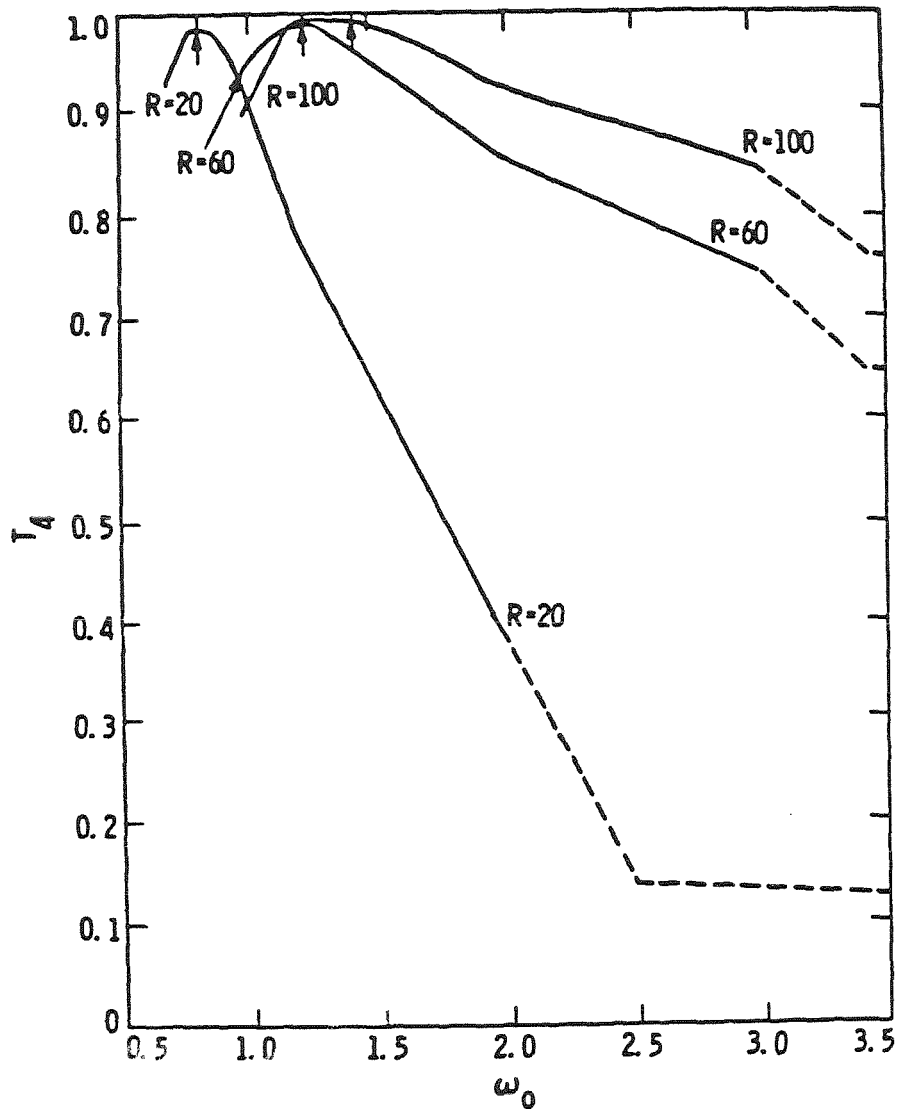
Fig. 3.5 Through-put (port IV) vs. waist-size of input Gaussian beam for different wall curvatures. Waist-sizes such that the beam phase-matched to the curved surface are indicated by arrows.

by replacing the amplitude reflectance r by rf and the amplitude transmittance t by $t\sqrt{f}$, where 1-f is the amplitude attenuation per round trip due to vertical diffraction loss. The values of 1-f are given in part A of this section. Under the conditions that loss factor is relatively small (i.e. 1-f<<1) and that the vertical curvature of the wall is mild so that the mode structure of the two dimensional waveguide analyzed in part B is not significantly distorted, the results obtained by this approach should represent a very good approximation to the solutions of the original problem. The effective finesse will be

$$F = \pi(rf)/(1-r^2f^2) \tag{3.29}$$

and

$$T_4' = T_4 (1-r^2)^2 f/(1-r^2f^2)^2 \tag{3.30}$$

where $T_4 \equiv |t_4|^2$ is the power transmission for port IV of the two dimensional problem (see Fig. 3.6), and T'_4 is the corresponding power transmission for the three-dimensional problem.

Chapter 4. EXPERIMENTAL RESULTS

Our experimental setup for transmission measurement in the vicinity of 100 GHz is shown in Fig. 4.1. Electroformed meshes (MN-40 from Buckbee-Mear Co.) are used as the partially transmitting mirrors at both sides of the diplexer. The monomodal approximation [11] is applied to free standing mesh model of Chen [12] to estimate their transmission characteristics. Experimental results at 100 GHz agree fairly well with theory. Experimental values of T'_4 (power transmission into port IV) for diplexers with different geometries of reflecting surfaces are compared in Fig. 4.2. In each case, values of T'_4 for the corresponding waveguides (i.e. with no meshes) are used as the 0 dB reference. Note that the peak values of T'_4 are improved
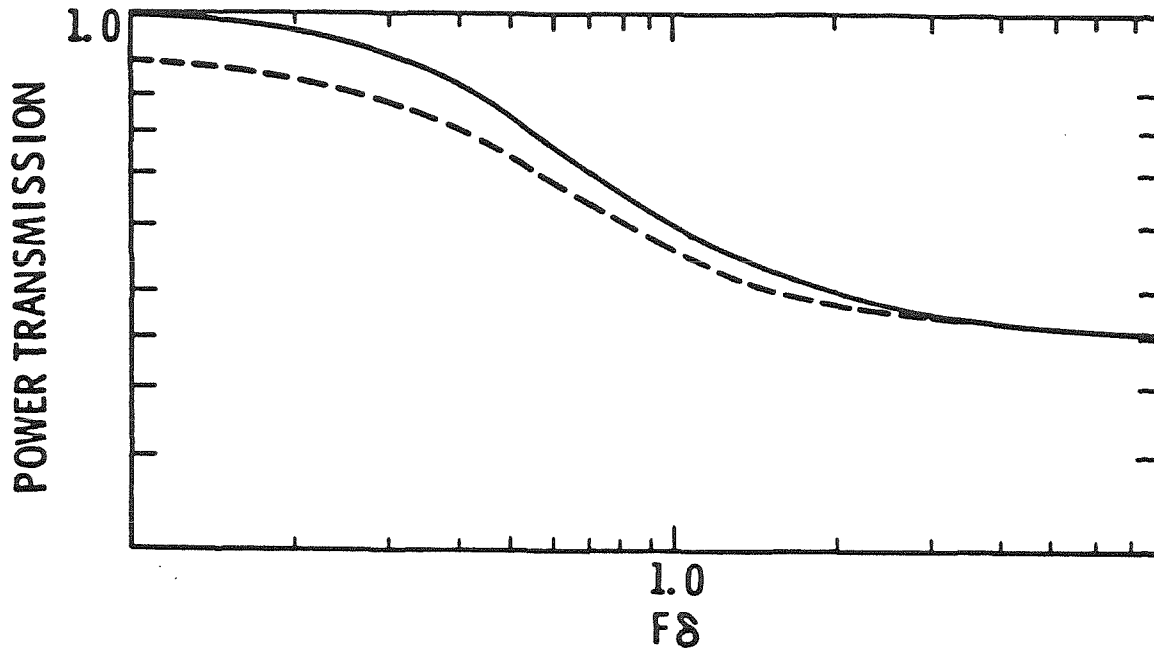
Fig. 3.6 Transmission (T$_4$) for diplexers with flat and curved reflectors vs. Fδ. (—— curved mirror, ---- flat mirror.)
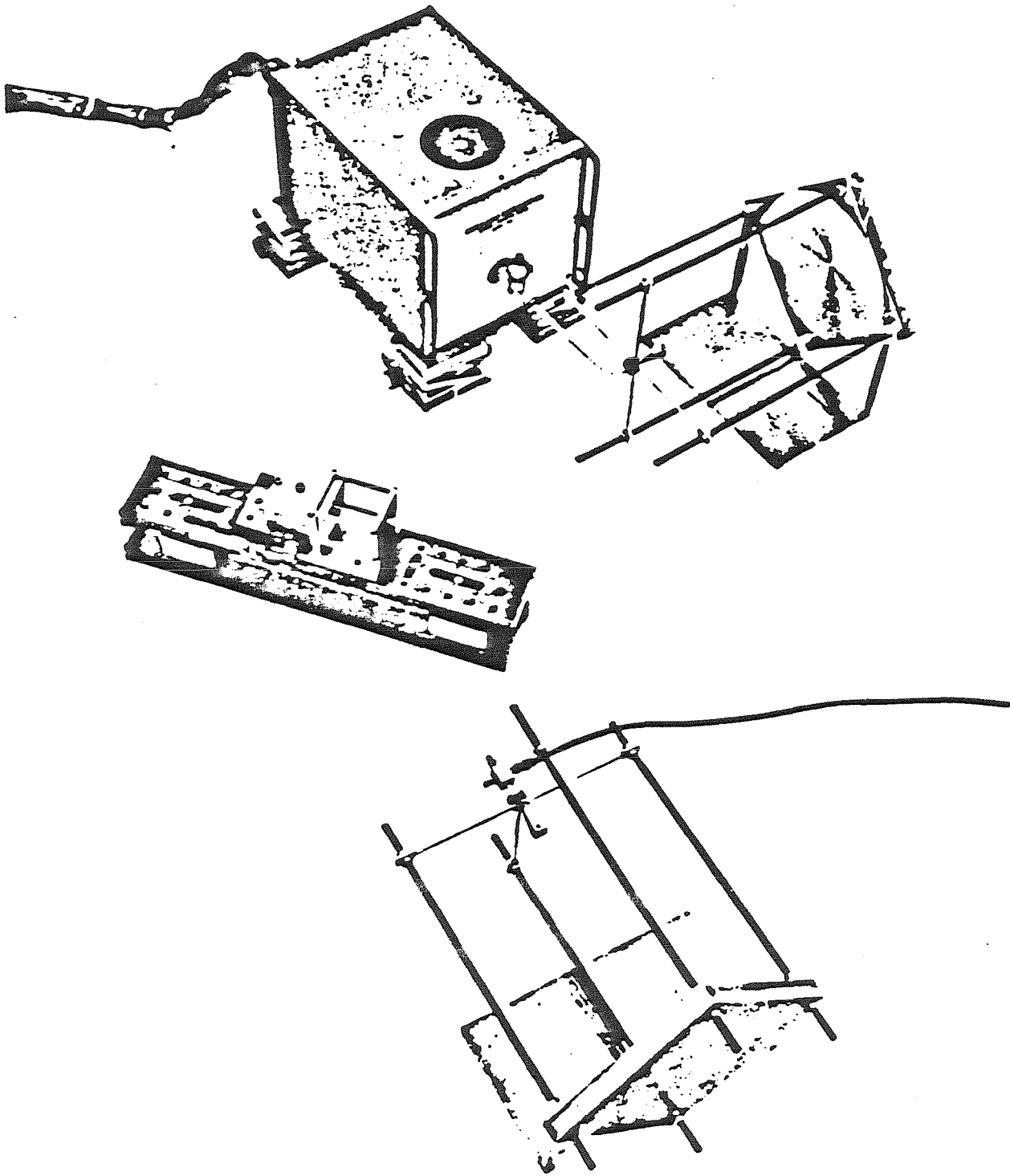
Fig. 4.1 Experimental setup for transmission measurement in the vicinity of 100 GHz.

zero dB reference

5 dB

(a)

zero dB reference
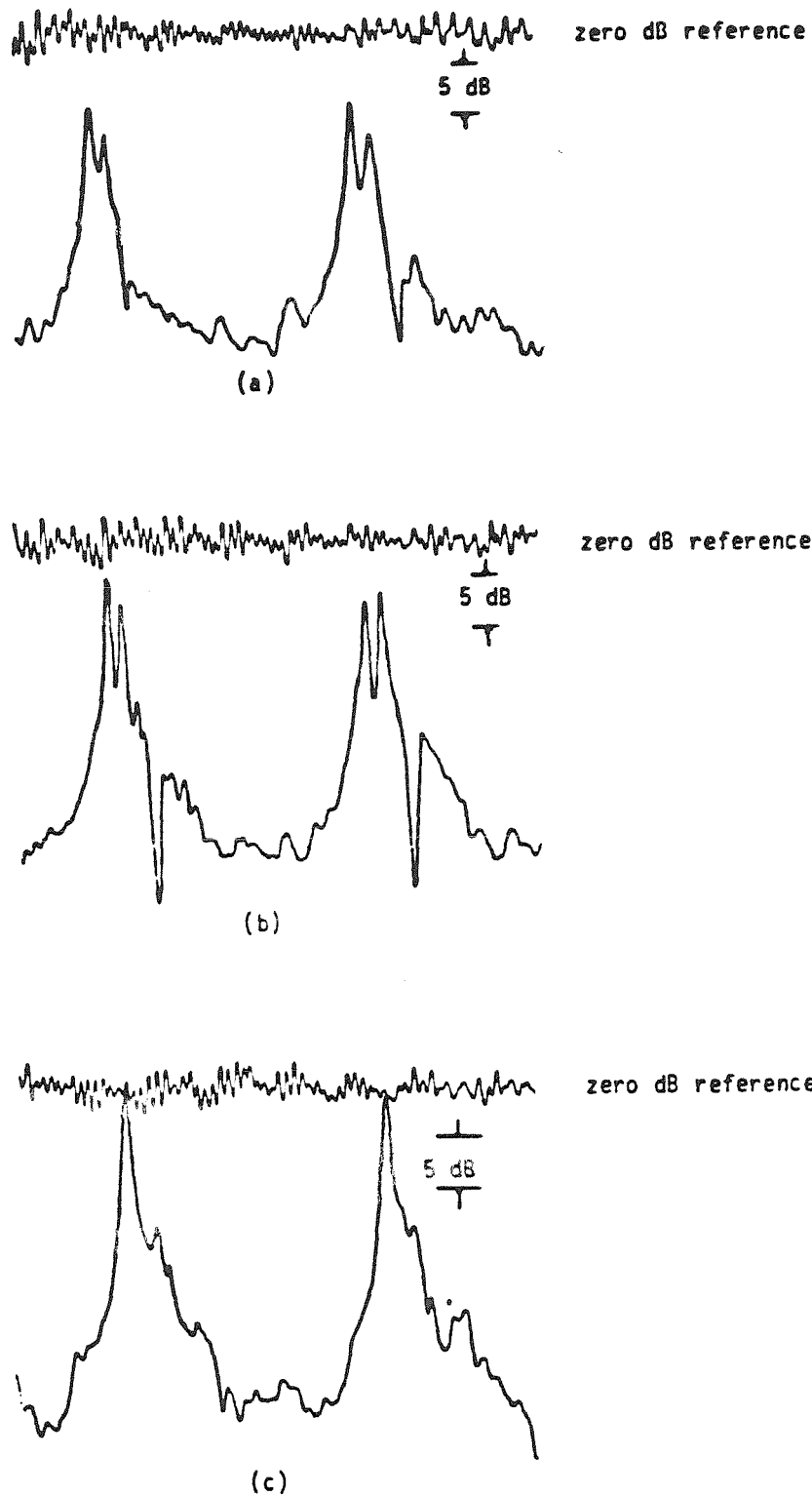
5 dB

(b)

zero dB reference

5 dB

(c)

Fig. 4.2 Experimental results of transmission measurement for diplexers with different geometries. (a) Plane diplexer. (b) Cylindrical diplexer. (c) Toroidal diplexer.

by steps of approximately 3 dB in going from plane to cylindrical and cylindrical to toroidal reflecting geometries. Within our experimental errors of $\pm$ 1 dB, the peak of T_4 for toroidal diplexer shows 0 dB loss relative to the toroidal waveguide. Furthermore, the toroidal geometry also helps in suppressing the unwanted secondary transmission peak which invariably appears in the transmission characteristic curves of plane and cylindrical diplexers.

Chapter 5. CONCLUSION

In this work, the solution to the minimum diffraction design problem of a folded Fabry-Perot quasi-optical ring resonator diplexer is given. The performance of diplexers with and without optimal geometry was invest-igated both theoretically and experimentally. Performance curves are presented so that they can be used to estimate how much improvement in performance one could expect by switching from the plane reflector to the optimal curved reflector.

Important steps are summarized below for the interest of prospective practical users:

(1) The size of the cavity, appropriate input Gaussian beam waist-size, and optimal radii of curvature for minimum diffraction are all deter-mined by the intermediate frequency f_{IF} of the system as explained in Chapter 2.

(2) The resonant order q is approximately given by $q = \sqrt{2}W/\lambda$.

(3) For a plane-mirror diplexer, the fractional part of the phase difference of the two dominant eigenmodes in modulo π is given by $\delta \simeq 1/q$.

(4) For a toroidal-mirror diplexer, the phase difference can be obtained from the empirical formula associated with Fig. 3.4.

(5) Based on the value of the finesse, F, required by the experimental condition the peak transmission for both the plane and toroidal diplexers can be estimated from the curves given in Fig. 3.6, assuming no diffraction loss in the vertical direction.

(6) The peak transmission can then be corrected for loss in the vertical direction using Eq. (3.30), and the reflectivity of the mesh can be determined from Eq. (3.29).

APPENDIX: Determination of the $\underset{\sim}{T}$ matrix for a two-dimensional waveguide with one curved wall.

The basic idea of this approach is to approximate the curved surface by a series of steps as illustrated in Fig. A1. Let the total number of steps be 2N-1, the depth of the steps are chosen, for later convenience, so that

$$L_i/L_{i-1} = (L_0/L_g)^{1/N} \quad \text{for } i<0 \qquad (A.1)$$

$$L_i/L_{i-1} = (L_0/L_g)^{-1/N} \quad \text{for } i>0 \qquad (A.2)$$

Note that the ratio is independent of the step index "i". Values of z where the jumps occur are chosen so that the original curve x(z) bisects the vertical segments at each jump, i.e. $x(Z_{i-1,i})=(L_{i-1}+L_i)/2$. The step width W_i is fixed by the conditions above and does depend on the index "i".

The $\underset{\sim}{T}$ matrix can be expressed as

$$\underset{\sim}{T} = \underset{\sim}{P}_N \underset{\sim}{J}_d \underset{\sim}{P}_{N-1} \underset{\sim}{J}_d \cdots \underset{\sim}{P}_2 \underset{\sim}{J}_d \underset{\sim}{P}_1 \underset{\sim}{J}_u \underset{\sim}{P}_0 \cdots \underset{\sim}{P}_{-(N-1)}\underset{\sim}{J}_u \underset{\sim}{P}_{-N} \qquad (A.3)$$

where $\underset{\sim}{P}_\ell$, the propagation along step "ℓ" of width δW_ℓ, is given by

$$\underset{\sim}{P}_\ell = \underset{\sim}{P}_{1\ell} \times \underset{\sim}{P}_{2\ell} \times \cdots \qquad (A.4)$$

and

$$\underset{\sim}{P}_{n\ell} = \begin{pmatrix} \cos(k_{n\ell}\delta W_\ell) & \sin(k_{n\ell}\delta W_\ell)/k_{n\ell} \\ -k_{n\ell}\sin(k_{n\ell}\delta W_\ell) & \cos(k_{n\ell}\delta W_\ell) \end{pmatrix}$$

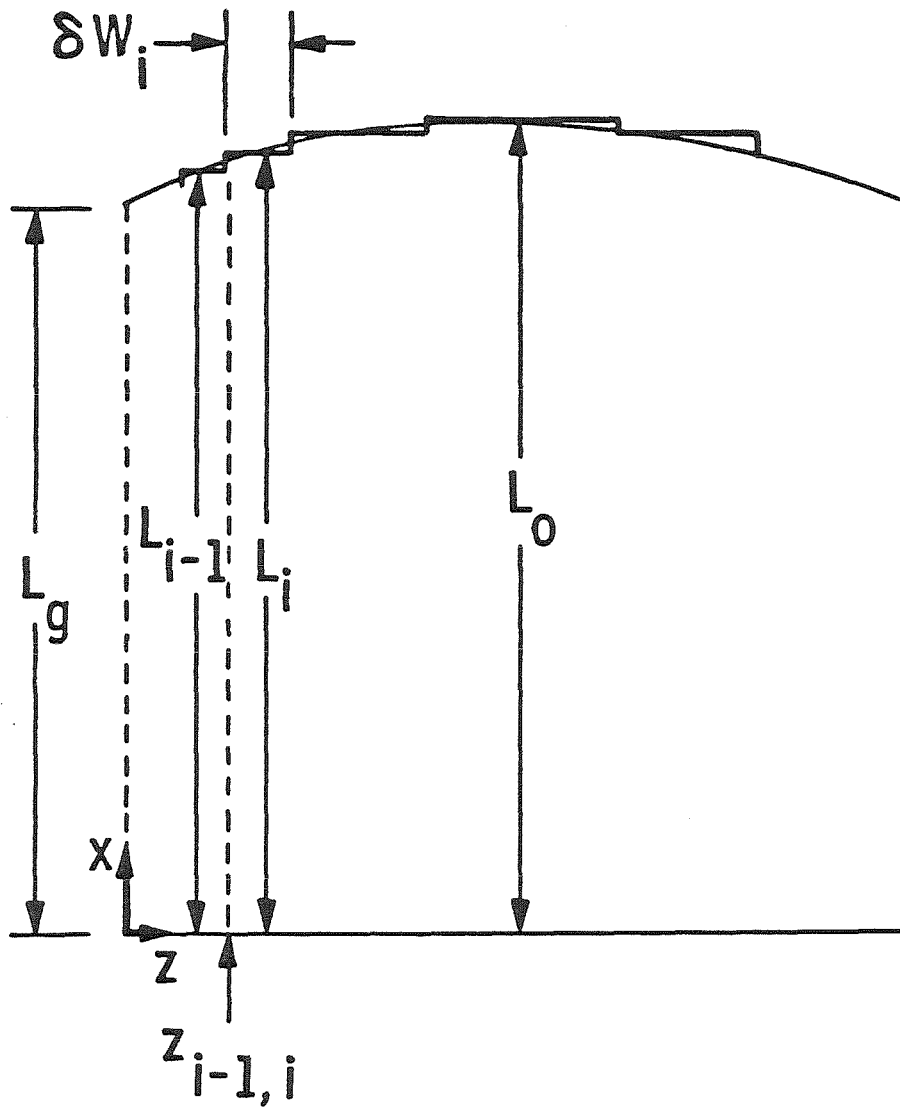with $\quad k_{n\ell}^2 = (2\pi/\lambda)^2 - (n\pi/L_\ell)^2 \qquad (A.6)$

Fig. A1. Approximation of curved wall by steps of constant length ratio.

For frequencies beyond cutoff (i.e. for imaginary values of $k_{n\ell}$), the expression for $k_{n\ell}$ given above can still be used with the standard substitution of hyperbolic functions for trigonometric functions. T_u is the mode change at each "step up jump" given by

$$\underset{\sim}{T}_u = \begin{pmatrix} x & 0 \\ 0 & x \end{pmatrix} \tag{A.7}$$

and T_d is the corresponding change at each "step down jump" given by

$$\underset{\sim}{T}_d = \begin{pmatrix} x^t & 0 \\ 0 & x^t \end{pmatrix} \tag{A.8}$$

where
$$x_{mn} = \frac{2}{\sqrt{L_i L_{i-1}}} \int_0^{L_{i-1}} \sin(m\pi x/L_i)\sin(n\pi x/L_{i-1})dx$$

$$= \sqrt{L_{i-1}/L_i} \,[\text{sinc}(n\pi - m\pi L_{i-1}/L_i) - \text{sinc}(n\pi + m\pi L_{i-1}/L_i)] \tag{A.9}$$

Note that x_{mn} depends only on n and m, and the ratio L_{i-1}/L_i which is independent of the step index "i".

For the calculations reported here, the step approximation converged when 50 to 100 steps were used. The size of the plane wave basis required ranged from 10 to 20 values of n centered about q. Only a few waves beyond cutoff could be used because of round-off errors in the cosh and sinh functions.

References for Part II

[1] Gustincic, J.J., "A quasi-optical radiometer," Digest of the Second International Conference on Submillimeter Waves and Their Applications, San Juan, Puerto Rico, 6-11, Dec. 1976, pp. 106-107

[2] Gustincic, J.J., "A quasi-optical receiver design," IEEE MTT-S International Microwave Symposium Digest, 1977, pp. 99-101

[3] See, for example, M. Born and E. Wolf, Principles of Optics, Pergamon Press, New York, 1965

[4] Erickson, N.R., "A directional filter diplexer using optical techniques for millimeter to submillimeter wavelength," IEEE Trans. Microwave Theory Tech. Vol. MTT-25, Oct. 1977, pp. 865-866

[5] Arnaud, J.A., A.A.M. Saleh, and J.T. Ruscio, IEEE Trans Microwave Theory Tech. Vol. MTT-22, pp. 486-493

[6] Goldsmith, P.F., IEEE Trans Microwave Theory Tech. Vol. MTT-30, pp. 820-823

[7] Nakajima, N. and R. Watanabe, "A quasioptical circuit technology for shortmillimeter wavelength multiplexers," IEEE Trans. Microwave Theory Tech. Vol. MTT-29, Sept. 1981, pp. 897-905

[8] Chiou, A.E. and H.M. Pickett, "Quasi-optical ring resonator diplexer: theory and experiment," Conference Digest, Sixth International Conference on Infrared and Millimeter Waves, Miami, Florida W-4-9, Dec. 1981

[9] Barone, S.R., "Resonances of the Fabry-Perot Laser," J. Appl. Phys., Vol. 34, Apr. 1963, pp. 831-843

[10] Boyd, G.D. and J.P. Gordon, "Confocal multimode resonator for millimeter through optical wavelength masers," Bell Sys. Tech. J., Vol. 40, Mar. 1961, pp. 489-508

[11] Durschlag, M.S. and T.A. DeTemple, "Far-IR optical properties of free-standing and dielectrically backed metal meshes," Appl. Opt., vol. 20, No 7, April 1981, pp. 1245-1251

[12] Chen, C.C. "Transmission through a conducting screen perforated periodically with apertures," IEEE Trans. Microwave Theory Tech., Vol. MTT-18, Sept. 1970, pp. 627-632